THESIS FOR THE DEGREE OF DOCTOR OF PHILOSOPHY

Bridging Single-Particle Characterisation Gaps of Optical Microscopy in the Nano-Submicron Regime

ERIK OLSÉN

Department of Physics
CHALMERS UNIVERSITY OF TECHNOLOGY
Gothenburg, Sweden 2023

Bridging Single-Particle Characterisation Gaps of Optical Microscopy in the Nano-Submicron Regime

ERIK OLSÉN

ISBN 978-91-7905-891-3
Doktorsavhandlingar vid Chalmers tekniska högskola, Ny serie nr 5357
ISSN 0346-718X.

Department of Physics
Chalmers University of Technology
SE-412 96 Gothenburg
Sweden
Telephone + 46 (0)31-772 10 00

Printed at Chalmers Digitaltryck
Gothenburg, Sweden 2023

Cover illustration: Deep-learning generated image of biological nanoparticles with bound gold nanoparticles during illumination with a green laser.

Bridging Single-Particle Characterisation Gaps of Optical Microscopy in the Nano-Submicron Regime

ERIK OLSÉN
Department of Physics
Chalmers University of Technology
Gothenburg, Sweden 2023

Abstract

As the practical importance of particles in the nano-submicron size regime continues to increase in both biomedical applications and industrial processes, so does the need for accurate and versatile characterisation methods. Optical scattering microscopy methods are commonly used for single-particle characterisation as they provide quick measurements at physiologically relevant conditions with detection limits reaching down to individual biomolecules. However, quantitative particle characterisation using optical microscopy often rely on assumptions about the surrounding media and the particle, including solution viscosity, boundary conditions, as well as particle shape and material. Since these assumptions are difficult to evaluate, particle characterisation beyond hydrodynamic radius and/or mass remains challenging.

The aim of this thesis is to contribute to bridging the gaps that limit quantitative optical microscopy-based characterisation of individual particles in the nano-submicron regime by both developing new and improving existing microscopy methods. Specifically, in Paper I a method was developed to evaluate the relation between diffusivity and particle size to enable measurements of the hydrodynamic boundary condition. Papers II-V are based around the development of holographic nanoparticle tracking (H-NTA) and extensions thereof, with the intent of using the complex-valued optical field for material sensitive particle characterisation with minimal dependence on the surrounding media. In Paper II, H-NTA by itself was used to characterise suspensions containing nanobubbles and molecular aggregates. In Paper III, the combination of H-NTA with deep learning was used to achieve simultaneous quantification of size and refractive index directly from single microscopy images, which allowed detection of reversible fluctuations in nanoparticle aggregates. In Paper IV, H-NTA augmented with a low frequency attenuation filter, coined twilight holography, was used to investigate the interaction between herpes viruses and functionalised gold nanoparticles in terms of size, bound gold mass, and virus refractive index. In Paper V, the combination of twilight holography and interferometric scattering microscopy (iSCAT) was used to quantify both size and polarizability of individual nanoparticles without the need of detailed knowledge about the surrounding media. Taken together, the presented results in this thesis provide both new insights into heterogenous nanoparticle systems and contributes to narrowing the gap for detailed optical particle characterisation.

Keywords: Optical microscopy, particle tracking, size estimation, material sensitivity, dynamics, particle shape, holography, iSCAT

It would be madness and inconsistency to suppose that things which have never yet been performed can be performed without employing some hitherto untried means.

- Sir Francis Bacon, *Novum Organum*

List of publications

This thesis is based on the work contained in the papers listed below. The papers are referred to using their roman numerals throughout the thesis.

Paper I:
Diffusion of Lipid Nanovesicles Bound to a Lipid Membrane Is Associated with the Partial-Slip Boundary Condition
Erik Olsén*, Silver Jõemetsa*, Adrián González Rodríguez, Paul Joyce, Vladimir P. Zhdanov, Daniel Midtvedt, and Fredrik Höök
Nano Letters 2021, 21, https://doi.org/10.1021/acs.nanolett.1c02092

Paper II
Size and Refractive Index Determination of Subwavelength Particles and Air Bubbles by Holographic Nanoparticle Tracking Analysis
Daniel Midtvedt, Fredrik Eklund, Erik Olsén, Benjamin Midtvedt, Jan Swenson, and Fredrik Höök
Analytical Chemistry 2020, 92, https://doi.org/10.1021/acs.analchem.9b04101

Paper III:
Fast and Accurate Nanoparticle Characterization Using Deep-Learning-Enhanced Off-Axis Holography
Benjamin Midtvedt, Erik Olsén, Fredrik Eklund, Fredrik Höök, Caroline Beck Adiels, Giovanni Volpe, and Daniel Midtvedt
ACS Nano 2021, 15, https://doi.org/10.1021/acsnano.0c06902

Paper IV:
Label-Free Optical Quantification of Material Composition of Suspended Virus-Gold Nanoparticle Complexes
Erik Olsén, Benjamin Midtvedt, Adrián González, Fredrik Eklund, Katarzyna Ranoszek-Soliwoda, Jaroslaw Grobelny, Giovanni Volpe, Malgorzata Krzyzowska, Fredrik Höök, and Daniel Midtvedt
Submitted, https://doi.org/10.48550/arXiv.2304.07636

Paper V:
Dual-Angle Interferometric Scattering Microscopy for Detailed Optical Multiparametric Particle Characterization
Erik Olsén, Berenice García Rodríguez, Fredrik Skärberg, Petteri Parkkila, Giovanni Volpe, Fredrik Höök and Daniel Midtvedt
In manuscript

* Shared first-author

Contribution report

Paper I

I was responsible for the idea behind the investigation and planned the experiments together with Silver Jõemetsa. I performed the data analysis, and I was main responsible for writing the article.

Paper II

I built the experimental setup, developed the code for the hardware communication, and was part of developing the image processing code used to analyse the holography data. I also participated significantly in the data analysis as well as in the writing of the article.

Paper III

I was responsible for the design and planning of the experiments. I built the experimental setup, performed the experiments, and participated significantly in the data analysis. I was not involved in the training of the neural network. I also participated significantly in the writing of the article.

Paper IV

I was responsible for the idea behind the investigation, the design, and planning of the twilight holography experiments. I built the optical experimental setup, performed the experiments related to the twilight holography, performed the data analysis, and was main responsible for the writing of the manuscript.

Paper V

I was responsible for the idea behind the investigation, the experimental design, and planning of the experiments. I built the optical experimental setup and performed the interferometric scattering (iSCAT)-twilight holography experiments. I performed most of the data analysis, with the exception of training the neural network used to quantify the iSCAT images. I was main responsible for the writing of the manuscript.

Publications not included in the thesis

Evaluation of Pressure Generated by Resistors From Different Positive Expiratory Pressure Devices
Monika Fagevik Olsén, Maria Carlsson, Erik Olsén, and Elisabeth Westerdahl
Respiratory care 2015, 60 (10) 1418-1423

Multidimensional hybridization of dark surface plasmons
Andrew B. Yankovich, Ruggero Verre, Erik Olsén, Anton E. O. Persson, Viet Trinh, Gudrun Dovner, Mikael Käll, and Eva Olsson
ACS Nano 2017, 11, 4, 4265–4274

Label-free spatio-temporal monitoring of cytosolic mass, osmolarity, and volume in living cells
Daniel Midtvedt, Erik Olsén, Fredrik Höök, and Gavin D. M. Jeffries
Nature Communications 2019, 10, 340

Visualizing spatial variations of plasmon-exciton polaritons at the nanoscale using electron microscopy
Andrew B. Yankovich, Battulga Munkhbat, Denis G. Baranov, Jorge Cuadra, Erik Olsén, Hugo Lourenço-Martins, Luiz H. G. Tizei, Mathieu Kociak, Eva Olsson, and Timur Shegai
Nano Lett. 2019, 19, 11, 8171–8181

Constructing a library of metal and metal–oxide nanoparticle heterodimers through colloidal assembly
Tina A. Gschneidtner, Sarah Lerch, Erik Olsén, Xin Wen, Amelia C. Y. Liu, Alicja Stolaś, Joanne Etheridge, Eva Olsson, and Kasper Moth-Poulsen
Nanoscale 2020, 12, 11297-11305

FRET-Based Assay for the Quantification of Extracellular Vesicles and Other Vesicles of Complex Composition
Konrad Thorsteinsson, Erik Olsén, Eneas Schmidt, Hudson Pace, and Marta Bally
Analytical Chemistry. 2020, 92, 23, 15336–15343

Single-shot self-supervised object detection in microscopy
Benjamin Midtvedt, Jesús Pineda, Fredrik Skärberg, Erik Olsén, Harshith Bachimanchi, Emelie Wesén, Elin K Esbjörner, Erik Selander, Fredrik Höök, Daniel Midtvedt, and Giovanni Volpe
Nature Communications 2022, 13.1: 7492

Patents not included in the thesis

Method and arrangement for holographic nanoparticle tracking analysis (H-NTA) in an off-axis digital holographic microscope
Daniel Midtvedt, Erik Olsén, Benjamin Midtvedt, and Fredrik Eklund
Patent number: WO2022123064A1

Method and arrangement for optical detection of dielectric particles
Fredrik Eklund Fredrik Höök, Erik Olsén, and Daniel Midtvedt
Patent number: WO2023075674A1

List of abbreviations and definitions

Textual abbreviations

2DFN	Two-dimensional flow nanometry
AuNP	Gold nanoparticle
BS	Beam splitter
CNN	Convolutional neural networks
COBRI	Coherent brightfield microscopy
DAISY	Dual-angle interferometric scattering microscopy
DLS	Dynamic light scattering
DNA	Deoxyribonucleic acid
DOPC	1,2-Dioleoyl-sn-glycero-3-phosphocholine
EVs	Extracellular vesicles
FBS	Fetal bovine serum
HSV(-1/-2)	Herpes simplex virus (type 1 or type 2)
HWP	Half-wave plate
H-NTA	Holographic nanoparticle tracking analysis
iSCAT	Interferometric scattering microscopy
LFAF	Low frequency attenuation filter
MALS	Multi-angle light scattering
NA	Numerical aperture
NTA	Nanoparticle tracking analysis
OBJ	Objective lens
PAS	Propagation of angular spectrum
PBS	Polarizing beam splitter
PEG	Polyethylene glycol
POPC	1-palmitoyl-2-oleoyl-sn-glycero-3-phosphocholine (lipid molecule)
QLSI	Quadriwave lateral shearing interferometry
QWP	Quarter-wave plate
RI	Refractive index
SLB	Supported lipid bilayer
TaAuNP	Tannic acid gold nanoparticle
TEM	Transmission electron microscopy
TIRF	Total internal reflection fluorescence
TL	Tube lens
tNTA	Twilight nanoparticle tracking analysis
U-Net	A convolutional network architecture which looks “U-like”
WAC-NET	Weighted average convolutional neural network

Mathematical symbols

a	The attenuation of the low frequency attenuation filter
α	Particle polarizability
b	Slip length
D	Diffusion constant
D_{f}	Fractal dimension
D_{∞}	Diffusion constant in bulk (far away from any neighbouring surface)
δ	Characteristic decay length in total internal reflection fluorescence
$\epsilon_0/\epsilon_{\mathrm{m}}$	Dielectric constant/relative dielectric constant
η	Viscosity
f	Optical form factor
$\tilde{f}$	Generalised optical form factor
$\boldsymbol{\mathcal{F}}$	Fourier transform
h	Particle height
h_0	Distance from the centre of a particle to a nearby surface
I	Intensity of the optical field
$\Im$	Imaginary part of a complex number
J_1	First order Bessel function
$\vec{k}, k$	Wave vector, where $k = \left\vert\vec{k}\right\vert = 2\pi/\lambda$
k_{B}	Boltzmann constant
K	Blur-factor describing the effect from particle motion
λ/λ_0	Wavelength in media/ wavelength in vacuum
m	Particle mass
μ	Mobility
n	Refractive index
N	Number of particle observations
$\sigma_{\mathrm{abs/scat/ext}}$	Absorption/scattering/extinction particle cross section
σ^2	Contribution of localisation uncertainty to the mean squared displacement
$\Delta\Phi$	Optical phase-shift
$\vec{p}$	Dipole moment
ρ	The spatial distribution of mass within the particle
q	The difference in wave vectors between the incoming and outgoing light
$\Re$	Real part of a complex number
R_{g}	Radius of gyration
R_{h}	Hydrodynamic radius
t	Optical transmittance
T	Temperature (in Kelvin)
v	Flow-induced velocity
γ	Friction coefficient
ξ	Stochastic force
ζ	Position uncertainty

Contents

1

Introduction

The future cannot be predicted, but futures can be invented.
– Dennis Gabor[*]

Visualisation is often key for understanding complex systems, as best captured by the phrase *"seeing is believing"*. Since most of the underlying processes of life occur on the nanometre to micrometre length scales (Figure 1), there are numerous processes around us that our naked eyes cannot see by themselves. To overcome this limitation, mankind has developed microscopes with ever-improving resolution and sensitivity. As the requirements of a measurement technique varies depending on the system under investigation, several different microscopy techniques have been developed over the centuries. These techniques range from optical methods such as fluorescence and phase contrast to electron and atomic force microscopy [1–3], and their importance to the scientific community is recognised by several Nobel Prizes related to advances in microscopy method development [4–10].

Building on that tradition, the pursuit of ever-improving quantitative imaging tools continues to this day. However, just because it is possible to observe a particular experimental system, correct interpretation of the data is far from a trivial task. For example, in the beginning of the 19th century, Robert Brown and several other researchers observed in their microscopes that small particles, such as clay particles contained in the pollen of plants[†], display a stochastic motion when dispersed in a fluid [11–13]. Numerous explanations for this phenomenon were initially hypothesised before it was eventually settled that this motion originates from the existence of atoms and molecules [14]. Similarly, disagreement persists to this day among scientists regarding how to correctly interpret optical measurements of biological nanoparticles. This includes for example how to relate light scattering to particle properties [15–17] and the interpretation of correlations between particle size and fluorescence [18–20], illustrating the difficulty in translating measurements to particle information.

[*] Dennis Gabor (1900 –1979) received the Nobel Prize in Physics 1971 for the development of the holographic method [8].
[†] Robert Brown wrote that he analysed particles or granules from grains of pollen [11].

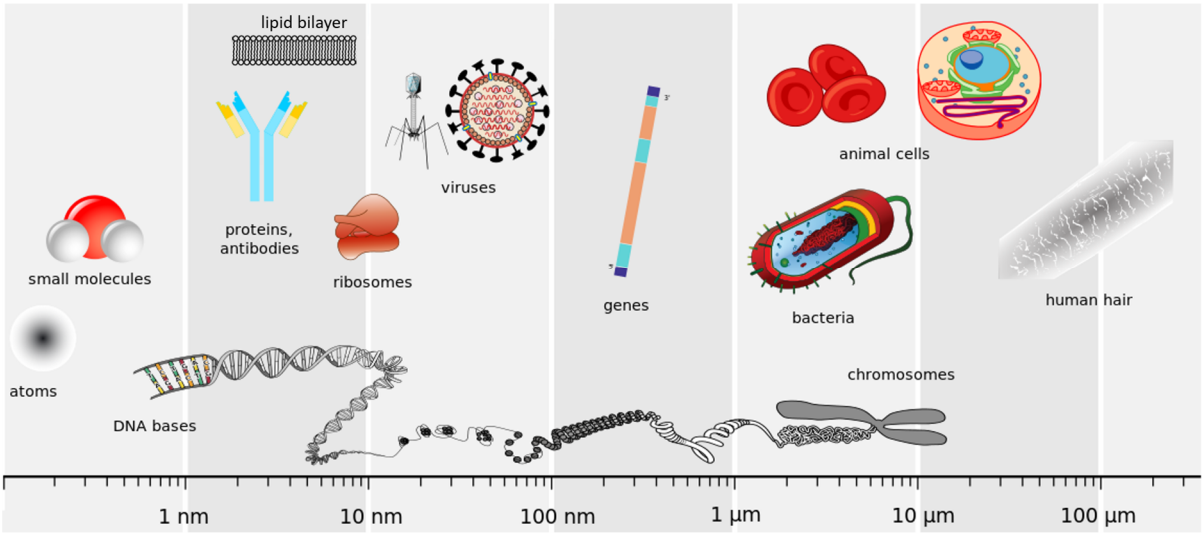

Figure 1 Schematic figure showing examples of important biological entities at different length scales, ranging from sub-nanometre to hundreds of micrometres. This thesis work primarily involves investigating particles in the 20-500 nm size range. The image is adapted from Wikimedia [21] under CC BY-SA 2.5 licence.

Although numerous microscopy methods such as electron microscopy have a spatial resolution well beyond that of optical microscopy [1], the latter is still often preferred in the context of life sciences. This is primarily due to the fact that optical methods offer high-throughput measurements of individual particles under physiological or near physiological conditions, whereas high-resolution imaging methods such as electron microscopy often require non-physiological imaging conditions. For example, despite that biomolecules and biological nanoparticles such as viruses and lipid vesicles all are smaller than the optical resolution limit of a few hundred of nanometres [22] (Figure 1), optical characterisation methods still enable accurate single-particle estimates in terms of concentration, size, and/or dry mass [23,24]. This has made optical techniques common when characterising size and concentration of particle suspension, in particular for biological particle samples such as liposomes and extracellular vesicles (EVs) [25].

Optical particle characterisation spans a wide range of techniques, including non-imaging techniques such as flow cytometry [26] and dynamic light scatting (DLS) [27], and imaging methods such as darkfield [23], interferometric scattering (iSCAT) [23], fluorescence [28], and Raman microscopy [29]. For studying individual biological particles, scattering microscopy is a common characterisation method since it works well with aqueous samples, has a detection limit that includes 100 kDa biomolecules, does not require any addition of labels, and the particle signal is related to properties such as mass and shape [23,30,31]. Despite being widely implemented, particle characterisation using label-free scattering microscopy currently has several limitations. These limitations originate from the fact that size and structure of single nanoparticles cannot easily be estimated directly from a microscopy image as the particles are much smaller than the spatial resolution limit [32]. Particle properties such as size are instead estimated indirectly by for example relating particle motion to size via the diffusivity-

size relation [33]. However, such relations rely on assumptions about the experimental system that are challenging to evaluate, which contribute to limitations regarding the quantitative precision and hence the applicability of the characterisation techniques.

During the past decade, the single-particle detection limit of optical scattering microscopy has improved significantly whereas the quantified particle information in the nano-submicron size regime is approximately the same. For example, the single-particle detection limit using interferometric scattering microscopy methods is now below 100 kDa* biomolecules in water [35], where recent developments go all the way down to 9 kDa when on a surface [36] and 66 kDa in suspension [31]. In comparison, most optical scattering microscopy methods quantify scattering intensity and particle position with little particle shape or material composition information [23]. Considering that the function of nanoparticles is greatly influenced by their size, shape, mass, and composition [37,38], there is need of improvements regarding the quantitative particle information that can be extracted from a single measurement.

Therefore, one of the main remaining challenges for optical particle characterisation is the combination of detection and *quantitative multiparametric particle estimates* of individual particles in the nano-submicron regime with as few prior assumptions about the particle system as possible. Most often the assumptions behind relating experimental data to particle properties are overlooked, as nicely captured by the joke "assume a spherical chicken" [39]. However, such assumptions and approximations put limitations on the potential analysis of heterogenous particle samples which needs to be removed to further expand the applicability of optical particle characterisation.

The mission of this thesis is to contribute to bridging the gaps of optical microscopy-based multiparametric characterisation of individual particles in the nano-submicron size regime. The approach taken is to acknowledge the complexity with respect to relying on diffusivity-based sizing and scattering intensity to characterise heterogenous particle samples, in order to thereby find new ways of obtaining size, material, and shape information on the single-particle level. For example, if only the size of a suspended nanoparticle is of interest, one commonly used approach is to relate the diffusivity of the particle to size using the Stokes-Einstein relation [33]. When relating diffusivity to particle size, several assumptions about the particle need to be made, one of which being its hydrodynamic boundary condition. If the no-slip boundary condition is incorrectly assumed, the size can become underestimated by up to approximately 30% [40]. This is highlighted in Paper I, which introduces a method to evaluate the hydrodynamic boundary condition of biological nanoparticles.

Papers II-V all involve method development with the purpose of improving the quantification of size, shape, and material properties of suspended particles in the nano-submicron size regime using scattering-based optical microscopy. In this context, a

* To compare with particles, a protein with a mass of 100 kDa has a radius of around 3 nm [34]. To relate other protein masses to size, the volume of a protein is approximately proportional to its mass.

common analysis approach is to quantify radius and refractive index of individual particles [41–44], where refractive index is related to the material of the observed particle. However, most optical characterisation methods for particles in the nano-submicron size regime measure only scattering intensity, which is insufficient to distinguish between different material types such as dielectric particles, metallic particles, and nanobubbles. One approach to overcome this limitation is to use methods such as off-axis holography that measures the complex-valued optical field [45], as the real and imaginary parts of the optical signal relates to different material properties. Despite its quantitative potential, optical holography is mostly used to characterise larger structures such as biological cells [46], while its use for characterising particles in the nano-submicron regime, as done in this thesis work, is less explored.

Paper II presents the development of off-axis holographic nanoparticle tracking (H-NTA) to distinguish suspended nanobubbles from solid particles while also quantifying their hydrodynamic radius and refractive index. As the scattering pattern from a particle inherently contains information about particle size, shape, and refractive index [47], Paper III investigates the combination of H-NTA and deep-learning image analysis to enable simultaneous quantification of size and refractive index from images of scattering patterns of subwavelength-sized particles. This measurement method enables sub-second temporal resolution of both size and refractive index, which was used to investigate the dynamics of nanoparticle clusters. Paper IV explores the potential of extending the quantitative measurement regime of off-axis holography into the nanoparticle domain by combining H-NTA with a low frequency attenuation filter (LFAF). This allows simultaneous optical quantification of the dielectric and metallic contributions of individual nanoparticle complexes, which was used to investigate the interaction between herpes simplex virus type 2 (HSV-2) and tannic acid modified gold nanoparticles (TaAuNPs). Inspired by multi-angle light scattering techniques [48], Paper V investigates the combination of H-NTA with interferometric scattering microscopy (iSCAT) to achieve simultaneous size and refractive index quantification of individual nanoparticles without relying on the diffusivity-size relation. Since the scattering-based size estimate depends on both the distribution of mass within the particles and their outer radius, whereas the simultaneously measured hydrodynamic radius estimates the outer particle radius, the two size estimates were also used to optically differentiate between solid spherical particles and particle aggregates.

To provide a broader context of the work, the thesis starts with a chapter describing the particle systems of main importance for this thesis work, followed by two chapters covering the theoretical background of the particle information contained in an optical microscopy image and the theoretical foundation used for relating diffusivity to particle properties. The subsequent chapter covers the main experimental methods used in this work, followed by a chapter summarising the five appended papers. The final chapter contains the main conclusions of this thesis and a future outlook addressing some of the remaining scientific challenges together with potential method development that could further bridge the gap of optical microscopy-based particle characterisation.

2

Biological background

Historically, nature has been very good at surprising us
- Sean M. Carroll[*]

The development of microscopy methods and our understanding about the world on the nano- and microscale have been linked together ever since the publication of Robert Hooke's *Micrographia* in 1665 [49]. Nowadays, our understanding about biological particle systems is to a large extent based on microscopy imaging, where remaining unanswered questions motivates the continued method development.

Most of the investigated particles in this thesis work are either biological nanoparticles or dielectric subwavelength-sized particles. Biological particles have to a first approximation a real-valued refractive index for visible wavelengths [50]. Dielectric particles refer to non-conducting particles, implying a real-valued refractive index [51]. Since biological and dielectric particles have similar optical scattering signals, dielectric particles of known size and material are often used to evaluate the performance of newly developed characterisation methods [52,53]. For example, silica and polystyrene spheres were used in Papers II-V to evaluate the size and material sensitivity of the developed methods. However, of main interest in this thesis is the ability of the methods to investigate biological nanoparticle systems such as lipid vesicles tethered to a supported lipid bilayer (SLB), extracellular vesicles (EVs), herpes viruses, and nanoparticle aggregates (Figure 2). The central biologically relevant particle systems investigated in this thesis work are introduced in this chapter.

2.1 Lipid membranes and vesicles

Lipids are amphiphilic molecules characterised by a hydrophilic head group linked to hydrophobic alkyl chains that are commonly referred to as lipid tails [54,55]. Due to the amphiphilic nature of lipids, they tend to self-assemble into organised structures such as lipid bilayers and vesicles when in aqueous media (Figure 2). This spontaneous organisation of amphiphilic molecules from a disordered to an ordered state is driven

[*] Sean M. Carroll (born 1966) is a theoretical physicist and Homewood Professor of Natural Philosophy at Johns Hopkins University. He is also a prominent science communicator via books and podcasts.

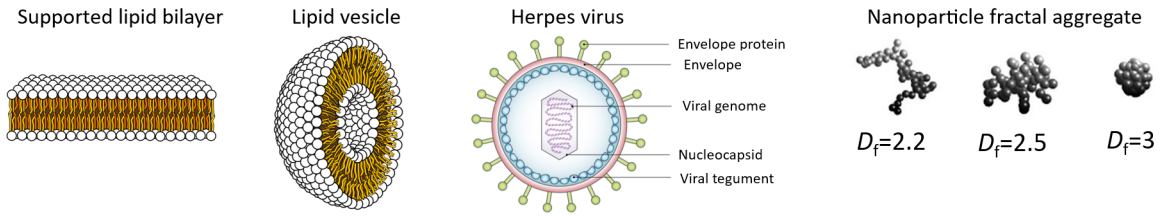

Figure 2 Selection of the biological structures and particles investigated in the papers appended to this thesis, which includes supported lipid bilayers (SLBs), lipid vesicles, herpes viruses, and nanoparticle aggregates. D_f is the fractal dimension, where a lower D_f corresponds to fewer particles per unit volume in an aggregate. The images of the fractal aggregates are adapted from Ref. [56] under CC-BY license.

by entropic effects. Specifically, since water molecules can adapt more configurations with hydrogen bonds when interacting with hydrophilic molecules than with hydrophobic molecules, forming organised structures that "hide" the tails of the lipids from the surrounding water increases the overall entropy [54].

Depending on the geometry of the lipid, which can be estimated using the effective area per head group, tail length, and volume of the tail, they organise into different structures [55]. For example, single-chained lipids with large head groups typically form spherical micelles, which are enclosed spherical structures consisting of a monolayer of lipids. In contrast, phospholipids with two tails tend to form bilayers and vesicles, which are planar and spherical enclosed structures consisting of a bilayer of lipids, respectively. Membranes consisting of a bilayer of lipids are commonly utilised by biological systems such as cells to separate their interior from the exterior, which is why phospholipids are prominent in both the outer membrane and internal organelles of cells [55].

During investigations of the properties of cell membranes, mimics such as SLBs are commonly used to reduce the complexity compared to the membrane of living cells [57]. SLBs are commonly formed on surfaces such as glass (silica) by letting liposomes, which are artificially made lipid vesicles, spontaneously attach to the surface. Once a critical coverage is reached, the liposomes rupture into an SLB [58]. In Paper I, the used membrane mimic was an SLB consisting of the phospholipid 1-palmitoyl-2-oleoyl-sn-glycero-3-phosphocholine (POPC) with a fraction of PEGylated[*] lipids used to control the separation between the SLB and membrane-attached particles.

SLBs and lipid vesicles differ from solid materials in that the lipids they consist of are mobile within the membrane. The motion of membrane molecules in a lipid membrane can therefore be described as an 2D fluid [55]. This property of SLBs was utilised in Paper I as its main method, two-dimensional flow nanometry (2DFN) [59], relies on the mobility of SLB-tethered particles to simultaneously estimate particle size and diffusivity (Section 5.5). In Paper I, the liposomes and EVs were tethered to the SLB using cholesterol-modified double stranded DNA as molecular linkers [60].

[*] Polyethylene glycol (PEG) is commonly used molecule to passivate surfaces, where PEGylation is the process of attaching PEG to other molecules such as lipids.

2.1.1 Extracellular vesicles

Extracellular vesicles (EVs) are a diverse family of lipid membrane-enclosed structures secreted by cells [61,62]. EVs are naturally occurring lipid vesicles that contain multiple different membrane molecules, including several types of lipids, membrane proteins, and glycolipids. Additionally, EVs also often contain cargo as they participate in intercellular transport [61].

Since EVs are circulating in the body and participate in a broad range of biological processes, EV subpopulations are considered important potential biomarkers for early diagnosis [61,62]. Different properties of EVs are measured using different experimental methods, where size estimation of single EVs is commonly performed by relating diffusivity to size (Section 4) [61]. To scrutinise this relation, the hydrodynamic boundary condition (Section 4.1) of both POPC liposomes and EVs were investigated in Paper I.

2.1.2 Nanobubbles

The term nanobubbles is typically used to describe bubbles with a diameter of less than one micron [63]. Although nanobubbles by themselves in water are theoretically predicted to be unstable [64], they can be made stable by using surfactants such as phospholipids or a combination of spans and tweens as used in Paper II [63]. Due to their non-toxic nature, nanobubbles are used in applications such as ultrasound contrast agents and diagnostics [65]. However, the use of nanobubbles comes with the challenge of differentiating nanobubbles from other particles potentially generated during the fabrication process [63]. For example, since nanobubbles are dielectric particles, their optical scattering intensity is similar to that of solid particles. Paper II attempts to address this challenge by measuring the optical phase shift on the single-particle level as the sign of the phase shift can be used to differentiate between bubbles and aggregates of surfactant molecules (Section 3.3.3).

2.2 Herpes viruses and tannic acid functionalised nanoparticles

The herpes simplex virus (HSV) is virus that consists of an inner capsid with a diameter around 125 nm and an outer spherical membrane of around 200 nm in diameter (Figure 2) [66]. Within the Herpesviridae family, HSV type 1 (HSV-1) and 2 (HSV-2) are two viruses that infect numerous humans around the world. Specifically, it was estimated in 2015 that more than 3.7 billion people under the age of 50 are infected with HSV-1 and 417 million people between 17 and 49 years of age suffer from HSV-2 [67].

Currently, there are several HSV vaccines at the pre-clinical stage, but none have yet been approved as treatment [68]. Due to the lack of HSV vaccines, several potential anti-herpes drugs are being tested. One such potential candidate that have been tested in various model systems is tannic acid [69]. Tannins such as tannic acid can interact with glycoproteins in the virus envelope, thus preventing virus attachment, entry, and cell-to-cell spread [69]. However, tannic acid is not commercially registered as a drug

since there is a lack of clinical evidence concerning its activity and selectivity [69]. Metallic nanoparticles functionalised with tannic acid are therefore explored as an alternative to free tannic acid in virus inhibition experiments [70–72]. To further explore the potential anti-viral properties of tannic acid functionalised nanoparticles, the interaction between HSV-2 and tannic acid modified gold nanoparticles (TaAuNPs) was investigated in Paper IV using the material sensitive signal of twilight off-axis holography (Section 5.1.2).

2.3 Particle aggregates

When particles or molecules interact with each other in solution they may eventually form larger disordered structures, which is referred to as aggregates. Particle aggregation is an example of a complicated random process that may display features such as self-similarity, scaling, and universality [73], which is theoretically well described by fractal geometry [74]. For example, the number of particles in an aggregate scale with size as [75]

$$N = k_0 \left(\frac{R_\mathrm{g}}{R_0}\right)^{D_\mathrm{f}}, \qquad 2.1$$

where k_0 is a pre-factor with a value close to 1 [76], R_0 is the monomer size, R_g is the radius of gyration and D_f is the fractal dimension. Measured values of D_f typically range from 1.6-2.3 and depend on if the aggregation is diffusion or reaction limited, as well as if it is monomer aggregation or cluster aggregation [73,77,78]. Examples of particle aggregates with different fractal dimensions can be seen in Figure 2.

Equation 2.1 contains the radius of gyration, which is a size estimate typically used when relating angular light scattering to the size of large molecules [48]. Mathematically, radius of gyration is the root mean square distance of the particle mass distribution from the centre of mass. This size estimate is different from for example the hydrodynamic radius as it depends on the mass distribution within the particle, whereas the hydrodynamic radius relates to the outer particle radius. The scaling between the hydrodynamic radius and number of monomers is similar to the radius of gyration, although the exact coefficients are less established [79]. In Papers II and IV, the pre-factor and fractal dimension used to analyse the hydrodynamic radius data were assumed to be similar to those for the radius of gyration (Eq. 2.1). For aggregates consisting of more than ten particles, both simulations and experiments indicate that the ratio between radius of gyration and hydrodynamic radius take a constant value close to 1 [80,81]. Thus, the scaling between the number of particles and aggregate size for aggregates consisting of more than a few particles is the same for both size estimates, where the fractal dimension is most often estimated experimentally via the scaling between parameters such as signal intensity and particle size [82]. Therefore, a minor uncertainty in the pre-factor of the used formula (for example Eq. 2.1) does not affect the ability of differentiating particle aggregates from solid spheres, which is how fractal dimension estimates were used in the appended papers to this thesis.

3

Single-particle optical imaging theory

"The book is about how small particles absorb and scatter light."
"My goodness, who could possibly be interested in that?"[*]

All papers included in this thesis involve using optical microscopy to quantify the motion and signal from particles in the nano-submicron regime with the intent of relating the measurement to particle properties. In both physics and science in general, theory and experiments are inescapably intertwined with each other. In the context of method development, theory is used to predict the potential information that can be extracted from a new method, while experiments that deviate from the current theoretical framework are used to guide future theoretical development. In this chapter, the theoretical background regarding optical imaging of individual particles is presented, with particular focus on the optical scattering from particles that are smaller than the wavelength of the incident light.

Theoretical discussions about optical measurement techniques tend to start with Maxwell's equations, a set of differential equations describing the spatiotemporal evolution of electromagnetic fields [51]. In principle, all classical properties of light can be derived from Maxwell's equations, although the solutions are not seldom challenging to obtain. However, there are also several simplified models to explain the propagation of light and the optical signal from particles interacting with light [22]. The main benefits with the simplified explanation models are that they aid in forming an intuition about the underlying physics and are often simpler to use than starting from Maxwell's equations, although the validity of the approximations needs to be evaluated on a case-by-case basis. Thus, for a rigorous handling of Maxwell's equations, I refer to Jackson [83], Cheng [51], or any of the numerous books on the subject[†].

In the context of this thesis, the theoretical description of the optical signal and imaging theory is based on simplified description models such as:

[*] The quote comes from the introduction of "Absorption and Scattering of Light by Small Particles" by Bohren and Huffman and describes people's reaction when they learned that the authors wrote a book about such a specific topic. To answer their question, according to Google Scholar, by the start of 2023 the book in question has been cited more than 30000 times.
[†] For a book that is freely available online, I recommend "Physics of Light and Optics" [22].

- The angular spectrum method for propagation of optical fields* [22].
- Optical scattering by particles using Rayleigh-Debye-Gans theory, Mie theory, and geometrical optics, which describe the optical signal of particles at different size intervals.

In addition, the differences and similarities between optical scattering and fluorescence are discussed, with a focus on their use for quantitative particle characterisation.

Before describing the theory of optical imaging, some fundamental properties of light need to be established. Although what our eyes and cameras typically register is light intensity, which is proportional to the energy emitted from a light source [51], a full description of light propagation requires more information than that contained in light intensity alone. Instead, the properties of light are described by its optical field, $\vec{E}(x, y, z)$, with the light intensity being proportional to the squared modulus of the optical field [51].

In the context of optical imaging theory, the main differences between the optical field and light intensity are that the field has a phase Φ and a polarisation. As light propagates, the phase changes depending on the distance travelled, Δx, according to $\Delta\Phi \propto \Delta x/\lambda$ [22], where λ is the wavelength of light. For two coherent† optical fields that have travelled different distances before reaching the same spot, their relative phase difference will determine the resulting light intensity (Figure 3) [51]. This property of light is critical both for understanding the measured particle signal as well as for the working principle of interferometric microscopy, which forms the experimental basis of Papers II-V.

The polarisation of light, in turn, describes the direction of the electric field as the electromagnetic wave propagates through space [22]. The direction of the polarisation is important both in the context of scattering from asymmetric particles as well as to describe the interference between optical fields. For spherical particles, the polarisation of the incoming light is of little importance as the scattering in that case is independent of particle orientation. In the context of holographic imaging, which is used in Papers II-V, it is important to consider that only light with the same polarisation interfere, where the polarisation of light can be manipulated by using specialised optical components (Section 5.1).

In addition to phase and polarisation, light waves also have an amplitude, wavelength, and a direction of propagation. These properties are all needed to fully describe the propagation of light, as will become apparent in the following sections.

---

* In optical microscopy, the optical field is often used instead of the electric field. The difference between the two fields is a constant which affects how the fields relate to the measured light intensity, where the light intensity being proportional to the squared modulus of the optical field [45].

† Coherence in this context means that there is a fixed phase difference between the different optical fields. If the two fields are incoherent, their interference will rapidly fluctuate between being constructive and destructive (Figure 3), resulting in a time-averaged signal without interference [22].

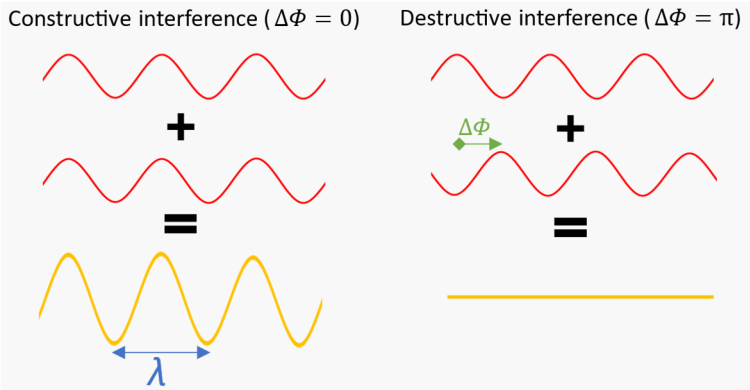

Figure 3 Schematic illustration of the interference properties of light waves. When two different light waves combine, depending on the phase difference $\Delta\Phi$ between the waves, the interference is either constructive or destructive. Note that the image shows the two extreme cases when $\Delta\Phi = 2N\pi$ and $\Delta\Phi = (2N-1)\pi$, where N is an integer. If $\Delta\Phi$ is any other value, the resulting interference pattern will be in between the two presented cases. λ is the wavelength of light.

Note that the classical description of light is used here, in which the properties of light are explained in the context of a continuous wave and not as a photon. Since an image typically involves measuring the contribution of numerous photons, the classical description of light describes the occurring physics well. Nevertheless, the quantum properties of light are still needed to understand some optical processes such as fluorescence [84,85], lasers [86] and shot noise in experimental images [87]. Thus, apart from the wavelength selectivity of fluorescence, the properties of light will henceforth be described as electromagnetic waves.

3.1 Propagation of optical fields using angular spectrum

One starting point to describe the propagation of light is the plane wave solution to Maxwell's equations, as the propagation of a general optical field in a homogenous environment can be described as a sum of plane waves [45]. In free space, Maxwell's equations become the Helmholtz equation [51]:

$$\nabla^2\vec{E}(x,y,z) + k^2\vec{E}(x,y,z) = \vec{0}, \qquad 3.1$$

which has the solution $\vec{E}(x,y,z) = \vec{E}_0 e^{-i(\vec{k}\cdot\vec{r})}$, where $\vec{k}$ is the wave vector that defines the direction of propagation with $|\vec{k}| = k = 2\pi/\lambda$. This solution is often referred to as the plane wave solution, as the optical field is constant over a plane orthogonal to the wave vector. Moreover, any $\vec{k}$ that fulfil $|\vec{k}| = 2\pi/\lambda$ is a valid solution to the Helmholtz equation. Using this set of solutions as a basis, any optical field in free space can be written as sum of plane waves [45]:

$$\vec{E}(x,y,z) = \iint_{k_x^2+k_y^2\leq k^2} \vec{A}(k_x,k_y) e^{-i\left(k_x\cdot x + k_y\cdot y + \sqrt{k^2-k_x^2-k_y^2}\cdot z\right)}\, \mathrm{d}k_x \mathrm{d}k_y, \qquad 3.2$$

where $\vec{A}(k_x, k_y)$ is a complex-valued pre-factor. Note that for each choice of k_x and k_y the magnitude of k_z is also determined by the requirement that $|\vec{k}| = 2\pi/\lambda$, where the sign of k_z indicates the propagation direction.

When inspecting Eq. 3.2, its structure is similar to that of the two-dimensional Fourier transform [88]. Therefore, Eq. 3.2 can be written as:

$$\vec{E}(x,y,z) = \boldsymbol{\mathcal{F}}\left(\vec{A}(\vec{k})e^{-i\sqrt{k^2-k_x^2-k_y^2}\cdot z}\,\mathrm{circ}\left(\frac{\sqrt{k_x^2+k_y^2}}{k}\right)\right), \qquad 3.3$$

where $\boldsymbol{\mathcal{F}}$ is the two-dimensional Fourier transform operator and circ is a function whose value is zero except when the argument is between zero and one, in which case the function takes the value of one. By applying the inverse Fourier transform to Eq. 3.3,

$$\vec{A}(\vec{k})e^{-i\sqrt{k^2-k_x^2-k_y^2}\cdot z}\,\mathrm{circ}\left(\frac{\sqrt{k_x^2+k_y^2}}{k}\right) = \boldsymbol{\mathcal{F}^{-1}}\left(\vec{E}(x,y,z)\right). \qquad 3.4$$

Hence, once the optical field is known at any one plane, $\vec{A}(\vec{k})$ can be obtained using Eq. 3.4. When $\vec{A}(\vec{k})$ is known, the optical field at any other plane is also known by the use of Eq. 3.3. This way of numerically propagating the optical field is called propagation of angular spectrum (PAS) [45].

Note that Eqs. 3.2-3.4 only describe the simplified situation of propagation in a constant environment. In most real-life situations, the imaging system contains several optical components such as lenses and apertures (see for example Figure 10 in Section 5.1.1). If an optical component is located along the path of the optical field, the subsequent propagation is affected. The mathematical procedure to handle this is to evaluate the optical field just before the component, calculate the change of the optical field it induces, and then initiate a new propagation after the component [22]. For this reason, the calculations become challenging to perform analytically for optical systems with more than just a few components.

The benefits of PAS compared to alternative propagation methods such as the Huygens–Fresnel method [45] are that (i) it is possible to propagate the optical field over short distances, (ii) it is a more general formalism of the optical field, and (iii) the numerical propagation can be performed using Fourier transforms, which can be efficiently calculated on modern computers. One of the main drawbacks of PAS is that the density of numerical sampling points is the same throughout the propagation, which makes it inefficient at propagating distances much longer than the wavelength of light. In Papers II-V, optical propagation was used to numerically refocus images a distance ranging from a few nanometres to a few micrometres. For this reason, PAS was used to propagate the obtained optical fields from off-axis holography (Section 5.1.1).

3.2 Spatial resolution of optical microscopy

When inspecting Eq. 3.2, the integral is carried out over all k_x and k_y values that fulfils $|\vec{k}| = 2\pi/\lambda$. In an image, the values of k_x and k_y can be viewed as spatial frequencies [45], which enables understanding of the resolution using Fourier analysis [86]. From Fourier analysis, a larger range of included frequency values leads to a reduced width of the signal distribution [88]. As the range of k_x and k_y values is limited by the wavelength, the wavelength also limits the spatial resolution. The definition of the spatial resolution limit varies between different optical techniques as it depends on the details of the recorded signal [89]. However, as a rule of thumb the resolution limit is λ/NA, where NA is the numerical aperture and describes the range of scattering angles captured by the objective lens [90].

At this point it is important to distinguish between detecting a particle and resolving a particle. To resolve a particle, it needs to be distinguished from potential neighbouring particles. If two objects are close enough such that their optical signals spatially overlap, they will at a certain distance no longer be distinguishable [22]. The shortest distance for which the individual particles are distinguishable is referred to as the spatial resolution limit. However, as long as the optical signal is sufficiently large and separated from the signal of other nearby particles, a particle is theoretically detectable in a microscope no matter its geometrical size. For such particles the centroid position and integrated particle signal can be accurately quantified. This property of optical microscopy forms the basis of particle characterisation using particle tracking [91], which is the main experimental approach in all appended papers to this thesis.

3.3 Optical signal from small particles

In a homogenous environment, light propagates as described in Section 3.1, where the only distance dependent factor is $\exp\left(-i\sqrt{k^2 - k_x^2 - k_y^2} \cdot z\right)$ (Eq. 3.2). For Eq. 3.2 to be valid, the optical properties of the medium need to be the same across the region where the optical field is located. When it comes to optics and the optical signal from particles, the important material property is the complex-valued refractive index n, the imaginary part of which relates to light absorption and its real part relates to light scattering (Sections 3.3.3-3.3.5) [22]. Following this reasoning, for deviations from ordinary optical propagation to occur, as for example optical scattering, there need to be spatial variations in refractive index [92].

In a similar way to the propagation of light, where the optical field is described as a sum of plane wave contributions, the scattering from a small* weakly optically interacting† particle can be described by subdividing it into smaller regions where the scattering

* Small refers to that the particle is smaller than the wavelength of the incident light.
† Weakly optical interacting particle means that the absolute difference in refractive index between the particle and the surrounding medium is much smaller than one.

from each subregion is acting as a wavelet [92]. The starting point for such an analysis is the scattering from a particle in the point-like limit [92]:

$$\vec{E}_{\mathrm{s}} = \frac{e^{-\vec{k}\cdot\vec{R}}}{-ik|\vec{R}|} S \begin{pmatrix} \cos(\theta) & 0 \\ 0 & 1 \end{pmatrix} \vec{E}_{\mathrm{in}}, \qquad 3.5$$

where $\vec{E}_{\mathrm{in}}$ is the incident optical field, $\vec{R}$ is the spatial coordinate vector, θ is the angle between the directions of the incident and scattered optical field, and S contains the material properties. The expression for S is

$$S = -v \frac{3ik^3}{4\pi} \frac{n_{\mathrm{p}}^2 - n_{\mathrm{m}}^2}{n_{\mathrm{p}}^2 + 2n_{\mathrm{m}}^2}, \qquad 3.6$$

where n_{p} and n_{m} are the refractive indices of the particle and the surrounding medium, respectively, and v is the volume of the point-like particle element. Of importance for characterisation of nanoparticles is that the optical field from a point-like particle is proportional to its polarizability $\alpha \equiv 3v(n_{\mathrm{p}}^2 - n_{\mathrm{m}}^2)/(n_{\mathrm{p}}^2 + 2n_{\mathrm{m}}^2)$ [93], which infers that both particle volume and refractive index information are experimentally available.

For weakly optically interacting particles beyond the point-like size limit, it is typically assumed that the excitation of each subdivided region to a first approximation is independent of the presence of the particle [92]. With this assumption, the particle scattering is the same as in Eq. 3.6 except for a correction factor f, typically referred to as the optical form factor, which describes the interference in the far-field from the different subdivided regions of the particle [92]. Mathematically, if the particle consists of a single material, f is expressed as

$$f(\theta, \phi) = \frac{1}{V} \int_V e^{-i\Delta\Phi(\theta,\phi)} \, \mathrm{d}v, \qquad 3.7$$

where V is the particle volume that contains material, $\Delta\Phi(\theta, \phi)$ is the phase difference of light contributions originating from different subregions $\mathrm{d}v$, and the angles θ and ϕ indicate that the phase difference between different scattering elements depends on the direction of the incident and scattered light. Examples of phase differences for different angles between the incident and scattered light are schematically shown in Figure 4 in the case of a spherical shell*, where the larger the directional difference between the incoming and scattered light the larger the relative phase difference†. This description of light scattering from particles is commonly called Rayleigh-Debye-Gans theory. From Eq. 3.7, the optical form factor for various particle shapes can be readily estimated as long as the assumption of small weakly optically interacting particles is valid ($|n_{\mathrm{p}} - n_{\mathrm{m}}| \ll 1$ and $2kR|n_{\mathrm{p}} - n_{\mathrm{m}}| \ll 1$, where R is the particle radius [92]), which often is the case for biological particles and particle aggregates as the difference between particle and media refractive index is small.

* A spherical shell is often used to approximate the signal from lipid vesicles (Section 2.1).
† In the case of rotational symmetric particles, but not necessarily true for asymmetric particles.

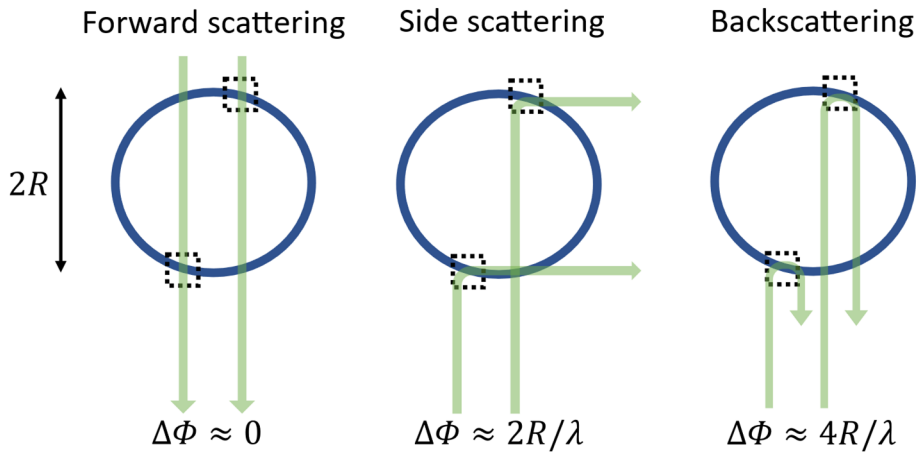

Figure 4 Illustration of how the relative phase difference ($\Delta\Phi$) between different scattering elements depends on the measured scattering direction. In the forward scattering direction (left) the relative phase difference is approximately zero. In the side scattering direction (middle) the relative phase difference is non-zero but smaller than that for the backscattered light (right), which is the direction with the largest relative phase difference. R is the particle radius and λ is the wavelength of light.

3.3.1 Examples of optical form factors for sub-wavelength sized particles

Analytical solutions to Eq. 3.7 can only be obtained in some special cases, which includes most of the investigated particles shapes in this thesis such as homogenous spheres, lipid vesicles, and particle aggregates (Section 2). In the case of a rotationally symmetric particle consisting of a single material, the optical form factor is [75]

$$f(q,R) = A\int_0^R r^2 \frac{\sin(rq)}{rq}\rho(r)\mathrm{d}r, \qquad 3.8$$

where $\rho(r)$ is the radial material distribution, A is a normalisation constant such that $f(q=0,R)=1$ and

$$q = \left|\vec{k}_{\mathrm{in}} - \vec{k}_{\mathrm{out}}\right| = \frac{4\pi}{\lambda_0} n_{\mathrm{m}} \sin(\theta) \qquad 3.9$$

describes the difference in wave vectors between the incoming and outgoing light. Note that λ_0 refers to the wavelength in vacuum. When $Rq \ll 1$, $1 - f(q,R)$ becomes similar to the equation for radius of gyration (R_{g}) [48]*. For larger particles the relation between $f(q,R)$ and radius of gyration eventually breaks down, but the similarity between the two particle characteristics can still be used to understand the relative difference in optical form factor between different types of particles (Figure 5).

In the case of thin-shelled particles, such as a lipid vesicle, $\rho(r) = 0$ except for the shell, inferring that $f(q,R) \approx \sin(Rq)/(Rq)$ [94]. For homogenous spheres $\rho(r) = 1$ up to the outer radius, which inserted into Eq. 3.8 becomes $f(q,R) = 3[\sin(Rq) - Rq \times \cos(Rq)]/(Rq)^3$ [48]. Particle aggregates (Section 2.3) is a special case as the aggregates themselves are not rotationally symmetric although the optical form factor

* Radius of gyration is the second moment of the mass density (Section 2.3).

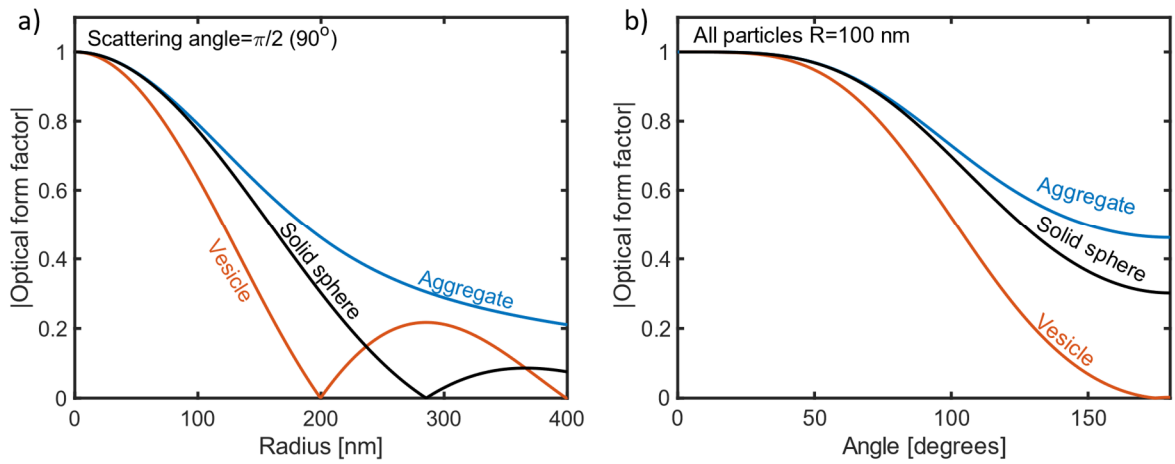

Figure 5 The optical form factor from Rayleigh-Debye-Gans theory for homogenous spheres, lipid vesicles, and aggregates with a fractal dimension of 2 using a wavelength of 532 nm and a surrounding medium refractive index of 1.33. The optical form factor as a function of (a) size when the scattering angle is 90 degrees and (b) as a function of scattering angle for a particle with a radius of 100 nm.

when relating the optical signal to particle properties approximates them as such [75]. For details, see Ref. [75]. Instead of replicating the derivation, the optical form factor is here plotted for an aggregate* with $D_f = 2$ to enable a visual comparison with thin-shelled particles and homogenous spheres (Figure 5).

Although Eq. 3.7 at first glance seems mathematically cumbersome, it can be used to interpret the relative importance of $f(q, R)$. The size limit when the optical form factor starts to significantly influence the optical signal can be approximated as the radius when $Rq = 1$, which occurs in the case of visible wavelengths for $R = 30 - 60$ nm when $\theta = 90^o$, $R = 20 - 40$ nm when $\theta = 180^o$, and $R \approx \infty$ when $\theta = 0^o$. Thus, the size-signal scaling is different for transmission methods and methods which measure at other scattering angles, as displayed in Figure 5. Since $f(q, R) \approx 1$ for transmission methods, the particle signal can directly be related to particle properties such as particle mass without the need of particle size or shape information, whereas non-transmission methods require size and shape information to estimate particle mass when $Rq > 1$. However, the size and shape dependence of the particle signal in non-transition methods can be combined with transmission measurements to estimate particle size directly from the optical signals [48,95]. This was utilised in Paper V, where further details of the used method are discussed in Section 5.3.

3.3.2 Mie theory

In the case of homogenous spherical particles, there exists an analytical solution to the optical scattering that is valid both dielectric particles and metallic particles. This solution was first derived by Gustav Mie and is commonly referred to as Mie theory [93]. Mie theory solves the optical scattering as an infinite sum of spherical polynomials [93], and is primarily used in numerical calculations of the optical

* For aggregates consisting of more than a few particles the monomer size does not affect the optical form factor [75], in which case the optical form factor depends only on the fractal dimension.

signal [96–98]. In the limit of small weakly optically interacting particles, such as biological nanoparticles, Mie theory and Rayleigh-Debye-Gans theory gives approximately the same results [92].

In optical particle characterisation, the use of Mie theory depends on the size of the particle. For particles larger than the wavelength of light, Mie fitting to the scattering pattern in microscopy images is used to quantify particle size, refractive index, shape, and position [99–101]. When the particle size becomes comparable to the wavelength of light, the ability of simultaneously quantifying particle size and refractive index from Mie fitting alone eventually becomes limited by the spatial resolution of the microscope. To improve the smallest particle size for which both particle size and refractive index can be extracted from an optical microscopy image, in Paper III the Mie calculations were complemented with information about the spatial resolution of the microscope and experimental noise to better mimic the optical signal during the particle characterisation. For even smaller particles, as for example nanoparticles, it is currently not possible to simultaneously quantify both particle size and refractive index from the scattering pattern in a microscopy image. Mie simulations are then used to get information regarding how the optical signal scales with one or more parameters, such as size, refractive index, wavelength or scattering angle [102]. In Papers II and V, Mie calculations were used for that purpose. All Mie calculations in the appended papers to this thesis are based on the freely available MATLAB package MatScat [96].

3.3.3 Local phase shifts and the complex-valued optical signal

Biological samples typically have a real-valued refractive index only slightly higher than that of water [103][*]. For this reason, the intensity contrast when imaging for example living cells using transmission light microscopy is low when the cells are in focus [104]. Instead, the presence of the cell mostly alters the local phase of the light [105]. If the particles are large enough to be described by geometrical optics, which requires that the particle size is several times larger than the used wavelength of light, the local phase shift $\Delta\Phi$ is

$$\Delta\Phi(x,y) = \frac{2\pi}{\lambda_0} h(x,y)\Delta n(x,y) \qquad 3.10$$

where h is the local height of the cell/particle. If the refractive index inside the structure of interest is homogenous, an integration over the phase shift gives

$$\iint \Delta\Phi \mathrm{d}x\mathrm{d}y = \frac{2\pi}{\lambda_0}\Delta n \iint h(x,y)\mathrm{d}x\mathrm{d}y = \frac{2\pi}{\lambda_0} V\Delta n. \qquad 3.11$$

This relation is commonly used to estimate refractive index of both living cells [106,107] and submicron-sized particles [108,109]. In Paper II, in addition to quantifying the refractive index difference between the particles and the medium, the sign of Eq. 3.11 was used to differentiate nanobubbles from solid particles as

[*] Different parts of the cell have different refractive indices, but in general the refractive index is less than 1.4 [103]. Biological nanoparticles such as viruses can have a refractive index up to 1.48 [15].

nanobubbles have an refractive index less than the surrounding media (water) whereas potential solid dielectric particles have an refractive index higher than the surrounding water.

In the context of biological particles, it is common to relate the integrated phase shift to dry mass [110,111], where the name comes from that the mass estimate is based on the phase difference to the surrounding media which often consists of water. The relation between integrated phase shift and dry mass is based on an approximately linear relation between material concentration C and refractive index difference between the particle and the surrounding media, $\Delta n = C(\mathrm{d}n/\mathrm{d}c)$. When inserted into Eq. 3.11 it becomes

$$\frac{2\pi}{\lambda_0} V\Delta n = \frac{2\pi}{\lambda_0}\frac{\mathrm{d}n}{\mathrm{d}c} VC = \frac{2\pi}{\lambda_0}\frac{\mathrm{d}n}{\mathrm{d}c} m_{\mathrm{dry}}, \qquad 3.12$$

where m_{dry} is the dry mass. The value of $\mathrm{d}n/\mathrm{d}c$ varies slightly between different biomolecules, where the average value is 1.8×10^{-4} m^3/kg [110]. Since the refractive index of a biological particle scales with biomolecular concentration, it is possible to distinguish different biological particles from each other based on the obtained particle refractive index. This property of refractive index estimations was used in Paper IV to analyse whether the observed particles correspond to intact viruses or if they had lost material due to interacting with functionalised gold nanoparticles (AuNPs).

In the case of twilight off-axis holography (Section 5.1.2), it can be convenient to work with the optical field instead of the phase shift. In the case of particles with a signal that is much smaller than the background illumination signal, the imaginary part of the optical field from a particle, $\Im(E_{\mathrm{p}})$, is related to particle phase shift via

$$\iint \Delta\Phi \mathrm{dA} = \iint \arctan\left(\frac{\Im(E_{\mathrm{p}})}{1+\Re(E_{\mathrm{p}})}\right) \mathrm{d}A \approx \iint \Im(E_{\mathrm{p}}) \mathrm{d}A. \qquad 3.13$$

This relation was used in Paper IV in combination with the simultaneously obtained hydrodynamic radius to estimate particle refractive index.

3.3.4 Light extinction and the complex-valued optical signal

When the complex-valued optical field from a particle is measured, both the imaginary and real part contain quantitative particle information. To understand the information content in the real part of the optical field, one starting point is its relationship with the measured light intensity, I_{im}. This relation comes from the equation representing the interfering field in an image,

$$I_{\mathrm{im}}/I_0 = \left|1 + E_{\mathrm{p}}\right|^2 = 1 + 2\Re(E_{\mathrm{p}}) + \left|E_{\mathrm{p}}\right|^2 \approx 1 + 2\Re(E_{\mathrm{p}}), \qquad 3.14$$

where I_0 is the image intensity in the absence of a particle and it is assumed that $|E_{\mathrm{p}}| \ll 1$. The change in I_{im} caused by the presence of a particle is therefore to a first approximation $\Delta I_{\mathrm{im}}/I_0 = 2\Re(E_{\mathrm{p}})$. A general property of particles and molecules is that their presence most often decrease the transmitted light intensity through the sample,

which is captured by Beer's law*. The decrease in measured light intensity in an image from a single particle can therefore be related to both a change in the real part of the optical signal and the optical extinction (or attenuation) cross section σ_{ext}:

$$\iint_S \frac{-\Delta I_{\text{im}}}{I_o} \mathrm{d}A = \begin{cases} \sigma_{\text{ext}} \iint_S \frac{1}{S} \mathrm{d}A = \sigma_{\text{ext}} \text{ (Beer's law)} \\ -\iint_S 2\Re\left(E_{\text{p}}\right) \mathrm{d}A \text{ (Eq. 3.14)} \end{cases}. \quad 3.15$$

Equating the two right-hand equations in Eq. 3.15 results in

$$\iint \Re(E_{\text{p}}) \mathrm{d}A = -\frac{\sigma_{\text{ext}}}{2}. \quad 3.16$$

A large σ_{ext} compared to the particles geometrical cross section is associated with a complex-valued refractive index that is significantly different from that of surrounding media, which is the case for metals such as gold when in water [93]. Thus, σ_{ext} is much larger for gold nanoparticles (AuNPs) than for biological nanoparticles, which enables distinction between the two types of particles by comparing their relative real and imaginary parts of the optical field.

In Paper IV, the detected particles complexes comprised of both metallic nanoparticles and dielectric particles. When the amount of bound metallic nanoparticles in a particle complex is low enough such that the light extinction of each metallic nanoparticles is to first approximation unaffected by the presence of other nanoparticles in the particle complex, then the extinction cross section of the particle complex can be approximated as the sum of the individual extinction cross sections, $\sigma_{\text{ext}} \approx \sum \sigma_{\text{ext}}(\text{monomer})$. Thus, if the extinction cross section of the metallic nanoparticles in the particle complex is known and the extinction contribution from the dielectric particle is much less than that of the bound metallic nanoparticles, the number of bound metallic nanoparticles in a particle complex can be estimated from the integrated real part as

$$N = -\frac{2}{\sigma_{\text{ext}}} \iint \Re(E_{\text{p}}) \mathrm{d}A. \quad 3.17$$

This equation was used in Paper IV to estimate the amount of bound AuNPs in detected particle complexes.

3.3.5 The relation between different optical characterisation methods

Although scattering-based microscopy and quantitative phase microscopy traditionally are viewed as different measurement approaches, their measured particle signals are related. To show this similarity, it is instructive to derive the relation between particle polarizability α and integration of the optical field at the camera plane [113]. This can be achieved by using the relation between polarizability with the dipole moment $\vec{p}$ and the incoming illumination $\vec{E}_0$ [92],

* Beer's law states that the absorbance scales linearly with the concentration, path length in the sample, and the molar attenuation coefficient [112].

$$\frac{\vec{p}\cdot\vec{E}_0^*}{\vec{E}_0\cdot\vec{E}_0^*} = \epsilon_0\epsilon_\mathrm{m}\alpha, \qquad 3.18$$

where ϵ_m is the relative dielectric constant of the medium and ϵ_0 is the dielectric constant. By modelling the optical field of a nanoparticle imaged through a microscope, Eq. 3.18 can be used to find a relation between the measured optical field and polarizability, where the details in the case of plane wave illumination are shown in Ref. [113]. Using the end results of the derivation in the small particle limit [113]*:

$$\alpha = \frac{i\lambda_0}{n\pi}\iint\left(1-\frac{t(x,y)}{t_0}\right)\mathrm{d}A = \frac{-i\lambda_0}{n_\mathrm{m}\pi}\iint E_\mathrm{p}\mathrm{d}A, \qquad 3.19$$

where t is the transmittance, t_0 is the transmittance when the particle is absent, and E_p is the optical field from a particle.

To relate the integrated phase from a nanoparticle to for example the signal measured in darkfield microscopy, it is instructive to first relate integrated phase to polarizability. In the case of a small refractive index difference between the particle and the surrounding media, the polarizability can be approximated as [92]

$$\alpha \equiv 3V\frac{n_\mathrm{p}^2-n_\mathrm{m}^2}{n_\mathrm{p}^2+2n_\mathrm{m}^2} \approx 2V\Delta n/n_\mathrm{m}, \qquad 3.20$$

where $n_\mathrm{p} = \Delta n + n_\mathrm{m}$. In the case of real-valued refractive indices, as for dielectric particles in water, Eqs 3.18-3.20 relates the integrated phase with particle polarizability as

$$\iint \Delta\Phi\mathrm{d}A \approx \iint \Im\big(E_\mathrm{p}\big)\mathrm{d}A = \frac{n_\mathrm{m}\pi}{\lambda_0}\Re(\alpha) \approx \frac{2\pi}{\lambda_0}V\Delta n, \qquad 3.21$$

where that the right-hand side of the equation is the same as Eq. 3.11. Thus, in the small particle limit the integrated phase is the same as the real part of the polarizability and an integration of the complex-valued optical field is related to the complex-valued polarizability.

Light scattering microscopy methods most often measure either the scattering cross section σ_sca or the extinction cross section σ_ext. For example, darkfield microscopy measures $\sigma_\mathrm{sca}|f(q,R)|^2$ and the transmission method coherent bright field microscopy (COBRI) measures the light extinction modulated with the Gouy phase [114]. Since the polarizability is related to the different optical cross sections as [93]:

$$\sigma_\mathrm{sca} = \frac{k^4}{6\pi}|\alpha|^2 \qquad 3.22$$

$$\sigma_\mathrm{abs} = k\Im(\alpha), \qquad 3.23$$

* In Ref. [113] they define the particle polarizability differently, which causes a difference of n_m^2 from the expression shown here.

where $\sigma_{\text{ext}} = \sigma_{\text{sca}} + \sigma_{\text{abs}}$ and σ_{abs} is the absorbance cross section, this shows that the information contained in the scattering cross section is present in measurements of the complex-valued optical field. Thus, if the optical field is measured using off-axis holography as in Papers II-V, additional optical measurements of the same particles using for example darkfield microscopy do not add any additional particle information unless the detection limit or the measurement geometry are different. The strengths and weaknesses of different optical microscopy methods in the context of characterising subwavelength-sized particles are further discussed in Section 5.7.

3.3.6 Optical particle characterisation beyond the small particle limit

When the particle size increases, the relation between the measured optical signal and particle properties is not necessarily the same. For example, the expression between polarizability and particle properties is derived in the quasi-static limit, where the linearity between polarizability and particle volume is only valid when the particle size is much smaller than the wavelength of light [93].

In this context, Sections 3.3.3 and 3.3.5 intend to illustrate that the relation between integrated phase and particle properties is to a first approximation the same in both the small and large particle limits. Combined with the fact that the integrated phase shift obtained from simulations scale with particle volume in the intermediate size regime between nanoparticles and micrometre-sized particles [108], this implies that the relation $\iint \Delta\Phi \mathrm{d}A = 2\pi V \Delta n/\lambda_0$ is valid for particle sizes ranging from nanoparticles to cells and beyond as long as $\Delta n \ll 1$. By association, the relation between the optical field and the particle polarizability formula can also be used to estimate particle properties in the same size regime. For this reason, the complex-valued optical field can be related to particle properties in the nano-submicron size regime without particle shape assumptions, which motivated its use in Papers II-V.

3.4 Fluorescence

In scattering-based optical microscopy all heterogeneities in the spatial distribution of refractive index will contribute to the optical signal. For this reason, label-free scattering-based microscopy naturally lacks specificity. This is advantageous for generic particle characterisation, but to identify specific entities in crowded environments it can be advantageous to have signal specificity.

There are several classes of optical measurement techniques that have a specific optical signal, including fluorescence [84], Raman [29], and Brillouin scattering [115]. For biological nanoparticles, the most commonly used technique is fluorescence. Fluorescence is a subclass of luminescence, which is the process where light is emitted from energetically excited molecules [84]. In fluorescence, the initial excitation originates from absorption of a photon of a particular wavelength and the subsequently emitted photon typically has a lower energy than the incident photon [84]. This shift in energy originates from that the excitations are linked to a vibronic transition, in which the molecule changes both its electronic and vibrational state, a process that is often

visualised using a Jablonski diagram (Figure 6) [116]. Since vibrational relaxations occur on a faster time scale than the electron relaxation, the vibrational relaxations will cause the emitted photon to have lower energy than the initially absorbed photon [84].

In modern optical microscopes, it is now routine to detect the fluorescence signal from single fluorophores [18,117]. For this reason, fluorescent labelling can be used to detect otherwise weakly optically interacting particles, as used in Paper I to obtain a signal from the lipid vesicles and the supported lipid bilayer (SLB) to enable particle tracking and evaluation of the SLB formation.

Regarding quantitative particle characterisation, fluorescence and optical scattering are conceptually different. First, fluorescence can be used to identify the presence of certain particle subgroups using molecular markers [118], whereas the scattering signal only gives information about the presence of the particle and its polarizability. Second, fluorescence can be used to track labelled particles in crowded environments [28], which only is possible when using scattering if the particle of interest has a much larger polarizability than the surrounding particles, as in the case of gold nanoparticle labelling [119]. Third, relating signal intensity to particle properties such as size is in general much more difficult using fluorescence than scattering. For example, the fluorescence signal is sensitive to aspects such as bleaching, the local chemical environment, and labelling efficiency [84]. The fluorescence signal does therefore not always scale with particle size as expected [120–122], whereas the scattering signal does not change over time unless the particle or the surrounding media changes. To achieve both specificity and a quantitative signal it is possible to simultaneously measure fluorescence and light scattering, which is common when investigating the scattering signal in complex environments such as inside living cells [123,124].

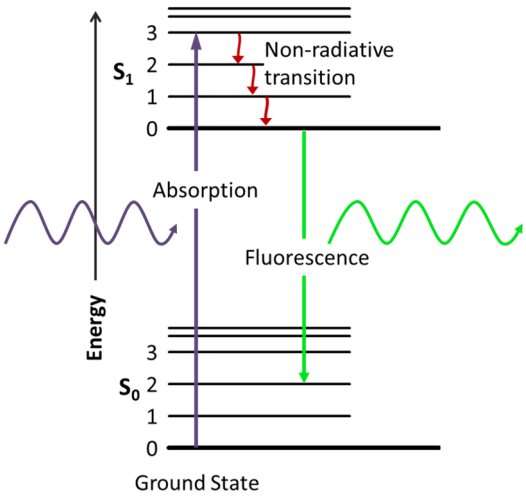

Figure 6 Jablonski diagram. An incoming photon of a particular wavelength is absorbed, which changes both the electronic and vibrational state of the molecule. The electronic state is indicated by S_i and the vibrational state is the number next to each plateau. Since the vibrational relaxations occur on a faster time scale than the electron relaxation, the system will relax to the lowest vibrational state before emitting a photon at a lower wavelength than the initial excitation. The image is adapted from Wikimedia [125] under CC0 1.0 licence.

4

Brownian motion

The story of Brownian motion is one of confused experiment,
heated philosophy, belated theory, and, finally, precise and
decisive measurement
- M. D. Haw, 2002 [12]

One of the most prominent examples of the intertwined relationship between experiment and theory is Brownian motion, where over a century of research is captured in the quote in the beginning of this chapter. When analysing the motion of suspended particles in a viscous fluid, one part is deterministic, which imply that the particle motion follows the flow of the surrounding fluid, and another will appear to be stochastic. The stochastic part of the motion is commonly referred to as Brownian motion, where the relation between Brownian motion and particle properties is used in all papers of this thesis.

In this chapter, the theoretical discussion is centred around Brownian motion and its dependence on particle size, hydrodynamic boundary conditions, confinement, and tethering to a fluid surface, as well as practical aspects of using Brownian motion in optical particle characterisation. For details about hydrodynamics of particles beyond the scope of this thesis, I refer to the book by Happel and Brenner [126].

After Einstein's initial derivation [14], several equations describing Brownian motion have been derived [127]. Starting from Newton's equations, the motion of a suspended particle with a low Reynolds number* when neglecting gravity follows [126]:

$$m\frac{\mathrm{d}v(t)}{\mathrm{d}t} = -\gamma(v(t) - v_{\mathrm{fluid}}), \qquad 4.1$$

where γ is the friction coefficient from the fluid acting on the particle, m is particle mass, $v(t)$ is the particle velocity, and v_{fluid} is the bulk velocity of the fluid. From Eq. 4.1, it follows that $v(t) \to v_{\mathrm{fluid}}$ as $t \to \infty$. However, one central concept in statistical physics is thermal fluctuations. In particular, the equipartition theorem states

* One common approximation used to solve the Navier-Stokes equations, which describe the motion of fluids, is to assume that viscous forces dominate inertial forces. This approximation is valid for particles when their Reynolds number, (fluid density)×(velocity)×(size)/(viscosity), is less than 0.05 [126].

that if a system is in thermal equilibrium, every degree of freedom contributes $(1/2)k_{\mathrm{B}}T$ to the total energy of the system, where k_{B} is Boltzmann's constant and T is the temperature in Kelvin [127]. Since the motion of the particle should be consistent with the equipartition theorem when $v_{\mathrm{fluid}} = 0$, Eq. 4.1 does not correctly describe the full motion of a suspended particle.

The missing contribution to the particle motion in Eq. 4.1 is that individual molecules in the fluid may deviate from the average fluid flow and bump into the particle such that it changes velocity, an effect that is typically described as a stochastic force. As a special case of the fluctuation-dissipation theorem [127,128], whenever there is dissipation, such as friction between a particle and the surrounding fluid, there is also a stochastic force present when the system obeys detailed balance [127]. When adding a stochastic force $\xi(t)$ to Eq. 4.1, it changes Newton's equation to the following Langevin equation [129]:

$$m\frac{\mathrm{d}v(t)}{\mathrm{d}t} = -\gamma(v(t) - v_{\mathrm{fluid}}) + \xi(t). \qquad 4.2$$

The measured particle motion is most often related to particle properties using the mean squared displacement. The relation between particle properties and the mean squared displacement starting from Eq. 4.2 while assuming that the stochastic force lack time correlation is derived in several books about the subject [33,127], and will not be reproduced here. Using the end-result of such derivations, the mean squared displacement when the particle is in equilibrium with the fluid is:

$$\langle (x(t) - x_0)^2 \rangle_{\mathrm{T}} = \frac{2k_{\mathrm{B}}T}{\gamma}\left[t - \frac{m}{\gamma}\left(1 - e^{-(\gamma/m)t}\right)\right]. \qquad 4.3$$

where $\langle \quad \rangle_{\mathrm{T}}$ denote the time average in equilibrium. If the effect of inertia is neglected, the mass-dependent terms in Eq. 4.3 can be dropped, which simplifies Eq. 4.3 to

$$\langle (x(t) - x_0)^2 \rangle_{\mathrm{T}} = \frac{2k_{\mathrm{B}}T}{\gamma}t = 2Dt, \qquad 4.4$$

where $D = k_{\mathrm{B}}T/\gamma$ is the diffusion constant. From Eq. 4.4 it follows that the mean squared displacement scales linearly with time, allowing the diffusion constant to be quantified from a linear fit (Figure 7) [33,130]. Deviations from such a linear behaviour is an indication of anomalous diffusion, which is linked to non-freely diffusing particles and phenomena such as active transport [131,132].

In the case of a freely diffusing spherical particle, the diffusion constant is related to its hydrodynamic radius R_{h} via the Stokes-Einstein equation [126],

$$D = \frac{k_{\mathrm{B}}T}{6\pi R_{\mathrm{h}}\eta}, \qquad 4.5$$

where η is the viscosity of the fluid. Thus, measurements of the mean squared displacement enable estimates of the hydrodynamic radius. However, the hydrodynamic radius is not necessarily the same as the geometrical radius R. This difference is further discussed in Section 4.1.

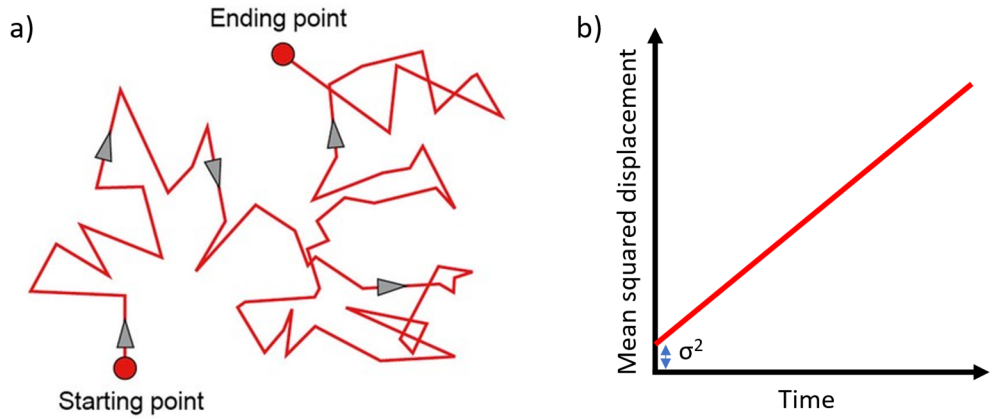

Figure 7 Schematic images describing Brownian motion. (a) Plot of the particle postion at discrete time steps when undergoing Brownian motion. (b) The mean squared displacement, $\langle (x(t) - x_0)^2 \rangle_T$, over time, which is linear for ordinary Brownian motion. The slope relates to the diffusion constant of the particle and the offset σ^2 from origin relates to position uncertainty (Section 4.3). The image in (a) is taken from Wikimedia [133] under CC BY-SA 4.0 licence.

4.1 Hydrodynamic boundary conditions

Hydrodynamics follows the Navier-Stokes equations, which are a set of partial differential equations describing the motion of viscous fluids [126]. However, the hydrodynamic boundary conditions cannot be derived from first principles [134]. Instead, the boundary conditions need to be assumed or measured. For systems larger than a millimetre, the exact boundary condition has a very minor influence on the overall system. But as the dimensions of the system become smaller, as is the case for diffusing nanoparticles, the relative importance of the boundary condition increases.

The boundary conditions are typically divided into three cases: no slip, partial slip, and perfect slip, as schematically exemplified in Figure 8. The no-slip boundary condition corresponds to that the velocity of the fluid parallel to the surface is zero at the transition between the fluid and the solid interface [134]. No slip is frequently observed for hydrophilic surfaces [135]. Since nanoparticles require hydrophilicity for a good dispersion in water, the no-slip boundary condition is commonly assumed unless the surface has been modified to make it hydrophobic [136].

Partial slip occurs when the friction at the fluid-solid boundary is finite [134]. The velocity of the fluid behaves as if the no-slip boundary condition still occurs but for an effective surface inside the solid material. The distance between the true and the virtual interface is referred to as the slip length b, as illustrated in Figure 8. Experimental measurements of slip length, using for example a surface force apparatus, typically range from 0 to a few tens of nanometres [40], where the general trend is that the slip length increases with increasing hydrophobicity and surface roughness [135]. Perfect slip is a special case of partial slip that is characterised by a slip length that approaches infinity, which is a useful approximation when the slip length is much longer that the length scale of the system [137].

The existence of non-zero slip is not only of theoretical importance; it also affects the relation between experimental results and physical properties of the system. For example, in the case of diffusing spherical particles, a non-zero slip length changes the standard Stokes-Einstein equation to [137]:

$$D_{\mathrm{b}} = \frac{R+3b}{R+2b}\frac{k_{\mathrm{B}}T}{6\pi\eta R}, \qquad 4.6$$

where R is the geometrical radius of the particle and b is the slip length. From this equation it is apparent that the relation between the diffusion constant and particle radius can change up to a factor of 3/2 depending on the relative length of the slip and the particle size. In Paper I, in which the hydrodynamic boundary condition was investigated, Eq. 4.6 was used to relate particle diffusivity to size. In Papers II-V, the investigated particle sizes were all much larger than the potential slip length, which imply that potential partial slip has a minor effect on the diffusivity-size relation and motivated that Eq. 4.5 was used in those investigations.

There are several potential reasons behind deviations from no slip. Firstly, a non-zero slip length has been shown to be related to molecular wall–fluid interactions [138,139]. If the flow profile at the closest few nanometres to the surface is different from that far away from the surface, this in turn will affect the extrapolation from measurements made far away from the surface. Other system properties such as ionic strength [140], mobile interfaces [141], and surface roughness [142] can all affect the diffusivity-size relation. This puts limits on the accuracy of diffusivity-based nanoparticle sizing and the understanding of particle motion when at a nanometre distance to a surface. This reasoning motivated the work behind the method developed in Paper I, which was used to estimate the slip length of liposomes and extracellular vesicles (EVs).

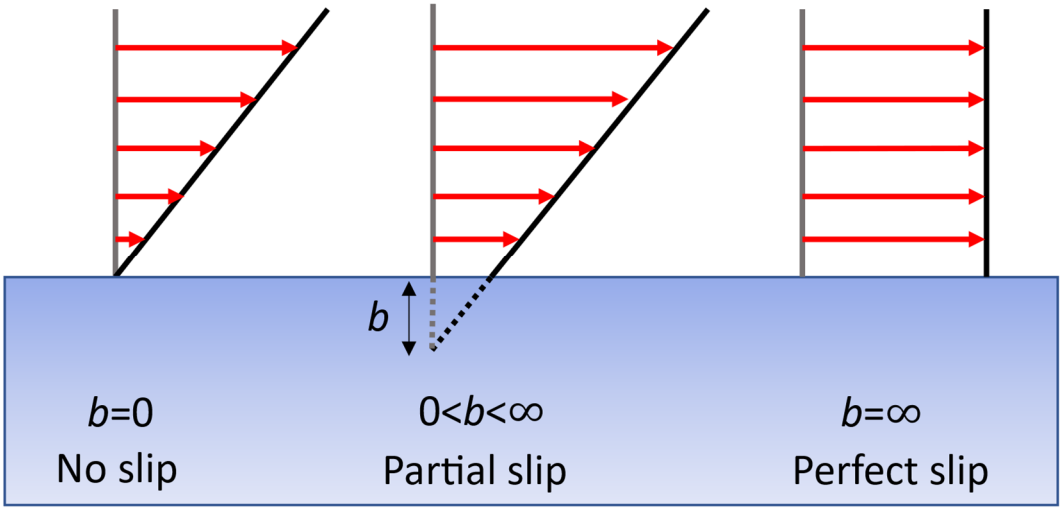

Figure 8 Schematic illustration of three common hydrodynamic boundary conditions. No slip: the velocity of the fluid parallel to the surface is zero at the transition between the fluid and the solid interface. Partial slip: the friction at the fluid-solid boundary is finite, causing the velocity of the fluid to behave as if the no-slip boundary condition still occurs but at an effective surface which is inside the solid material, where the distance from the outer material surface to effective surface within the material is referred to as the slip length b. Perfect slip: the special case when the slip length is infinite.

4.2 Confined particle diffusion

The Stokes-Einstein equation for relating diffusivity to particle size assumes that the particle is far away from any neighbouring surface. When a particle approaches a surface, its diffusivity-size relation gradually changes [33]. The equation describing the change in particle diffusivity when approaching a planar surface under the no-slip boundary condition was first derived by Hilding Faxén in the beginning of the 20th century [143,144]. Faxén's derivation is based on the method of reflections and subsequent publications have introduced various number of correction terms [33,137]. Using the 5th order correction, the particle diffusion parallel to a surface depends on the distance from the centre of the particle to the surface, h_0, as [126]:

$$D_{\mathrm{NP,int}} \approx D_\infty \left[1 - \frac{9}{16}\left(\frac{R_\mathrm{h}}{h_0}\right) + \frac{1}{8}\left(\frac{R_\mathrm{h}}{h_0}\right)^3 - \frac{45}{256}\left(\frac{R_\mathrm{h}}{h_0}\right)^4 - \frac{1}{16}\left(\frac{R_\mathrm{h}}{h_0}\right)^5\right], \qquad 4.7$$

where D_∞ is the diffusion coefficient for the particle in bulk. This equation predicts that the closer the particle is to the surface, the slower the diffusion becomes. However, since Eq. 4.7 is derived for the case when $R_\mathrm{h}/h_0 \ll 1$, its predictions become unreliable when $R_\mathrm{h}/h_0 \to 1$. In the close proximity limit, the particle motion is better described by a different set of equations derived for when $(1 - R_\mathrm{h}/h_0) \ll 1$ [145]. To interpolate between the regimes, Brenner derived an equation that is commonly referred to as the Brenner formula [33,146], in which the particle diffusion parallel to a surface is:

$$D_\mathrm{B} \approx D_\infty \left[1 - \frac{8}{15}\ln\left(1 - \frac{R_\mathrm{h}}{h_0}\right) + 0.029\frac{R_\mathrm{h}}{h_0} + 0.04973\left(\frac{R_\mathrm{h}}{h_0}\right)^2 - 0.1249\left(\frac{R_\mathrm{h}}{h_0}\right)^3\right]^{-1}. \qquad 4.8$$

Although Eq. 4.7 and Eq. 4.8 look significantly different from each other, their predictions are similar as long as $h/R_\mathrm{h} > 1.3$ (Figure 9) [145].

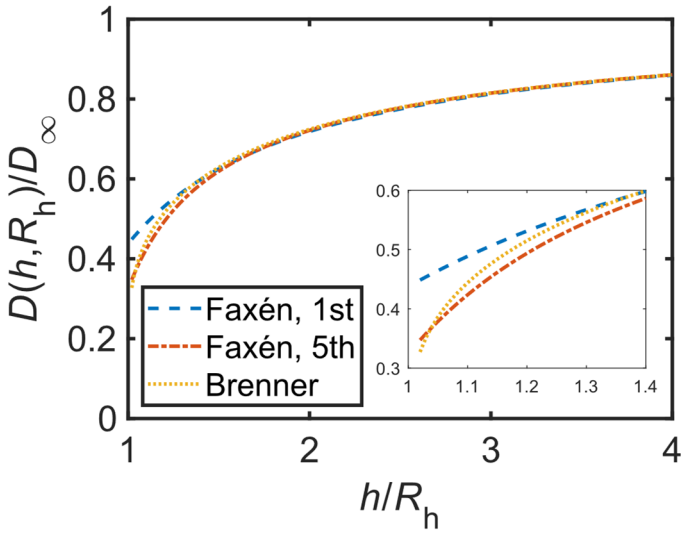

Figure 9 Diffusivity parallel to a planar surface for different particle-surface distances. Three different confined diffusion models (Faxén's first and fifth order corrections and the Brenner formula) are here shown, all assuming the no-slip boundary condition. The shorter the particle-surface distance the lower the diffusivty becomes. The inset highlights the difference for $h/R_\mathrm{h} < 1.4$. R_h is the hydrodynamic radius and h is the distance from the centre of the particle to the surface.

In the case of more general particle confinement, for example when a particle is in micro- and nanofluidic channels, the relation between diffusivity and particle size becomes different from that presented above. However, both for diffusion between two parallel surfaces [147] and for confinement in pores [148], the correction factors are known and looks similar to the presented equations for a single surface confinement. Thus, by using confinement corrections to the Stokes-Einstein relation, the diffusivity of suspended particles can still be related to the hydrodynamic radius.

The presented equations for confined diffusion assumes that the no-slip boundary condition applies. However, partial slip might occur at both the particle and the nearby surface, as reported for lipid bilayers using a surface force apparatus [149]. The resulting particle diffusion when deviation from no slip occurs at both the particle and nearly surfaces is not well established, especially when the distance from the particle to the surface is comparable to either of the two slip lengths [137]. In the limit where $h_0 \gg b$, the effect from the slip can be included in Eq. 4.7 by replacing h_0 with an effective distance $h_{\mathrm{ef}} \equiv h_0 + b$, which was the approximation used in Paper I.

4.2.1 Brownian motion of nanoparticles tethered to a lipid bilayer

In general, the diffusivity of a nanoparticle that is tethered to a mobile interface, such as a supported lipid bilayer (SLB, Section 2.1), depends on both the nanoparticle mobility μ_{NP} and the mobility of the tethers μ_{Tethers}. In the case of nanoparticles tethered to a lipid bilayer, μ_{NP} and μ_{Tethers} are related to two approximately independent origins of friction: between the surrounding fluid and the nanoparticle, and between the tethers and the SLB. Given that the frictions are inversely proportional to mobilities, the combined nanoparticle-tether mobility is

$$\mu^{-1}(R_{\mathrm{h}}) = \mu_{\mathrm{NP}}^{-1}(R_{\mathrm{h}}) + \mu_{\mathrm{Tethers}}^{-1}, \qquad 4.9$$

where the combined mobility is in turn related to the measured diffusion constant as $\mu = Dk_{\mathrm{B}}T$ [127]. Under the assumption of independent friction forces, only one of the two terms in Eq. 4.9 depends on particle size. Since the number of tethers can only obtain discrete values, it is possible to distinguish between particles linked with one, two or more tethers, enabling that the size dependence of the diffusivity can be quantified for each tether subpopulation. In Paper I, simultaneous size and diffusion constant measurements, achieved using two-dimensional flow nanometry (2DFN, Section 5.5), were used to obtain information about both terms of Eq. 4.9, which in turn were related to slip length and the diffusivity of the tethers.

4.3 Diffusion constant estimation from particle tracking

When using optical microscopy, the diffusion constant is most often quantified via particle tracking and estimation of the mean squared displacement [33]. However, the estimated particle position, $\hat{x}_{\mathrm{est}}(t)$, in a microscopy image is a combination between the true particle position, $x_{\mathrm{true}}(t)$, and the experimental/analytical position uncertainty $\zeta(t)$:

$$\hat{x}_{\text{est}}(t) = x_{\text{true}}(t) + \zeta(t). \quad 4.10$$

The position uncertainty depends on two different contributions: (i) how well the used position estimation algorithm can identify the centre of the particle, which varies depending on particle size and signal-to-noise ratio [150], and (ii) how much the particle moves during the exposure time. The position uncertainty affects the estimation of the mean squared displacement and the covariance between observed particle displacements as [130]*

$$\langle(\hat{x}_{n+1} - \hat{x}_n)^2\rangle = 2D\Delta t + 2(\sigma^2 - 2DK\Delta t), \quad 4.11$$

$$\langle(\hat{x}_{n+2} - \hat{x}_{n+1})(\hat{x}_{n+1} - \hat{x}_n)\rangle = -(\sigma^2 - 2DK\Delta t), \quad 4.12$$

$$\langle(\hat{x}_{n+1} - \hat{x}_n)(\hat{x}_{m+1} - \hat{x}_m)\rangle = 0 \text{ for } |m-n| > 1, \quad 4.13$$

where σ is the localisation uncertainty, the subscripts correspond to independent particle observations, Δt is the time between the observations, and K is the blur-factor describing the effect from particle motion during the exposure time. If the exposure time for the camera is the same as the time between frames, then $K = 1/6$ [151]. Thus, although σ^2 can be minimised using accurate localisation algorithms, the contribution from motion during the exposure time will remain and affect the relation between estimated mean squared displacement and particle diffusivity.

To accurately estimate particle diffusivity from a particle trace, it is therefore needed to correct for position uncertainty. From Eqs. 4.11-4.12 it follows that it is possible to correct for the bias terms on the single-particle level. However, the estimate is uncertain as the variance depends on the track length as [130]:

$$\text{var}(\Delta x_n \Delta x_m) = \frac{\alpha+4\alpha\beta+6\beta^2}{N-|n-m|} - \frac{2\beta^2}{(N-|n-m|)^2}, \quad 4.14$$

where $\alpha = 2D\Delta t$, $\beta = \sigma^2 - 2DK\Delta t$ and $(N+1)$ is the number of position observations of the same particle. If $\alpha \gg \beta$, for large N it follows from Eq. 4.14 that (standard deviation)/mean $\propto 1/\sqrt{N}$, which is the rule of thumb when it comes to diffusion estimation from particle traces. For this reason, it is beneficial to have long track lengths as well as performing the estimate of $(\sigma^2 - 2DK\Delta t)$ on the ensemble level. In Paper I, the contribution from position uncertainty was estimated on the ensemble level using a linear fit between $\langle(\Delta x_n)^2\rangle$ and $\langle\Delta x_n \Delta x_{n+1}\rangle$. That strategy was used since the particles all had a similar optical signal, making σ^2 approximately the same for the analysed particles. In Papers II-III, the effect from position uncertainty was assumed to be negligible due to a strong particle signal and short exposure time in the off-axis holography measurements compared to the time between frames. In Papers IV-V, the position uncertainty was corrected using a single value for each recorded video, both because the measured particles were close to the limit of detection and that the position uncertainties are slightly different between ordinary off-axis

* In Ref. [130] R is used instead of K. K is used here to avoid confusion with the hydrodynamic radius.

holography and twilight off-axis holography, requiring uncertainty correction to accurately compare the methods.

4.3.1 Using hydrodynamic radius for particle refractive index estimates

When using optical microscopy methods for particle characterisation, the hydrodynamic radius is often combined with the optical signal to estimate particle refractive index, as used in Papers II-V. However, since the hydrodynamic radius estimate has an uncertainty based on the track length (Eq. 4.14) and requires detailed information about the surrounding media, its use in estimates of particle refractive may introduce artefacts which is important to consider when interpreting the particle data.

First, uncertainty in the size estimation used to obtain particle refractive index affects the accuracy of the particle refractive index estimate. This goes beyond the use of hydrodynamic radius, where size and refractive index estimates using Mie theory has a similar correlation [100]. In the context of Papers II-V, the uncertainties in hydrodynamic radius and particle refractive index are anticorrelated since an underestimation of particle volume results in a subsequent overestimation of particle refractive index. This creates a non-physical correlation between particle size and refractive index, which often takes the shape similar to a banana in plots of the two particle parameters. For this reason, it is currently challenging to distinguish true size-refractive index correlations from that induced from data analysis. Long particle traces can be used to minimise the uncertainty in the hydrodynamic radius estimate, which is the case for high frame rate methods such as interferometric scattering (iSCAT) [43]. Another alternative is to use particle sizing approaches that do not require long track lengths, as used in Paper III where particle size was accurately estimated from optical scattering images using only five particle observations. However, these approaches only minimise the correlations, which shows the challenge in analysing potential continuous refractive index distributions in particle samples.

Second, estimates of the hydrodynamic radius in biological environments require substantial information about the surrounding media and the experimental system, where lack of such information increases the risk of misinterpreting the measured optical signal. For example, hydrodynamic boundary conditions, potential particle confinement, and media viscosity all affect the relation between measured mean squared displacement and particle size [33]. Since particle volume estimates scale with the hydrodynamic radius cubed, even small imprecisions when estimating particle size will have a large effect on the obtained particle refractive index. Therefore, the hydrodynamic radius can only be used in particle refractive index estimations in certain specific measurement conditions, such as when the particles are measured in known media in a microfluidic channel as in Papers II-V. To extend detailed optical particle characterisation to more complicated biological environments alternative particle sizing approaches are needed, which motivated the development of optical scattering-based particle sizing in Paper III and V.

5

Experimental methods

If it disagrees with experiment it is wrong.
In that simple statement is the key to science.
– Richard Feynman[*]

When measuring properties of macroscopic objects, such as the size of a football, it is typically assumed that the considered property can be measured without any major restrictions from the measurement tool itself. However, this reality changes when the size of the object starts to approach the nanoparticle size regime as it then becomes comparable to the resolution and/or the sensitivity of measurement methods. Detailed knowledge about the used measurement method is therefore required to minimise the risk of misinterpretations when relating the signal to particle properties.

In this chapter, the details of the developed experimental techniques are presented together with some of the complimentary techniques used to evaluate their performance. Since the ability to track the motion of particles is generic for optical microscopy methods, the focus in this chapter is the working principles of the different methods together with a motivation of their use and how they complement alternative methods.

5.1 Quantitative phase microscopy

The information in an ordinary image recorded by a camera is related to the amplitude of the incoming light. However, as described in Section 3.3, changes in light amplitude are primarily related to light extinction, which only gives partial material information about a particle. To obtain more detailed material information, one approach is therefore to measure both the scattering amplitude and the phase shift, which all are contained in the complex-valued optical field.

The first microscopy technique measuring the phase signal was developed in the middle of the 20th century by Frits Zernike, in which a phase-delay ring was used to increase the contrast of weakly optically interacting samples [105,153]. A vast number of phase

[*] Richard Feynman (1918-1988) received the Nobel prize in physics 1965 for his work related to quantum electrodynamics [152]. He is also famous for his lectures about physics.

microscopy methods have since been developed, all sharing some central features about how the phase information is obtained.

The central idea to recover phase information is to relate amplitude modulations of interfering optical fields to phase. If two or more optical fields are present at a camera, the recorded light intensity is:

$$I_{\mathrm{im}} = \left|\sum_n \vec{E}_n\right|^2 = \sum_n |\vec{E}_n|^2 + \sum_{n,m,n\neq m} \vec{E}_n \cdot \vec{E}_m^*, \qquad 5.1$$

where $\vec{E}_m^*$ is the complex conjugate of the optical field and subscripts correspond to different optical fields [22,51]. In the special case of two coherent optical fields where one of the fields is a plane wave, $\vec{E}_0 e^{-i(\vec{k}\cdot\vec{r})}$ (Section 3.1), Eq. 5.1 can be expressed as:

$$I_{\mathrm{im}} = \left|\vec{E}_0 e^{-i(\vec{k}\cdot\vec{r})} + \vec{E}_n(\vec{r})\right|^2 = \left|\vec{E}_0\right|^2 + \left|\vec{E}_n(\vec{r})\right|^2 + \vec{E}_0 e^{-i(\vec{k}\cdot\vec{r})} \cdot \vec{E}_n^*(\vec{r}) + \vec{E}_0^* e^{i(\vec{k}\cdot\vec{r})} \cdot \vec{E}_n(\vec{r}), \qquad 5.2$$

where $\left|\vec{k}\right| = 2\pi/\lambda$ and $\vec{r}$ is the 3D coordinate vector. The $\left|\vec{E}\right|^2$ terms of Eq. 5.2 are commonly referred to as intensity terms, as the same terms would be present if the fields were incoherent, whereas the two rightmost terms are called interferometric terms and are proportional to the optical field. The goal of phase microscopy techniques is to suppress the intensity terms such that the optical field is isolated.

Nowadays, there exist several strategies to suppress the intensity terms of Eq. 5.2 and quantify the full optical field. These strategies be divided into three classes using either: (i) several shifted images, (ii) spatially detailed interference patterns, and (iii) deep learning to recover the phase information from out-of-focus images [45,154–156].

In the case of using several shifted images, which includes I) phase-shifting [157,158], and II) the transport of intensity equation [154], a set of images with a known difference between them are used to obtain the optical field. For example, since a phase shift of one of the optical fields in Eq. 5.2 only influences the interferometric terms, a set of images with different relative phase shifts can be used to isolate the optical field [45]. The benefits of using several shifted images are that the spatial resolution is the same as in a single microscopy image and that light sources with a short coherence length* can be used. The disadvantage is that several images are required, which previously have limited the potential temporal resolution. Recent method developments have however demonstrated phase shifting at a kHz imaging speed [159]. The downside instead becomes the technical complexity of using active optical components.

The second approach, which is based on using spatially detailed interference patterns, can in turn be divided into I) interference with an external reference beam as in off-axis

* When two initially coherent optical fields travel different distances before recombined at a camera, the fields can become incoherent. The distance difference for which the fields become incoherent is referred to as the coherence length.

holography and II) interference with an internal reference beam as in quadriwave lateral shearing interferometry (QLSI). Off-axis holography is based on using an external reference beam which is slightly tilted with respect to the light that interacts with the sample (Figure 10). This method is presented in detail in Section 5.1.1, as it is the main experimental method used in Papers II-III, whereas a modified version of off-axis holography (twilight holography) was used in Papers IV-V (Section 5.1.2). QLSI is instead based on using a checkerboard phase grating just before the camera, which creates an interference pattern that enables extraction of the optical field [160]. In both cases the optical field is quantified using only a single image. However, using spatially detailed interference patterns comes with the drawback that the spatial resolution is slightly reduced compared to other approaches due the use of Fourier filters to isolate the optical field (Figure 11). In the case of off-axis holography, interference with a slightly tilted reference beam across the field of view requires that the light source has a coherence length of at least the wavelength multiplied with the square root of the number of camera pixels. This length is often around one millimetre and makes the images prone to coherence speckle noise [161]. Compared to off-axis holography, QLSI has the advantage of not requiring as coherent light, which reduces coherence-related noise [160]. The downside for QLSI is instead that system specific optical components are needed, which is not the case for off-axis holography.

The third approach use out-of-focus images and deep learning to recover the phase information [155,162]. In short, a deep-learning algorithm is trained to suppress the unwanted terms of Eq. 5.2 while also generating a focused optical field image, often using training data from multi-image phase reconstruction [162]. This removes the drawbacks of using several shifted images. The current drawbacks of this method are that the sample needs to be imaged significantly out of focus and that a representative training set is needed. However, since the method is continuously being developed, it remains to be seen to which extent these limitations will be possible to overcome.

5.1.1 Optical off-axis holographic microscopy

Off-axis holography is a microscopy technique that measures the complex-valued optical field. The technique was first developed in the 1960s by Emmett Leith to overcome some of the issues with Gabor holography* [163,164]. When using Gabor holography, it is difficult to separate the two interferometric terms (Eq. 5.2) and the technique is limited to samples that transmits most light without scattering [164]. To overcome these limitations, Leith introduced a tilted external reference beam to enable a mathematical procedure to separate the interferometric terms (Figure 10-Figure 11).

To motivate the use of a tilted external reference beam, we return to Eq. 5.2. If all the optical fields have the same polarisation, the reference beam is well approximated by a plane wave, and the camera plane is defined such that $z = 0$, the recorded image is:

* Holographic microscopy was initially developed for electron microscopy, but it was quickly realised that the same principles could be used in optical microscopy.

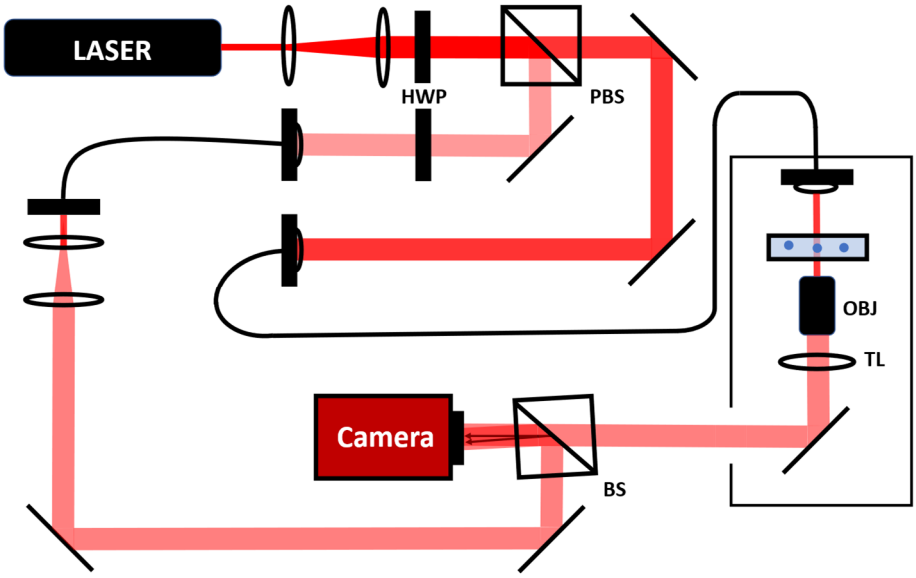

Figure 10 Schematic illustration of an off-axis holographic microscope. The laser beam is split into two different beams using a polarizing beam splitter (PBS), with one ligh beam passing through the sample while one does not. The two beams are then recombined at the camera with a slight angle with respect to each other. BS: beam splitter, TL: tube lens, OBJ: objective lens and HWP: half-wave plate.

$$I_{\mathrm{im}}(\mathrm{x},\mathrm{y}) = \left|\vec{E}_0\right|^2 + \left|\vec{E}_n(x,y)\right|^2 + |E_0|E^*_{\mathrm{obj}}(x,y)e^{-i(\Delta k_{\mathrm{x}}x+\Delta k_{\mathrm{y}}y+\Delta\Phi)} + |E_0|E_{\mathrm{obj}}(x,y)e^{i(\Delta k_{\mathrm{x}}x+\Delta k_{\mathrm{y}}y+\Delta\Phi)}, \quad 5.3$$

where $E_{\mathrm{obj}}(x,y)$ is the optical field that has interacted with the sample, $\Delta\Phi$ is a phase offset between the two beams and (Δk_{x},Δk_{y}) describe the angle between the external reference beam and the sample beam. At this point, it is important to recall the relation $\boldsymbol{\mathcal{F}}(f(x)e^{ik_{\mathrm{x}}x}) = \hat{f}(k-k_{\mathrm{x}})$, where $\hat{f}(k) = \boldsymbol{\mathcal{F}}(f(x))$ and $\boldsymbol{\mathcal{F}}$ is the Fourier transform operator [88]. Specifically, multiplication with $\exp\left(-i\left(k_{\mathrm{x}}x+k_{\mathrm{y}}y\right)\right)$ becomes an offset in the spatial frequency space. Thus, the interferometric terms and the intensity terms can be separated from each other during the image post processing.

An example of the image analysis used to obtain the optical field from a recorded image is shown in Figure 11. The central peak of the Fourier transformed image corresponds to the intensity terms and the off-centre peaks correspond to the interferometric terms. One of the interferometric terms can be isolated by first centring the corresponding Fourier peak, which is done by multiplying the microscopy image with $\exp\left(-i\left(k_{\mathrm{x}}x+k_{\mathrm{y}}y\right)\right)$ before the initial Fourier transform, and then applying a Fourier filter. The inverse Fourier transform is thereafter used to obtain the optical field (Figure 11) [45]. The obtained field is then normalised and the static background is subtracted, after which the scattering pattern of particles become clearly visible.

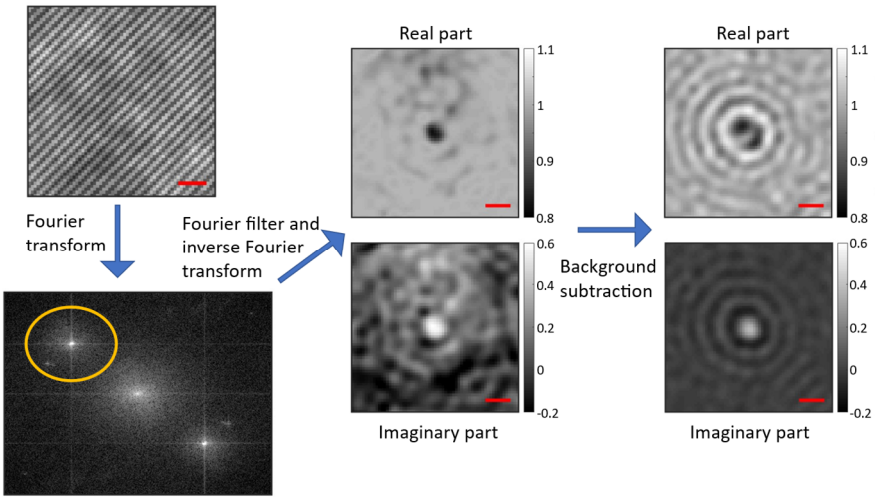

Figure 11 Illustration of the initial data processing steps of the off-axis holography. The recorded image at the camera is Fourier filtered such that the optical field is obtained. The optical field is then normalised such that the plane wave background is equal to 1. The stationary background signal is thereafter subtracted. All images with a scalebar (1 µm) correspond to the same region in the sample.

Once the optical field is obtained, the signal can be related to particle properties (Section 3.3). Furthermore, by utilising the propagation algorithm in Sections 3.1, the optical field can be repropagated and analysed at any arbitrary depth position, enabling analysis of particles throughout the sample volume. For these reasons, off-axis holography has been extensively used in various cell studies [45]. These aspects of off-axis holography were all utilised in Papers II-V to enable quantitative particle characterisation and tracking throughout the volume of a microfluidic channel.

5.1.2 Twilight off-axis holography

When detecting small particles using interferometric microscopy, the signal-to-background ratio is critical. If the background signal is too high, it will saturate the image. However, if no background is present, it is not possible to quantify the relative signal shift induced by the particle compared to the background.

The approach in Papers IV-V to improve the signal-to-background ratio of off-axis holography was to use of a low frequency attenuation filter (LFAF) [165], which consists of a semi-transparent optical filter placed in the back-focal plane of the objective (or a conjugate to the back-focal plane). The purpose of the LFAF is to selectively attenuate the unscattered light. This is achieved by utilising the properties of 4f lens systems [86], which enables access to the Fourier transform of the input image (Figure 12). Specifically, since the Fourier transformation of a plane wave is approximately a point and a point source is Fourier transformed to a plane wave, it is possible to position the LFAF such that it mainly attenuates the background signal. Using an LFAF therefore enables that a more intense illumination can be used compared to when the LFAF is absent without increasing the background signal, which increases the signal-to-background ratio and the lower detection limit.

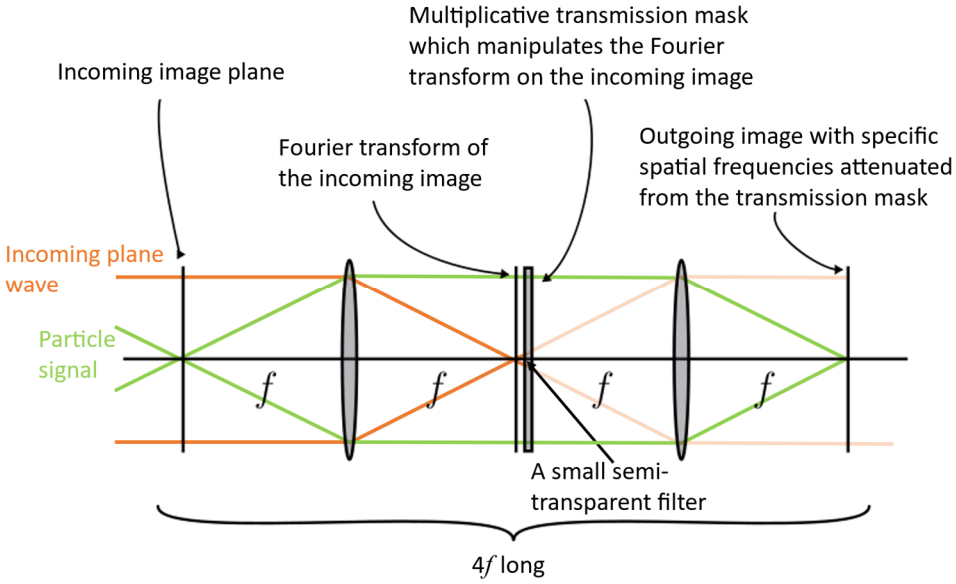

Figure 12 Schematic image showing the properties of a 4f (focal length) system in the case of a low frequency attenuation filter (LFAF). The incoming signal from the left is Fourier transformed using the property of the first lens. The LFAF is positioned in the Fourier plane such that it mainly attenuates the incoming plane wave and not the particle signal. The second lens transforms the signal to an image again. The particle signal is in orange and the plane wave background is in green to make it easier to distinguish the two signals. Modified from Wikimedia [166] under CC0 1.0 licence.

Twilight off-axis holography is off-axis holography augmented using an LFAF (Figure 13). The similarity with ordinary off-axis holography enables that the image can be processed using the same algorithms. The main difference is that the relation between the measured particle signal and particle properties changes. Specifically, the measured particle signal relative to the background signal E_0 becomes

$$E_{\mathrm{im}} = aE_0 + E_{\mathrm{p}} = aE_0\left(1 + \frac{E_{\mathrm{p}}}{aE_0}\right) \quad , \qquad 5.4$$

where a describes the attenuation and the phase shift of the LFAF and $|a| < 1$. Since a in general is a complex number, it affects the relation between the measured optical field and particle properties due to the background normalisation. In previous work using an LFAF, the full extent of how the LFAF affects the signal has not been critical as the main interest has been the signal amplitude and not how the LFAF affects the relative phase shift between the particles and the background [35,167,168]. To maintain the ability to relate the optical signal to particle properties, the effect of the LFAF was in Papers IV-V quantified by measuring the optical field from a particle sample both with and without an LFAF present, where the difference in particle signal was attributed to a. With the properties of the LFAF known, the measured particle signal can be processed such that it can be related to particle properties in the same way as for ordinary off-axis holography.

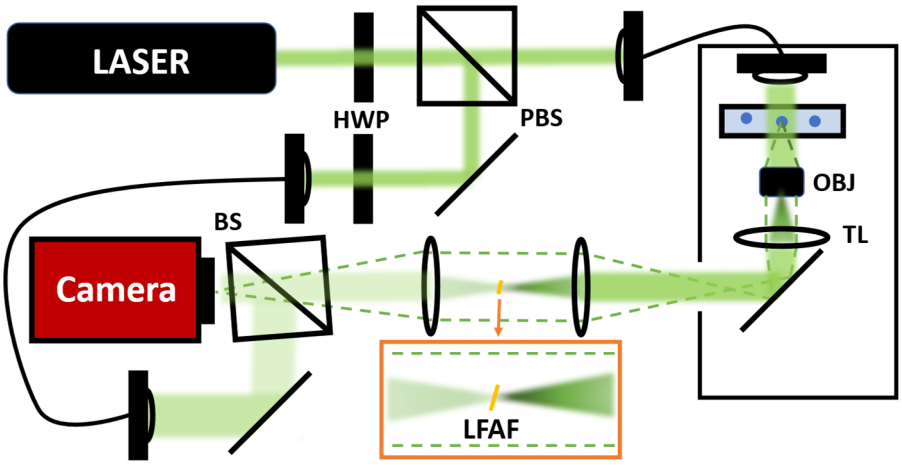

Figure 13 Schematic illustration of a twilight off-axis holographic microscope. The laser beam is split into two beams by the polarizing beam splitter (PBS): one beam goes through the sample, while the other beam acts as a reference. The low frequency attenuation filter (LFAF) reduces the amplitude of the unscattered light of the sample beam while having a negligible effect on the particle signal, as highlighted in the zoomed-in inset. The LFAF is slightly tilted to direct reflected light away from the optical axis. BS: beam splitter, TL: tube lens, OBJ: objective lens and HWP: half-wave plate.

5.1.3 Tracking of subwavelength-sized particles using phase microscopy

Particle tracking consists of two different challenges: detection and linking of subsequent detections. The starting point for particle tracking is detection. The particle detection in Papers I-III is based on using a global signal threshold, whereas in Papers IV-V the N strongest image detections were considered as potential particle candidates, as it was assumed that true particle traces could be differentiated from noise traces based on track length and flow direction.

For each potential particle candidate, the subpixel position is typically estimated to improve the accuracy when relating the measurement to particle properties (see for example Section 4.3). In optical field imaging, as in the case of off-axis holography, the optical field image can be re-propagated once captured (Sections 3.1). This allows each image of every particle to be transformed such that the particle is in focus, enabling particle position determination in 3D. However, this requires the use of an automated focus criterion that is generic enough to capture all the particles of interest.

There are numerous focus criteria for different types of samples, where each criterion is based on different particle features [169,170]. In Papers II-V, the used focus criterion is based on optical features of point-like particles and self-similarity along each trace. From propagation of angular spectrum (PAS, Section 3.1), the Fourier image of a point-like particle is flat when in focus and has a parabolic phase profile when out of focus. For this reason, a generic focus criterion for point-like particles is to minimise the standard deviation of its Fourier image, which was introduced in Paper II. Once having an initial focused particle image, subsequent particle images can be focused by minimising the difference compared to the first particle image. These two approaches were used in Papers II-V to track the depth position of the particles as these focus criteria are computationally efficient and insensitive to the presence of an LFAF.

The in-plane position can also be determined using several different metrics [150]. In Paper I, the position determination was done using Gaussian fitting, while in Papers II-V the radial symmetry center was used [171]. Gaussian fitting works well for point-like particles in focus, as for particles tethered to a supported lipid bilayer (SLB), which motivated its use in Paper I. The radial symmetry center method estimates the position of radial symmetric features in images, which makes it more versatile than using Gaussian fitting. Since the detected particles in Papers II-V had different sizes and were tracked in 3D, it motivated the use of the radial symmetry center method.

To link subsequent observations, each particle observation in the papers of this thesis were associated with a distance metric to particle detections in previous frames, where the observations were joined into particle traces by minimising the sum of this metric using the Hungarian algorithm [172]. In papers II-V, to link the particle observations correctly even at high flow speeds, the positions from the particle traces in the previous frame were extrapolated using the mean displacement before calculating the distance metric. Together with an upper distance cut-off during the linking of particle observations, this forms the basis of the particle tracking used in the papers of this thesis.

5.2 Interferometric scattering microscopy

An alternative strategy to the use of an LFAF to improve the signal-to-background ratio during interferometric imaging of nanoparticles is to measure the backscattered light (Figure 14). Since the light scattering from nanoparticles is approximately isotropic whereas only a small fraction of the incoming illumination is reflected at the glass-water interface, the signal-to-background ratio is higher in the backscattering direction than in the forward scattering direction. This measurement configuration goes under the name interferometric scattering (iSCAT) microscopy and was developed approximately 20 years ago for the purpose of detecting even smaller nanoparticles than what was possible at the time [173,174]. Nowadays, iSCAT is mostly used as a surface technique to measure the optical mass of biomolecules [35] or to track surface-bound particles/molecules [175,176]. The last few years iSCAT has also been used to characterise suspended particles [43,177], which is how iSCAT was used in Paper V. However, the motivation behind the use of iSCAT in Paper V is not based around its detection limit, but rather that the measured particle signal from iSCAT can be combined with simultaneous twilight off-axis holography measurements to estimate particle size directly from the optical signals (Section 5.3).

Characterisation of suspended particles using iSCAT is slightly different from particles on a surface. First, the interference between the optical fields from the particle and the background depends on their relative phase, which changes with the particle's depth position [178]. iSCAT images of suspended particles therefore changes between subsequent particle observations, making it difficult to estimate the particle signal. To handle this challenge, in Paper V the iSCAT images were transformed using a convolutional neural network (Section 5.4) trained to generate focused images in which the particle signal corresponds to the amplitude of its backscattered optical field.

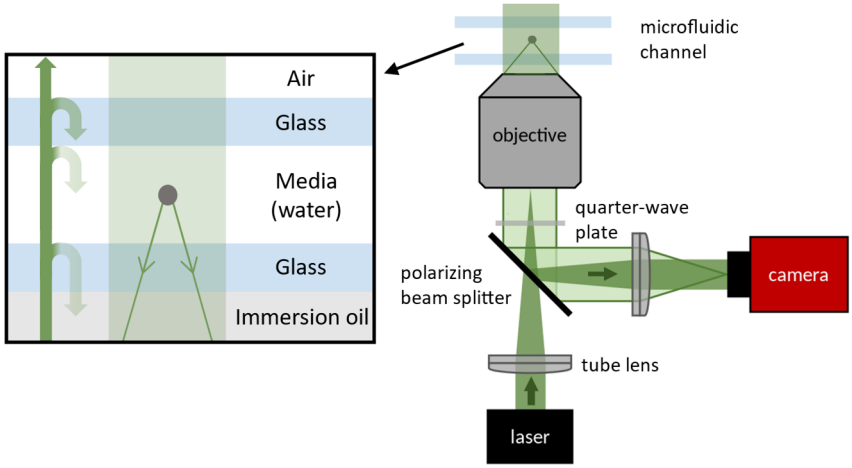

Figure 14 Schematic image of a widefield interferometric scattering (iSCAT) setup when combined with a microfluidic chip. Linear polarised light from a laser is focused in the back focal plane of the objective. Backscattered light from the particle and all the material interfaces in the sample are collected by the objective, where the double passage through the quarter-wave plate changes the polarisation direction such that the backscattered light is directed towards the camera. The image is adapted from Wikimedia under CC BY-SA 4.0 licence [179].

Second, the suspended particles in Paper V were measured under flow in a microfluidic channel, where all the interfaces of the microfluidic channel contribute to several interface reflections (Figure 14). Specifically, there are reflections from the two glass-media interfaces and glass-air interface. When measuring surface-bound particles using iSCAT, these reflections are avoided by either using an open droplet instead of microfluidics [174] or by scanning a focused light beam across the field of view instead of widefield illumination [23]. In Paper V, the challenges of using microfluidics were solved using two different solutions. By having a slight angle between the incoming illumination and the optical axis of the microscope* the glass-air reflection is separated from the other reflections. This separation enables that an optical filter can be used to block that specific reflection from reaching the camera. The two media-glass reflections were handled by utilising that the height in the used microfluidic chip varied slightly between different regions in the channel. This in turn affects the relative phase between the two reflections, which results in constructive/destructive interference (Figure 3) depending on chosen imaging position in the channel. In Paper V, the imaging position was chosen such that the two reflections interfered constructively.

5.3 Dual-angle interferometric scattering microscopy

One major limitation of particle characterisation using optical microscopy is that particle size is most often estimated using the diffusivity-size relation, which limits investigations into particle size to suspended particles in a media of known viscosity (Section 4). One alternative optical scattering-based particle sizing approach is to relate the light scattering at different angles to particle size (Figure 15a). Using Rayleigh-

* The optical axis of a microscope is an imaginary line along which there is some degree of rotational symmetry. Optical components such as lenses are in general positioned such that their middle point is on the optical axis unless the optical system is intentionally misaligned.

Debye-Gans theory, which is valid for small weakly optically interacting particles (Section 3.3.1), the ratio of measured particle signal at two different scattering angles can be related to the optical from factor (Section 3.3) [48,95]. The optical form factor can in turn be related to particle size with no dependence on particle refractive index. Such particle sizing is used in multi-angle light scattering (MALS) [48,95] and nanoparticle flow cytometry [102], which are methods that measure the ensemble signal or single-particle snapshot information, respectively. To combine a similar particle characterisation approach with optical microscopy, dual-angle interferometric scattering microscopy (DAISY) was developed in Paper V.

Since Rayleigh-Debye-Gans theory is only valid for particles with a minor refractive index difference to the surrounding media (Section 3.3), relying on Rayleigh-Debye-Gans theory when relating the optical signal to particle properties limits the particles that can be accurately characterised. For spherical particles, Mie theory can be used to describe the optical particle signal (Section 3.3.2). When calculating the scattering ratio of different particle sizes and refractive indices (Figure 15a), the scattering ratio is uniquely related to particle size when the radius is smaller than 170 nm, where the precision of the size estimate depends on the available particle refractive index information. Specifically, the uncertainty is within a few nanometres when considering a refractive index range of 1.34-1.60, which cover most biological nanoparticles [15].

The working principle of DAISY is to use the information in forward and backward scattering to simultaneously estimate both particle size and polarizability of individual particles. The DAISY radius, which is the size estimate of DAISY, is defined as the smallest radius of a homogeneous sphere suspended in water having the same backscattering-forward scattering ratio and polarizability, where the polarizability information improves the accuracy of the size estimate. The forward scattering image is measured using twilight holography, which signal can be related to polarizability (Section 3.3), and the backscattering image is measured using iSCAT (Figure 15b).

The measured scattering signal ratio in DAISY is related to particle size by introducing the generalised optical form factor $\widetilde{f_{\mathrm{b}}}$. The generalised optical form factor is based on taking the scattering ratio from Mie calculations, which makes it similar to the ordinary optical form factor and is used to generalise the applicability of DAISY beyond small weakly optically interacting particles. The particle signal ratio measured in iSCAT and twilight holography is related to the generalised optical form factor $\widetilde{f_{\mathrm{b}}}$ as

$$\frac{\mathrm{iSCAT}}{|\mathrm{twilight}|} \propto \widetilde{f_{\mathrm{b}}}(q_{\mathrm{i}}; \rho, \alpha), \qquad 5.5$$

where q_{b} is the average q value for the backscattering direction (Section 3.3.1), ρ encodes the spatial distribution of mass within the particle, and α is the polarizability. The generalised optical form factor can in turn be related to particle size. In Paper V. it is shown that the DAISY radius estimate is insensitive to the precise value of the refractive index of the surrounding media (size uncertainty within a few percent for biological environments as the refractive index is often only of a few percent higher

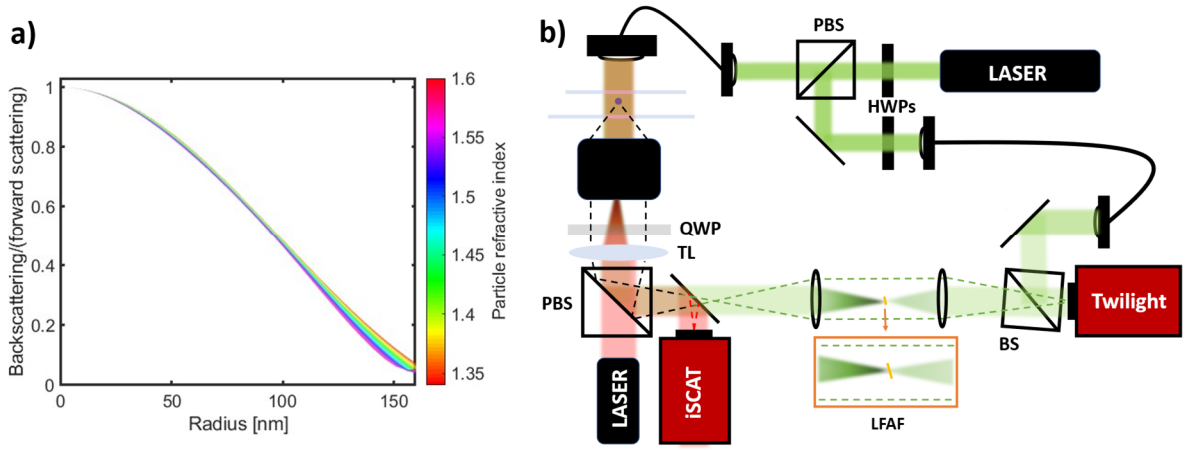

Figure 15 The working principle of dual-angle interferometric scattering microscopy (DAISY) and how the optical signal ratio is related to particle size. (a) Mie calculations of the ratio between the backscattering and forward scattering as a function of particle size for particles in water with a refractive index of 1.34-1.60. (b) The DAISY setup, which corresponds to one interferometric scattering (iSCAT) part and one twilight off-axis holography part. LFAF: low frequency attenuation filter, BS: beam splitter, PBS: polarising BS, TL: tube lens, QWP: quarter wave plate, and HWP: half-wave plate.

than that of water [180]). Thus, DAISY enables surrounding media intensive particle sizing using optical microscopy, which combined with the polarizability information also enables simultaneous estimation of the refractive index difference between the particle and the surrounding media.

Since the optical form factor is different for different particle shapes (Section 3.3.1), the optical scattering ratio is also dependent on the particles internal mass distribution. Using that the hydrodynamic radius relates to the outer radius of the particle, the relative value of the DAISY radius and the hydrodynamic radius relates to the particle shape of individual particles. This property of DAISY was used in Paper V to distinguish solid spheres from aggregates.

5.4 Image analysis of microscopy data using deep learning

Image analysis is typically based on using a fixed set of mathematical operations, such as convolutions and thresholds, combined with intuition about the experimental system in question [181]. Despite the historical success of this approach, the explored space of potential solutions* of a human is limited, where the obtained solution may not be optimal and depends significantly on the knowledge of the user. One solution to this limitation is to use deep learning to find a solution to the task at hand.

In essence, image analysis using deep learning is based on setting up a space of image processing operations, such as thresholds and convolution, where a computer explores different parameter combinations of the image processing operations given a certain set of rules [181]. There exist several different classes of deep learning, both regarding the

* The phrasing "space of potential solutions" comes from viewing the task as a multi-dimensional optimisation problem, where each free parameter, such as a signal threshold, is a separate dimension in the space of potential solutions.

mathematical operations the algorithm performs and how the end-result is obtained. In the context of image analysis of microscopy data, convolutional layers are commonly used as they are inherently translation-invariant and contain relatively few parameters to be optimised compared to fully connected layers [182]. The individual layers are combined into a network structure, where the structure of the network depends on the considered application. For example, for image-to-image translation the so-called U-Net structure has successfully been applied to holography data to achieve phase recovery, denoising, and virtual staining [155,183], where U-Net's ability of analysing microscopy images motivated its employment in Paper V. Another example is convolutional neural networks (CNN) combined with dense neural networks, which has been used to estimate size and refractive index from particle scattering patterns [100] and inspired the employment of a similar network structure in Paper III.

There are both advantages and disadvantages to using deep learning in image analysis. The main disadvantage is that representative training data is needed, which can be challenging to obtain. Moreover, for images with a high signal-to-noise ratio and distinct features of interest, established image analysis algorithms often performs similarly to deep-learning algorithms [184]. For this reason, it is not certain that the time investment in training a network will improve the performance.

The advantages of using deep learning in image analysis include for example improved particle detection and localisation accuracy at low signal-to-noise ratios [124,184] as well as new analysis possibilities, such as recovering the phase information from a single out-of-focus image [155] and virtual staining [183]. Moreover, during the past few years there have been significant effort to minimise the disadvantages of using deep learning. For example, in some applications it is now possible to train a network using a single experimental image [124], which significantly reduces the complexity of training a network. Moreover, there are now several open-source software packages available that aid in this step of the analysis. This was utilised in Papers III and V where the networks were trained using the Python library DeepTrack 2.0 [182].

5.5 Two-dimensional flow nanometry

When quantifying the diffusion constant of individual particles, long track lengths are needed to reduce the statistical uncertainty (Section 4.3). However, if the particles are free to move unrestrictedly in 3D, they will eventually move outside the imaging region, which consequently limits the experimentally obtainable track lengths. To overcome this limitation, one solution is to restrict the motion of the particle by using nano- or microfluidic designs [185,186]. Another approach is to molecularly link the particles to a laterally fluid SLB (Section 2.1), as illustrated in Figure 16, which restricts the particle motion to two dimensions [187]. Although long track lengths can readily be obtained using any of these approaches, the particle mobility is affected by the confinement (Section 4.2). Furthermore, when a particle is molecularly linked to an SLB, the mobility of the particle-tether complex depends also on the mobility of the linker (Section 4.2.1) [59,188]. Thus, when using any of these approaches, the ordinary

Stokes-Einstein equation cannot be used to relate diffusivity to particle size without first introducing corrections for the particular system under investigation [126].

In the case of nanoparticles tethered to an SLB, one strategy to avoid the added complexity when relating diffusivity to particle size is to introduce a shear flow and use the ratio between the flow-induced particle velocity and its diffusivity [59]. Implied by the Einstein–Smoluchowski relation [14], which relates diffusivity with particle mobility, the ratio between the flow-induced particle velocity, v, and the diffusion constant, $D_{\mathrm{th-NP}}$, relates to the hydrodynamic force as [59]

$$F = k_{\mathrm{B}}T\frac{v}{D_{\mathrm{th-NP}}}. \qquad 5.6$$

Assuming spherical particles, F is related to particle size, R_{FN}, as [59]

$$F = k_{\mathrm{B}}T\frac{v}{D_{\mathrm{th-NP}}} \approx A\eta u_0 R_{\mathrm{FN}}\left(R_{\mathrm{FN}} + \tilde{\lambda}\right), \qquad 5.7$$

where u_0 is the flow rate of the surrounding fluid, η the dynamic viscosity of the surrounding fluid, while A and $\tilde{\lambda}$ are calibration parameters which depend on the experimental geometry and hydrodynamic boundary conditions. In other words, since both the flow-induced particle velocity and the diffusion constant depend on the mobility of the tethered particle, their ratio cancels the effect from the unknown mobility. This approach to measure particle size is called two-dimensional flow nanometry (2DFN) and is the main particle characterisation approach in Paper I.

Since 2DFN offers both size and diffusivity information of particles that are only a few nanometres away from a planar interface, the diffusivity-size relation is sensitive to the hydrodynamic boundary conditions of the particles and the SLB (Section 4.2). This was used in Paper I to obtain information about the slip length for lipid bilayers and extracellular vesicles (EVs), where the mobility contributions of the particle and that of the tethers were separated during the data analysis.

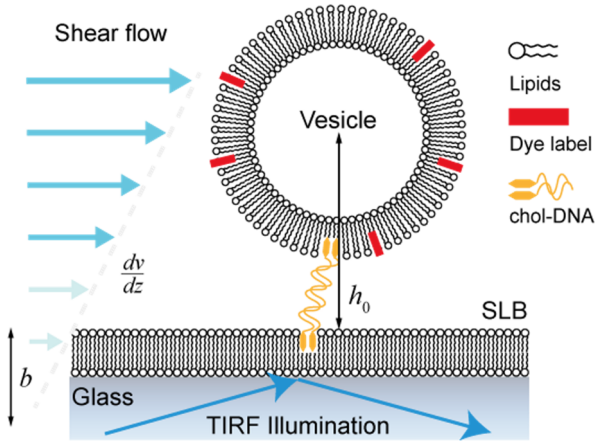

Figure 16 Schematic of a two-dimensional flow nanometry (2DFN) measurement. Particles (here a lipid vesicle) are linked to a supported lipid bilayer (SLB) using molecular tethers, here consisting of a cholesterol-DNA tether. A shear-flow is applied such that the particle has a non-zero drift velocity. The particles are typically imaged using total internal reflection fluorescence (TIRF). b indicates the potential slip length of the SLB and h_0 is the distance from the centre of the particle to the SLB.

5.5.1 Total internal reflection fluorescence microscopy

Total internal reflection is an optical phenomenon which occurs when light travels from a medium with a higher refractive index to one with a lower refractive index* and the angle relative to the normal direction of the surface is larger than a critical value determined by the ratio of the two refractive indices [51]. When this happens, there is no direction in the second medium in which constructive optical interference in the far field can occur. Instead, all light is reflected at the surface. Although the far field is zero, there is still a non-zero optical near field close the interface in the low refractive index medium, which often is called the evanescent field. This evanescent field can excite fluorophores near the surface, which forms the basis of total internal reflection fluorescence (TIRF) microscopy.

The intensity of the evanescent field decays exponentially, $I = I_0 \mathrm{e}^{-z/\delta}$, with the characteristic length δ,

$$\delta^{-1} = \frac{4\pi}{\lambda}\sqrt{(n_1 \sin\theta)^2 - n_2^2}, \qquad 5.8$$

where n_1 is the refractive index of the original medium, n_2 is the refractive index of second medium and θ is the relative angle between the incoming ray of light and the normal of the surface [22]. TIRF is commonly used when analysing particles attached to an SLB as it suppresses the potential background signal from particles in bulk [189–191], a feature used in Paper I.

5.6 Transmission electron microscopy

The spatial resolution of optical microscopy methods is limited by the wavelength of the used measurement beam (Section 3.2). To obtain structural information beyond the spatial resolution of ordinary optical microscopy, one approach is therefore to illuminate the sample with a beam having a shorter wavelength than visible light. Since all particles have a de Broglie wavelength, electrons that are accelerated in a potential of hundreds of kilovolts have a wavelength shorter than 0.01 nanometres [1]. Combined with that electron beams can be generated and controlled using an electron source and electromagnetic fields [1], electron microscopy is commonly used to measure nanomaterials with sub-nanometre spatial resolution [192,193].

In both Paper III and IV transmission electron microscopy (TEM) was used for complementary size characterisation of the measured particle samples. A TEM works similarly to an optical transmission microscope: there is a signal source which emits an illumination beam that is directed towards the sample using several lenses, where lenses after the sample are used to create an image of the sample at a camera (Figure 17). The main differences are that in a TEM the lenses consist of electromagnetic coils and the illumination consist of charged electrons in an electron beam [1].

* In optical microscopy, the high refractive index material is commonly glass, and the low refractive index material is commonly water (Figure 16).

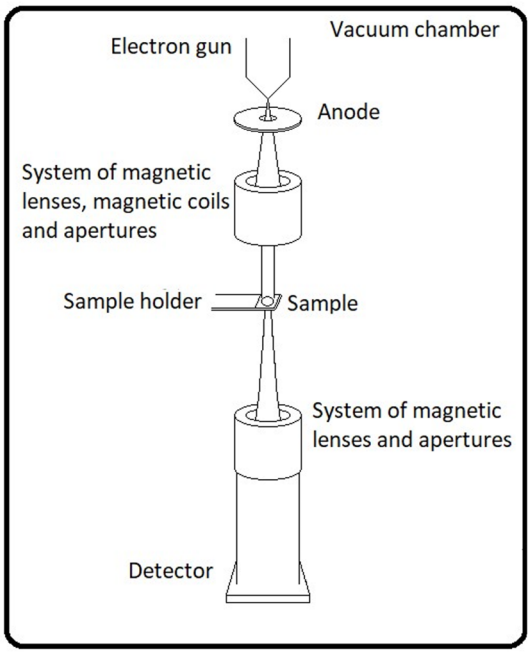

Figure 17 Schematics of a transmission electron microscope (TEM). The electron beam is generated in the top of the microscope and is then accelerated and directed towards the sample by magnetic/electrostatic lenses/coils. The electrons that penetrate the sample are collected and directed towards a detector. All the components in the microscope are under high vacuum.

A crucial difference between optical microscopy and electron microscopy is the measurement conditions. Specifically, optical microscopy can used at physiological conditions whereas electron microscopy typically operates under high vacuum [1]. Since TEMs operates under high vacuum, sample preparation is important to maintain the structure of the particles of interest. Solid dielectric particles such as silica and polystyrene, as used in Paper III, are stable in vacuum. In Paper III, the TEM sample preparations therefore consisted of placing a small droplet on a TEM grid, and after a few minutes the excess liquid was removed by slightly touching the droplet with a tissue paper. Such sample preparation cannot be used for biological nanoparticles since the drying may cause imaging artefacts [193]. In Paper IV cryoTEM was therefore used, where a small droplet containing the solution is frozen in liquid ethane such that the sample vitrifies [193], and the imaging was thereafter performed at -178 ^{o}C.

5.7 Comparison between label-free optical methods for characterisation of subwavelength-sized particles

As outlined in Section 3.3, the label-free particle signal acquired from different optical scattering methods contains similar particle information in the nano-submicron regime. Several different optical characterisation techniques can therefore often be used to address the same question. However, there are some key distinctions between different methods that become critical in multiparametric particle characterisation, where the main differences of some selected techniques are summarised in Table 1. In that table and the following subsections, five specific experimental aspects will be considered to separate the quantitative capabilities of different optical methods.

Table 1 Summary of strengths and weaknesses for different particle characterisation methods using optical scattering, where the details of the comparison are presented in Sections 5.7.1-5.7.5. DLS: dynamic light scattering.

	Darkfield (solution)	Interferometric imaging (solution)	Complex-valued optical field (solution)	Surface methods	Non-imaging methods
Main strength	Detection limit around 5 nm	Can detect single proteins (≳66 kDa)	Material sensitive signal that can be related to particle mass	Particle dynamics and surface interactions	Measurements with high particle statistics
Main limitation	Limited material sensitivity	Limited material sensitivity	Particle detection limit slightly below 100 nm in diameter	Limited throughput	Limited ability of analysing heterogenous samples
Shape sensitive?	Most often yes	Yes	No	Yes	Yes
Hydrodynamic radius?	Yes	Yes	Yes	Most often no	Yes (DLS)

5.7.1 Particles in suspension or bound to a surface

Although Papers II-V involve measuring the scattering signal from suspended particles, there are numerous scattering-based microscopy methods that rely on binding the particles to a surface. This includes for example evanescent field scattering [194–196], iSCAT [197], and multi-imaging phase methods [109]. For surface-bound particles a similar signal-polarizability relation as for suspended particles can be used to characterise the particles, with the difference being that the scattering directivity is affected [198].

The main benefit of immobilising particles on a surface is that signal of hundreds of individual particles can simultaneously be measured on the single-particle level during environmental changes [195], which cannot easily be done for freely suspended particles. The drawback with surface immobilisation is that it is challenging to relate the signal to multiparametric particle properties such as size and refractive index due to that the diffusivity-size relation cannot be used. In some cases, 2DFN or multiple refractive index media can used to obtain size information [199], but then the throughput becomes limited compared to when measuring under flow. In Paper I, the close proximity between the particles and the surface was used to enhance the effect from potential partial slip, which highlights that the gained information from the surface tethering was in that specific case worth the lowered throughput. Thus, measuring surface-bound particles are advantageous for detailed investigations of particles over time or particle-surface interactions, while methods that use suspended particles are advantageous for high-throughput characterisation in terms of size and refractive index. Since the goal of Paper II-V was to establish a generic particle characterisation methodology, the focus became to characterise freely suspended particles.

5.7.2 Measurement geometry

The angle between the incoming light and measured light-scattering direction influences how the optical particle signal scales with size, which can be described by the optical form factor (Section 3.3.1). In particular, the relation between particle signal and size is only single valued when using transmission methods. Thus, when using non-transmission methods, particle shape and size information are needed to estimate the dry mass if the particle radius larger than a few tens of nanometres (Section 3.3.1). However, non-transmission methods are required to observe a difference in the measured signal of a nanoparticle based on its structure, as for example used in Ref. [30].

The optimal choice of measurement geometry is therefore related to the particle information of interest. For quantification of the dry mass when the particle shape is unknown, as in Papers II-IV, a transmission measurement geometry is advantageous. For particle shape measurements, as in Paper V, non-transmission methods are preferred. In Paper V specifically, the combination of hydrodynamic radius and optical scattering in the forward and backward directions were used to estimate the mass distribution within individual particles (Section 5.3). However, the state-of-the-art detection limits are currently also different for different measurement geometries, which is further discussed in Section 5.7.5.

5.7.3 Optical field or scattering intensity

Optical field or quantitative phase measurements give information about the complex-valued particle polarizability, which contains more particle material information than the scattering intensity alone (Section 3.3). For suspensions of nanoparticles made of a single material, the scattering intensity is sufficient to estimate particle refractive index. The difference in quantitative particle information between scattering intensity and the optical field becomes crucial when the sample contains several different types of particle materials. For example, when relating scattering intensity to refractive index, the optical intensity gives only information about the absolute value of the polarizability, which is insufficient to distinguish particles such as metallic nanoparticles, dielectric particles, and nanobubbles. The main drawbacks with optical field measurements are that it requires extensive image analysis and that its detection limit is much higher than for methods that only measures scattering intensity (Section 5.7.5).

In Papers II and IV the measured particles involved mixtures of bubbles/solid particles and dielectric/metallic particles, respectively. For this reason, optical field measurements were chosen as the main experimental method as the scattering amplitude would not have enabled the required material sensitivity.

5.7.4 Imaging or non-imaging characterisation methods

The spatial resolution in microscopy enables the same particle to be tracked over time, which can for example be used to estimate particle size via the Stokes-Einstein relation (Section 4). However, it is possible to optically characterise particles without relying on particle tracking. For example, when using nanoparticle flow cytometry, it is possible to simultaneously obtain snapshot information regarding size and refractive index by measuring the forward and side scattered light [102]. Moreover, dynamic light scattering (DLS) can be used to estimate ensemble particle size from the time-correlated scattering intensity [27]. The benefits of non-imaging methods are the increased particle throughput and that no image analysis is needed. The drawbacks with non-imaging methods are that they often require limited sample heterogeneity, only measure the optical scattering intensity, and that the single-particle dynamics cannot be accessed. Thus, to measure single-particle dynamics or the complex-valued polarizability, as in the case of the systems investigated in the appended papers to this thesis, microscopy methods are preferred. However, ensemble techniques are useful for charactering monodisperse samples, as for example used in Paper IV to characterise the size and concentration of the used gold nanoparticles (AuNPs).

5.7.5 Detection and quantification limits

Although the particle information from different label-free optical techniques is similar in the case of small nanoparticles, the detection limits of the different techniques are not the same. For example, iSCAT can detect down to 9 kDa molecules [36] and darkfield methods can detect particles down to around 5 nanometres in size [23,200], whereas the detection limit for optical field measurements is slightly below 100 nm in diameter [109,201]. Therefore, there is a wide range of particle sizes which optical field measurements cannot currently detect, which limits its use in particle characterisation.

However, in addition to a lower detection limit, many characterisation methods have an upper size limit regarding accurate signal-particle properties relation. For example, only transmission methods have a single-valued relation between measured particle signal and size (Section 5.7.2). Therefore, methods that obtains the complex-valued optical field can be used to estimate polarizability in both the small and large particle limits without particle size and shape information (Section 3.3). Non-transmission methods require both particle shape and size information when relating the scattering signal to particle properties, which limits their ability of estimating polarizability. Instead, the size-signal relation for non-transmission methods can be used to estimate particle shape [43]. Since the investigations of Papers II-V involve multiparametric characterisation in terms of size and polarizability for both nanoparticles and particles with a size comparable to the wavelength of visible light, the quantitative properties of optical field measurements motivated its use as the main experimental technique.

6

Summary of results

"Because I enjoy it."
Michelson's answer to Einstein's question regarding why he spent so much effort on measuring the natural constants. [202][*]

The general scope of this thesis work is to contribute to bridging the quantitative gaps of optical microscopy-based characterisation of particles in the nano-submicron size range. Specifically, the goal is to contribute to solving some of the current limitations regarding multiparametric particle characterisation, with a particular focus on particle size, material, and shape. I have addressed this by being part of developing several different optical imaging-based characterisation methods, with each appended paper being based around one such method development.

Paper I focuses on the quantification of the hydrodynamic boundary conditions for biological nanoparticles using two-dimensional flow nanometry (2DFN). Papers II-V focus on multiparametric characterisation of suspended subwavelength-sized particles using optical scattering microscopy. In Paper II, holographic nanoparticle analysis (H-NTA) is introduced, where the optical phase shift was used to characterise nanobubbles in the presence of dielectric aggregates. In Paper III, H-NTA is combined with deep learning to accurately quantify both particle size and refractive index directly from the optical scattering pattern, which enables sub-second temporal analysis of both size and refractive index. In Paper IV, twilight off-axis holography is introduced, where the improved detection limit and quantitative signal were used to characterise the interaction between herpes simplex virus (HSV) and gold nanoparticles (AuNPs). In Paper V, dual-angle interferometric scattering microscopy (DAISY) is introduced, which extends the size range of simultaneous size and refractive index quantification using optical microscopy images into the nanoparticle regime, where the relative value of the size estimate from optical scattering and hydrodynamic radius enables estimation of the particles internal mass distribution. For details beyond the following summaries, see the appended papers to this thesis.

[*] Translation of: Einstein, der Michelson in seinem letzten Lebensjahre fragte, warum er auf die Genauigkeit der Bestimmung gerade dieser Naturkonstanten so ungeheure Mühe verwende, erhielt darauf die für Michelson so charakteristische Antwort: "Weil es mir Spaß macht." [202].

6.1 Paper I

This investigation is based upon two challenges regarding relating the diffusivity of nanoparticles to particle properties. First, when relating nanoparticle diffusivity to size, the no-slip boundary condition is commonly assumed. This assumption cannot be derived from first principles and direct evaluation of the boundary condition for biological nanoparticles is difficult using existing methods [40,134,203]. Second, when deviations from no slip occurs, the equations describing confined nanoparticle diffusion close to a planar surface are uncertain [137]. Thus, to improve particle estimations using their diffusivity there is a need for new approaches to experimentally quantify the hydrodynamic boundary conditions for nanoparticle systems in general, and mobility of nanoparticles close to a surface with partial slip in particular.

To investigate these questions in the context of biological nanoparticles close to a supported lipid bilayer (SLB), 2DFN (Section 5.5) was used to simultaneously measure particle size and diffusivity of both extracellular vesicles (EVs) and POPC liposomes (Figure 18a). When inspecting the flow-induced velocity and the diffusivity of individual particles, the data is not continuously distributed but is instead gathered in clusters (Figure 18b). This data clustering is a result of the lipid vesicles being tethered by a discrete number of tethers. Within each cluster only particle size varies, which opens up the possibility to fit the measured size-diffusivity relation using the slip lengths b as fitting parameter (Figure 18c).

When deriving the size-diffusivity expression under the assumption of short slip lengths, $b \ll R$, the distance between the nanoparticle and the SLB, δ, the slip length at the SLB interface, b_i, and the slip length at the vesicles, b_p, enter the expression as a sum. Thus, the size-diffusivity relation has two fitting parameters, $b_\mathrm{ef} \equiv \delta + b_\mathrm{i} + b_\mathrm{p}$ and D_T, where D_T is the diffusivity of a tether without any vesicle. Measurements of POPC vesicles in different buffer salt concentrations resulted in a b_ef of around 21-26 nm, whereas measurements of the EVs resulted in a b_ef of $\sim$31 nm. These lengths are considerably longer than the height of the PEG2000 in the SLB, which is $\sim$4 nm [204], and the length of the DNA tether, which is $\sim$15 nm, that together set a range of potential b_ef values if the no-slip boundary condition occurs. Since the slip length is expected to be similar for the POPC liposomes and the EVs, the difference in b_ef is likely due to the complex membrane composition of EVs, with protruding proteins and hydrocarbons increasing the particle-surface distance [205].

Assuming the same slip at both the nanoparticle and the SLB gives a slip length for POPC of around 8-11 nm, which is similar to the literature value for DOPC SLBs of 6 ± 0.5 nm that was measured using a surface force apparatus [149]. However, it should be noted that the used expression in Paper I to obtain the slip length is not an exact solution [137]. For this reason, the results should be considered as evidence of deviation from no slip and the values should be interpreted as effective slip lengths obtained using the short slip length approximations.

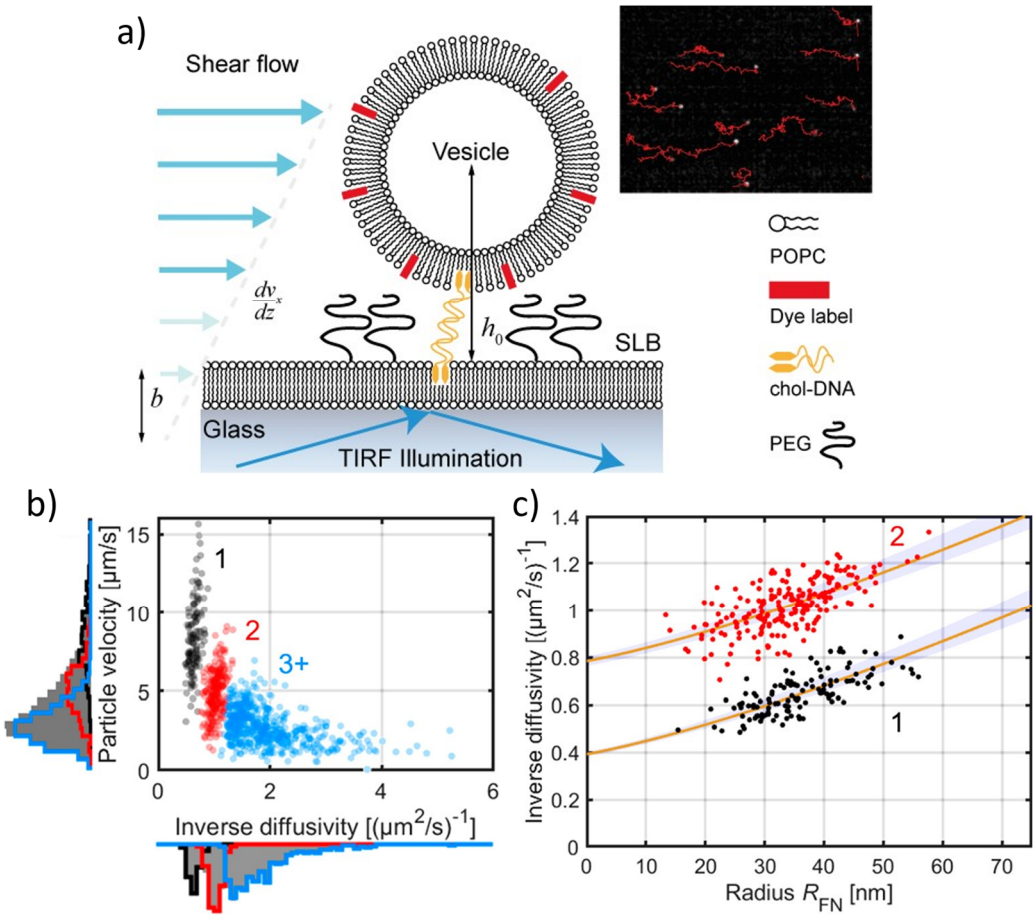

Figure 18 Two-dimensional flow nanometry (2DFN) of tethered vesicles and the subsequent data analysis. (a) Illustration of the 2DFN concept. Labelled vesicles are linked to a supported lipid bilayer (SLB) using cholesterol-DNA-tethering within a microfluidic channel. A shear-flow is applied and the two-dimensional movement of the vesicles are tracked using fluorescence microscopy. b indicates the potential slip length of the SLB and h_0 is the distance from the centre of the particle to the SLB. Inset: fluorescence micrograph showing the shearing of vesicles in the field of view with tracks highlighted in red. (b) Flow induced particle velocity versus inverse diffusivity for POPC liposomes tethered to and SLB consisting of POPC. The different colours indicate the number of tethers (1, 2 and 3+). (c) Inverse diffusivity versus R_{FN} for the first two vesicle-tether clusters in (b). The estimated values from the least-square fit (yellow lines) are $b_{ef} = 22.8 \pm 6.3$ nm and $D_T = 2.56 \pm 0.07$ μm²/s (mean ± 95% CI, visualised using the shaded blue region). Adapted from [206] under CC-BY license.

6.2 Paper II

This investigation is based upon extending the material sensitivity of optical characterisation of suspended particle mixtures. Although the optical scattering intensity often is used to estimate particle refractive index [42], the scattering intensity cannot differentiate between particles that have a positive or negative refractive index difference to the surrounding media. This particularly limits quantitative optical particle characterisation of samples containing mixtures of nanobubbles and other dielectric particles that are potentially generated during the sample preparation [63].

To overcome this limitation, H-NTA is here introduced, which is a single-particle characterisation method based on off-axis holographic imaging (Section 5.1.1) and

particle sizing using the Stokes-Einstein relation (Section 4). By combining the integrated phase shift and the hydrodynamic radius of individual particles, the refractive index of the detected particles is obtained. First, H-NTA was validated using mixtures of standard dielectric particles, where it accurately could distinguish particles based on their diffusivity and integrated phase shift. Thereafter, H-NTA was used to characterise samples containing surfactant stabilised nanobubbles, where the sign of the phase shift was used to differentiate between nanobubbles and potential dielectric particles (Figure 19). The sample contained both particles with a positive and negative phase shift, where the particles with a negative phase shift disappeared after pressure treating the sample. This shows that the detected particles consist of both nanobubbles and dielectric particles. Moreover, the relation between the phase shift and hydrodynamic radius indicates that both the nanobubbles and dielectric particles are not spherical particles but instead aggregates (Section 2.3), where the nanobubble aggregates have a fractal dimension of around 2.3. Note that some of the correlation between hydrodynamic radius and particle refractive index in Figure 19 come from the data analysis, as discussed in detail in Section 4.3.1.

Combined, these results illustrate that optical field imaging, or quantitative phase microscopy, can be used to characterise samples beyond what is possible using optical scattering intensity techniques.

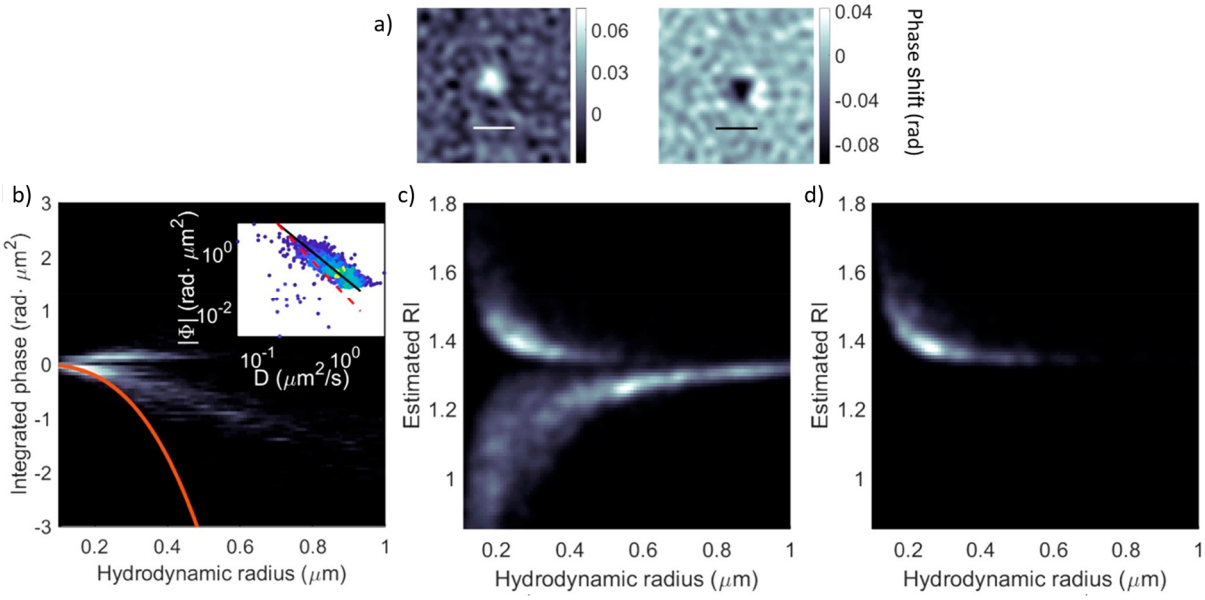

Figure 19 Quantification of hydrodynamic radius and refractive index (RI) of nanobubbles using holographic nanoparticle analysis (H-NTA). (a) The phase shift allows for a direct differentiation between particles and bubbles based on the sign of the phase shift. The scalebars are 2 μm. (b) The scaling of the integrated phase shift with hydrodynamic radius for the bubble population is not consistent with spherical, homogeneous bubbles with a refractive index of 1.0 (red line in the main figure, red dashed line in the inset). Rather, the phase shift scales as if they are formed by aggregation of smaller bubbles with a fractal dimension on 2.3. Inset: the fractal dimension is the slope of the black line in the log-log plot. Here, only the bubble population was considered. (c) The estimated refractive index of both bubbles and particles approaches 1.33 with increasing size. (d) Following pressurisation of the bubble solution, the population of detections having a refractive index < 1.33 disappeared. Adapted with permission from [108]. Copyright 2020 American Chemical Society.

6.3 Paper III

The purpose of this investigation is to improve size and refractive index quantification of subwavelength-sized particles without relying on the Stokes-Einstein relation, as diffusivity-based sizing cannot be applied for dynamically changing particles or for particles in unknown surrounding media. One alternative size estimation approach is to fit the optical scattering pattern to Mie theory calculations (Section 3.3.2). Previous implementations of this approach, however, either only measure dielectric particles that are larger than the wavelength of light or cannot follow the same particle over time as the implementation do not rely on imaging [44,102,207]. Thus, the applicability of such scattering-based particle sizing is currently limited, which this work attempts to extend.

To overcome these limitations, H-NTA was combined with a deep learning-based analysis called weighted average convolutional neural network (WAC-NET). The WAC-NET was trained using Mie simulations combined with the experimental resolution and noise to characterise both particle size and refractive index using optical scattering images without relying on information about particle diffusivity. The performance was subsequently evaluated using experimental data of particles with known size and refractive index. For polystyrene particles which according to the manufacturer had a radius of 228 ± 6.8 nm, the WAC-NET correctly estimated both the radius and refractive index on the single-particle level after only a few particle observations, where the standard approach (diffusivity-based particle sizing) did not converge even after 60 particle observations (Figure 20a-b). The standard deviation of the WAC-NET approach reached ±11.9 nm in radius and ±0.03 in refractive index units using 60 observations, which is close to the distribution width from the particle supplier.

After the WAC-NET was validated using several different standard particles and measurement in media with different refractive indices, its ability of measuring dynamically changing particle samples was evaluated using a solution of 31 nm radius polystyrene nanoparticles during salt-induced clustering. Since aggregates are not homogenous spheres, the quantified size and refractive index are effective particle parameters. However, these effective parameters can in turn be related to the number of monomers and the fractal dimension of the cluster [47] (Section 2.3). As seen in Figure 20c-g, the size and refractive index change over time while the fractal dimension is approximately constant, demonstrating that the clustering process is dynamic and has a reversible nature.

In conclusion, this work shows that the size and refractive index can accurately be measured for particles with a minimum radius of $\sim$150 nm using only a few particle observations. The reason for this lower size limit comes from the challenge of distinguishing particle size from the limited resolution of the microscope. However, compared to diffusivity-based sizing, the WAC-NET analysis requires approximately a factor of 100 fewer observations to achieve the same accuracy for individual particles and it can also be used in different sample media without knowing the media viscosity or refractive index, which extends the applicability of optical particle characterisations.

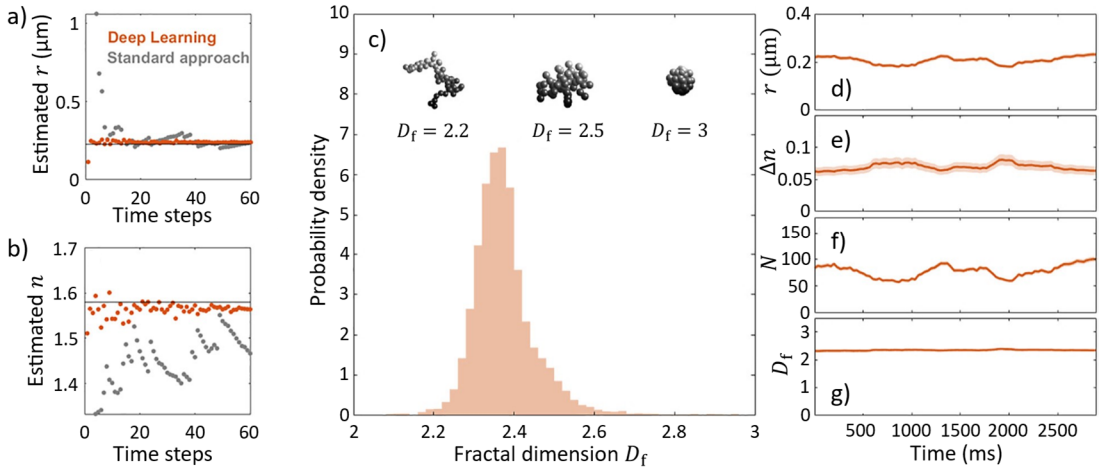

Figure 20 Weighted average convolutional neural network (WAC-NET) based particle characterisation of homogeneous spheres and nanoparticle clusters. (a-b) The WAC-NET approach correctly estimates both the size (a) and refractive index (b) for 0.228 ± 0.0068 μm radius polystyrene particles using only a few particle observations, where the standard approach (diffusivity-based particle sizing) has not fully converged even for 60 particle observations. (c) The WAC-NET approach gives an average fractal dimension D_f close to 2.35 for salt-induced clustering for 31 nm radius polystyrene nanoparticles. The insets show some pictorial depictions of possible clusters for three different fractal dimensions. (d–g) Time-resolved behaviour of a representative cluster, characterised in terms of its radius r (d), refractive index difference Δn (e), number of monomers N (f), and fractal dimension D_f (g). While r, Δn, and N greatly vary over time, D_f remains stable. The shaded regions represent the estimated standard deviation of the error. The detected particles are here analysed using a moving window of 20 observations, acquired at a frame rate of 30 frames per second. Adapted from [56] under CC-BY license.

6.4 Paper IV

Related to Paper II, the purpose of this investigation is to lower the detection limit of H-NTA while also maintaining the material sensitivity. In off-axis holography, one limiting factor for detecting single nanoparticles is the signal-to-background ratio. This limitation stems from the fact that a coherent background signal is needed to quantify relative phase shifts, but with a too low signal-to-background ratio, the background signal risks saturating the image before the particle can be detected.

To improve the signal-to-background ratio compared to ordinary off-axis holography twilight off-axis holography is here introduced (Section 5.1.2), which consists of an off-axis holographic microscope augmented with a semi-transparent low frequency attenuation filter (LFAF) that attenuates the background signal. When using an LFAF, the illumination can be increased to improve the particle signal without increasing the background signal since the particle signal is to a first approximation unaffected by the LFAF. The use of twilight holography for characterising particles is here referred to as twilight nanoparticle tracking analysis (tNTA). Since the LFAF affects the background signal, it also affects the quantified particle signal as it is normalised to the background signal (Figure 21). However, this effect can be compensated using a single complex-valued filter constant during the image processing. From this filter constant and the estimations of the noise signal, tNTA has four times higher signal-to-background ratio compared to H-NTA while the noise in the images only increased around 20-25%.

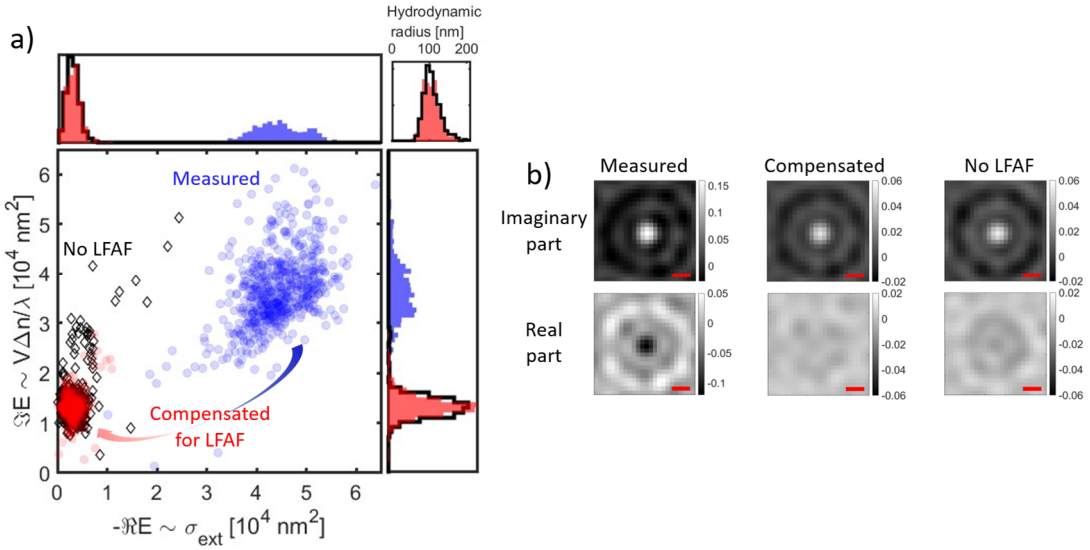

Figure 21 Compensation of the low frequency attenuation filter (LFAF) in the post processing. (a) The LFAF compensation factor is obtained by first quantifying the optical signal from 105 nm radius polystyrene spheres both with (blue symbols and blue histograms) and without (open, black symbols and black outlined histograms) the LFAF. The red symbols and histograms correspond to the population measured using the LFAF after compensation. Note that the inferred optical signal and the hydrodynamic radius are similar after compensation. (b) Images of the real and imaginary parts of the optical signal both with and without the LFAF, showing the similarity of the optical signal after compensation and without the LFAF. The scalebars correspond to 500 nm.

To investigate the ability of tNTA to quantify material information of particle complexes consisting of both dielectric and metallic particles, measurements were done using silica-AuNP particle complexes formed during salt-induced aggregation at different AuNP concentrations. The data indicates that the imaginary part of the optical signal reflects the silica particle even as 5 nm radius AuNPs binds to the silica particle, whereas the negative integrated real part of the optical signal reflects the amount of bound AuNPs. This material sensitivity of tNTA comes from that AuNPs have a high extinction cross section compared to the silica particle, where the integrated real part relates to the extinction cross section (Section 3.3.4), and that the integrated imaginary part primarily reflects the dielectric signal of the particle complex (Section 3.3.3).

The material sensitive particle signal of tNTA was thereafter used to investigate the interaction between tannic acid functionalised AuNPs (TaAuNPs) and HSV type 2 (HSV-2, Section 2.2). When measuring HSV-2, AuNPs, and TaAuNPs separately (Figure 22a), few particle detections were observed compared to the expected concentrations. This is due to the fact that the 5 nm radius AuNPs are well below the detection limit of the microscope whereas HSV-2 is just at the limit of detection.

When the HSV-2 sample was mixed with the TaAuNPs using a TaAuNP concentration of around 3×10^{12}/ml (Figure 22b and d), the number of particle detections became similar to the HSV-2 concentration from darkfield measurements. Moreover, the detected particle signals have both prominent imaginary parts and negative real parts, which indicates TaAuNP binding to HSV-2. At an HSV-2 concentration of around 10^9/ml, the TaAuNPs induced aggregation in the HSV-2 suspension as observed from

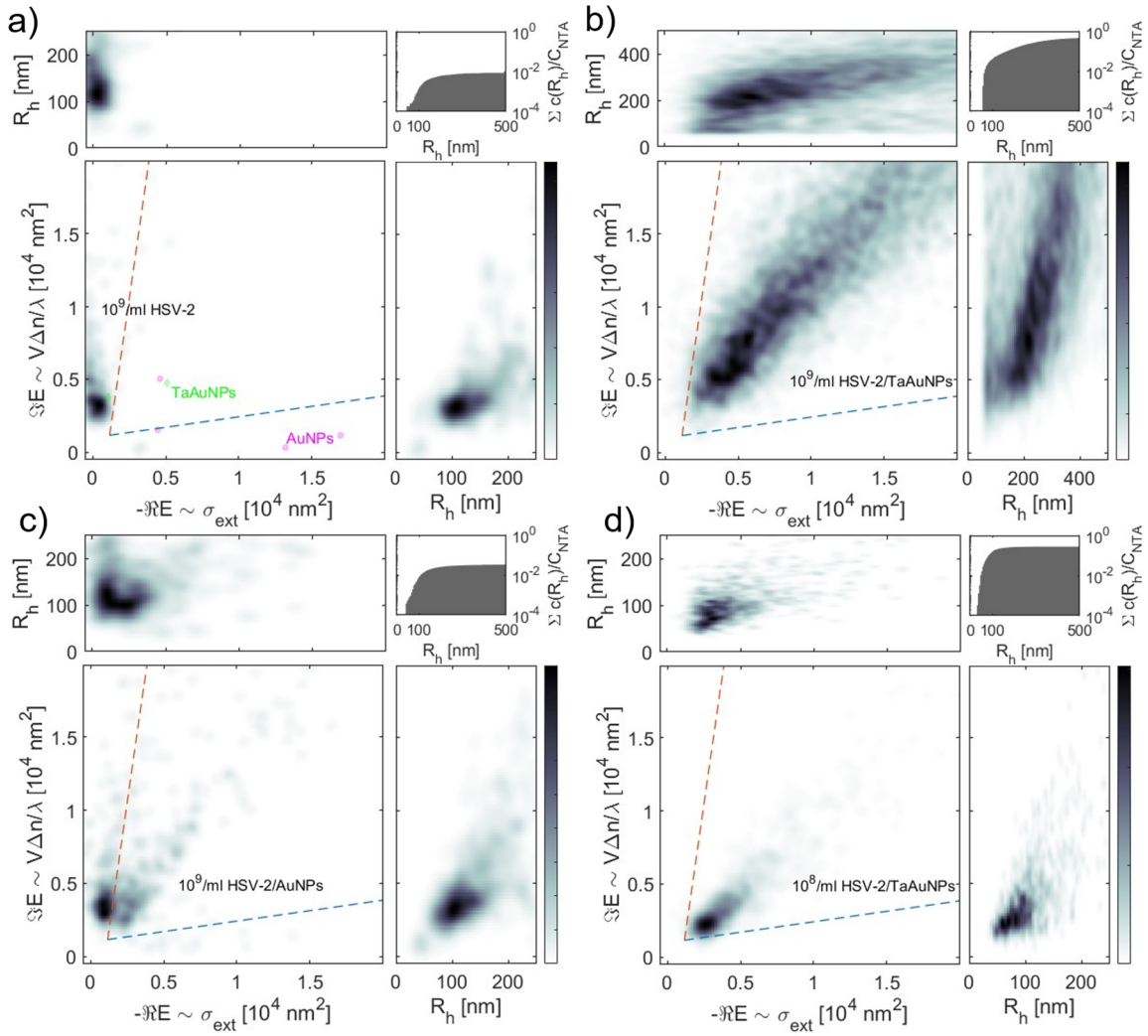

Figure 22 Twilight off-axis holography (tNTA) measurements of herpes simplex virus, gold nanoparticles (AuNPs) and tannic acid AuNPs (TaAuNPs). (a) HSV-2, AuNPs and TaAuNPs when measured separately. Only a small fraction of the HSV-2 population is detected in tNTA compared to the HSV-2 concentration, where the particle sizes are significantly larger than the expected literature value. Only a handful of detections are made in the pure AuNP and TaAuNP samples. (b) ~10^9/ml HSV-2 when mixed with TaAuNPs, for which the measured particle concentration is close to the HSV-2 concentration, the integrated real part ($\Re E$) shifts and a broad hydrodynamic radius distribution is induced, which all indicate HSV-2/TaAuNP binding and particle complex aggregation. (c) ~10^9/ml HSV-2 when mixed with AuNPs, where the concentration is more than order of magnitude lower than the HSV-2 concentration and the only a small shift in $\Re E$ occur. (d) ~10^8/ml HSV-2 when mixed with TaAuNP, where the concentration is close to the HSV-2 concentration, the hydrodynamic radius agrees well with the literature value for HSV-2 [208], and the shift in $\Re E$ indicate TaAuNP binding.

the broad hydrodynamic radius and optical field distributions, whereas at an HSV-2 concentration of around 10^8/ml, both the particle size and the integrated imaginary part were similar to expected values for HSV-2 [208,209]. When the TaAuNPs were changed to AuNPs, the binding to HSV-2 was much less (Figure 22c), indicating that the tannic acid functionalisation promotes binding to HSV-2. The difference in HSV-2 interaction between TaAuNPs and AuNPs was also observed in viral inhibition assays, where the tannic acid functionalisation significantly decreased the viral infectivity. Moreover, when relating the integrated imaginary part and hydrodynamic radius to

particle refractive index, the obtained refractive index for the HSV-2/TaAuNP particle complex of around 1.44 is similar to that of intact viruses [15]. This indicate that the anti-viral properties of tannic acid functionalised AuNPs originate from physical hindrance rather than disrupting the virus.

In conclusion, this work shows that the use of an LFAF improves the detection limit while maintaining a quantitative optical field signal. This enables that hydrodynamic radius, dielectric particle mass, and the AuNP mass can all be quantified for individual suspended nanoparticle complexes. This shows that the optical signal both has material sensitivity and is quantitative for particle complexes, which is something that is less explored in previous investigations using optical particle characterisation.

6.5 Paper V

The purpose of this investigation is to extend size and refractive index quantification of subwavelength-sized particles using the optical scattering signal compared to Paper III. In Paper III, the smallest particle radius the method accurately could characterise was $\sim$150 nm, where this size limit comes from the challenge of distinguishing particle size from the limited resolution of the microscope. Inspired by multi-angle light scattering (MALS) techniques [48], particle size can be estimated from the optical scattering signal measured at two well separated angles relative to the incoming illumination signal with no special requirement on spatial resolution (Section 5.3). Previously, such particle sizing has only been used in ensemble measurements or snapshot observations [48], where its combination with microscopy imaging is less explored.

To enable optical imaging at two well separated scattering angles with a detection limit approaching the nanoscale, interferometric scattering microscopy (iSCAT) is here combined with twilight off-axis holography to create DAISY (Section 5.3). The resulting size estimate, called the DAISY radius, is defined as the smallest radius of a homogeneous sphere in water having the same scattering ratio and polarizability, where the theoretical relation can for example be obtained using Mie theory (Section 3.3.2).

When measuring the DAISY radius for spherical particles with different refractive indices, all samples followed a one-to-one relation with the hydrodynamic radius (Figure 23a). The DAISY radius also remained stable when measuring particles in media with different refractive indices and viscosities (Figure 23b). Moreover, by combining the DAISY radius with the optical field information from twilight off-axis holography, the refractive index difference to the surrounding media was accurately estimated for four different particle samples, where the refractive index estimate also followed the expected change in different surrounding media (Figure 23b).

Since the optical scattering ratio is related to the optical form factor (Section 3.3.1), the DAISY radius depends on both particle size and the mass distribution within the measured particles. In turn, the hydrodynamic radius reflects the outer particle radius. Thus, the relative value of the two size estimates gives information about the internal mass distribution (Figure 23c-d). This property of DAISY was used to investigate both

aggregates of polystyrene particles and fetal bovine serum (FBS). The DAISY-hydrodynamic radius values for both samples deviated from the one-to-one relation observed for spheres. Note that no properties of the particle so far need to be assumed, which shows that DAISY can differentiate different particle types in a generic manner. When compared with theoretical expressions for fractal aggregates, the polystyrene aggregates and FBS detections correspond to a fractal dimension of around 2.0 and 1.9, respectively, which is similar to literature values [73,77,78].

In conclusion, this work shows that DAISY can estimate both size and refractive index of individual particles without relying on the size-diffusivity relation, where the relation between the DAISY radius and hydrodynamic radius can also be used to estimate particle shape with no prior information required. The scattering-based size estimate works for particle sizes much smaller than the diffraction limit, overcoming the lower size limitations of Paper III. Combined, DAISY advances multiparametric optical particle characterisation in the nano-subwavelength regime.

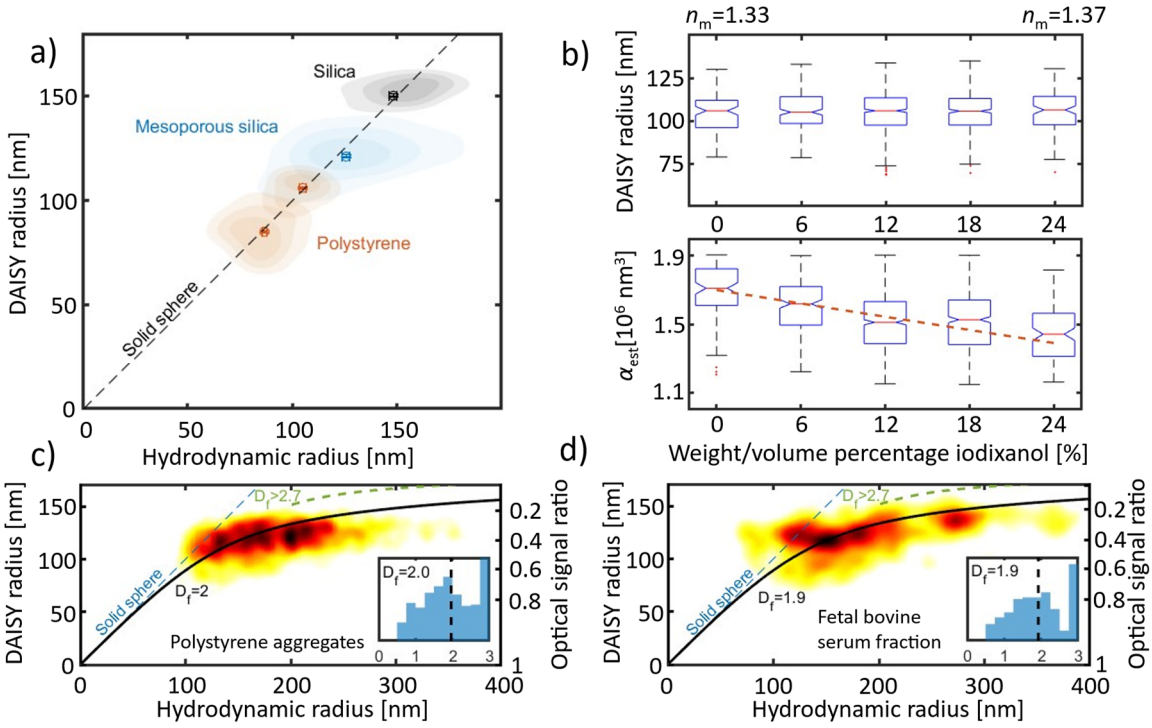

Figure 23 Dual-angle interferometric scatting microscopy (DAISY) particle characterisation and its use to differentiate between solid spheres and aggregates. (a) The DAISY radius and hydrodynamic radius for two polystyrene samples, one silica sample, and one mesoporous silica sample, where all particles follow a one-to-one relation with the hydrodynamic radius (dashed line). (b) The DAISY radius and polarizability as a function of the water-iodixanol concentration for 105 nm polystyrene particles without including information about the changed media in the parameter estimation. The DAISY radius remains the same for all different media whereas the polarizability decreases according to theory as the refractive index difference to the media decreases (dashed line). (c-d) DAISY radius as a function of hydrodynamic radius for (c) salt-induced aggregation of 35 nm radius polystyrene particles and (d) fetal bovine serum (FBS) after size-exclusion chromatography. The detections deviate from the one-to-one relation as for spheres (solid line), where the particle observations agree with fractal aggregates (blue dashed line). The green dashed lines correspond to a fractal dimension of 2.7, which is used separate true aggregate detection from that of spheres with a hydrodynamic radius larger than 200 nm. The insets are the single-particle fractal dimension for the observed particles.

7

Conclusions and future outlook

History is affected by discoveries we will make in the future.
– Sir Karl Popper[*]

The goal of this thesis is to contribute to bridging the quantitative gap in particle characterisation of nano-submicron sized particles using optical scattering microscopy. To conclude the work in this thesis, Paper I presents a method that to the best of my knowledge is the first being capable of quantifying the hydrodynamic boundary condition of biological nanoparticles, including measurements that also clarify the diffusivity of surface tethered nanoparticles. Papers II-V expands the quantitative capabilities of optical characterisation for nano-submicron sized particles, with a particular focus on particle material, size, and internal mass distribution. This was done by extending the capabilities of off-axis holography regarding characterisation of suspended particles, where the optical field information can be directly related to particle properties (Section 3.3). For example, Papers II and IV show that nanobubbles, viruses and gold nanoparticles all can be distinguished based on their complex-valued optical field, where the optical signal accurately relates to both dielectric and gold mass even in the case of virus-gold nanoparticle complexes. Moreover, Papers III and V show that particle size and refractive index can be simultaneously quantified from optical microscopy images for both nanoparticles and subwavelength-sized particles, which enable investigations of particle size without relying on diffusivity-based particle sizing. The optical size estimates also enabled investigations into particle dynamics, as shown in Paper III, and estimations of the internal mass distribution of individual particles by combining the optical size estimate with the hydrodynamic radius, as shown in Paper V. Combined, these papers advance quantitative particle characterisation, in particular for heterogenous particle suspension.

Although I hope that this thesis shows that the gap regarding quantitative particle characterisation is now narrower than before, there is still work left to be done. When looking forward, the main targets are to push the limits of multiparametric particle characterisation using optical field imaging, for example by lowering the detection limit

[*] Sir Karl Popper (1902-1994) was a philosopher, academic and social commentator. Popper is particularly known for promoting empirical falsification instead of classical inductivism.

and to extend the investigations to systems of higher complexity. In particular, this involves further developing dual-angle interferometric scattering microscopy (DAISY) as a generic measurement platform for particles on a surface, particles interacting with cells, as well as exploring the use of twilight holography as a biosensor.

7.1 Size dynamics of surface-bound particles

Interferometric scattering (iSCAT) microscopy is most often used to estimate particle mass of surface-bound nanoparticles without any single-particle size information [23]. Since DAISY does not rely on particle motion to estimate particle size, it could be used to extend the available information about surface-bound nanoparticles to include size and mass dynamics.

Since the measurement platform for DAISY already is developed, the focus is the experimental systems that could benefit from such a particle analysis. One such system is lipid nanoparticles and their interaction with cell membrane mimics. Lipid nanoparticles are used as delivery vehicles of molecules into cells, as used by Moderna and Pfizer in their COVID-19 vaccines [210,211]. Lipid nanoparticles often contain ionisable lipids to promote endosomal escape [212], where a charged supported lipid bilayer (SLB) formed on mesoporous silica has previously been used as a cell mimic to investigate the interaction between lipid nanoparticles and the endosome membrane [213]. In the supporting information to Ref. [213] they show that the same measurement platform can be used to investigate fusion between lipid nanoparticles and an SLB. Since the iSCAT signal is sensitive to the depth position of the particles, it should be possible to follow the depth position between the particle and the SLB during the fusion process. Combined with forward scattering in DAISY, a single measurement would contain information regarding size, mass, and position dynamics, which could be used to better understand lipid nanoparticle-SLB interaction during endosomal escape [212].

Preliminary measurements using only iSCAT indicates that it is possible to detect lipid nanoparticles attached to an SLB, allowing the signal and particle position to be followed over time when changing the surrounding media. However, individual lipid nanoparticles with a radius of around 50-70 nm are currently not detectable using twilight holography, which future developments of DAISY will need to solve. The challenges will be combining accurate particle signal quantification with a frame rate approaching 1000 frames per second to capture the particle dynamics. This will likely require small field of views and state-of-the-art cameras. However, if realised, this would enable detailed characterisation of lipid nanoparticle dynamics beyond what is possible using existing techniques, where the platform could also be used for generic investigations into the interaction between biological nanoparticles and cell mimics such as SLBs.

7.2 Twilight holography as a biosensor for suspended particles

Biosensors are used to detect the presence of specific particles/molecules in a solution. For modern biosensors there are three key challenges: assay sensitivity, response time, and selectivity [214]. In Paper IV, the binding between tannic acid modified gold nanoparticles (TaAuNPs) and herpes viruses resulted in that the optical signal became higher than the limit of detection, where the interaction occurred directly upon mixing the samples. Since it is also possible to differentiate between different particle complexes directly using their complex-valued optical field and size, surface functionalised metallic nanoparticles combined with optical field measurements could potentially work as a quick and sensitive biosensor with a low risk of false positives.

Initial data from twilight off-axis holography indicate the possibility of detecting particles down to a concentration of around 100 fM (Figure 24). Biotinylated POPC vesicles with a radius of around 150 nm were here used as a particle mimic and PEGylated 25 nm diameter gold nanoparticles (AuNPs) functionalised with streptavidin were used as the particles binding to the vesicles. The lower concentration limit comes partly from the used microfluidics, where only a limited measurement volume passed through the imaging region during the video recording, and partly from the number of gold nanoparticle aggregates present in the sample before any the target particles have been added. The detection can therefore likely be improved further, although the current limit of 100 fM is already better than comparable particle detection methods using gold nanoparticle binding [215].

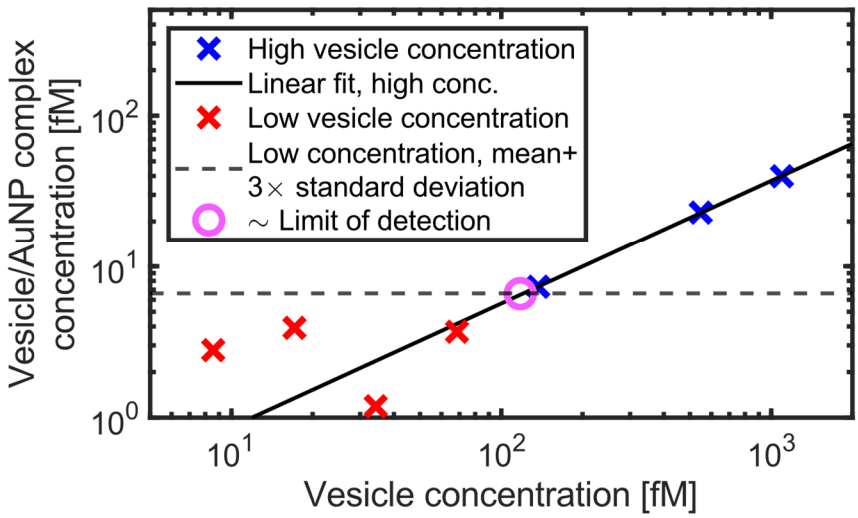

Figure 24 Preliminary twilight holography measurements of the lower concentration detection limit using biotinylated POPC vesicles with a radius of around 150 nm and 25 nm diameter gold nanoparticles (AuNPs) functionalised with PEG and streptavidin. Only particles within a limited interval of size, dielectric signal, and metallic signal are included in the analysis to minimise potential false positives. The concentration detection limit is estimated by taking the average detected concentration when no target particles are present and adding three standard deviations to that value.

7.3 Extending optical characterisation to intracellular structures

One of the major remaining challenges of particle characterisation using optical scattering microscopy is multiparametric characterisation of nanoparticles on/inside cells. Since DAISY can be used to estimate particle size in unknown biological environments, it has the potential to be used for characterisation of intracellular structures/particles. However, characterising particles inside cells using optical scattering microscopy is different from characterising particles on a surface or in solution, as the interior of the cell is a crowded environment [216]. Combined with the limited spatial resolution of optical microscopy (Section 3.2), it is generally challenging to distinguish individual nanoparticles inside a cell using the optical scattering signal. Thus, an extension of DAISY for analysis of entities inside cells will require means to suppress the background signal while simultaneously improving the detection limit.

The solution to this challenge most likely involves performing DAISY using confocal iSCAT and deep learning. Confocal microscopy is different from widefield microscopy, where the latter is the measurement configuration used in the appended papers to this thesis. Confocal microscopy is based around scanning a focused beam across the imaging region of interest where a pinhole filter is used to select the signal originating from a limited measurement volume [217]. This minimises the background signal in the resulting image. The difference in image quality between widefield and confocal iSCAT is presented in Ref. [218], where confocal iSCAT was used to investigate the interaction between a SARS-CoV-2 virion and a cell. Thus, Ref. [218] shows the possibility of investigating biological nanoparticles in the context of cells using confocal iSCAT, where confocal DAISY could aid in solving the remaining quantitative challenges.

Once developed, one interesting question to address would be to follow cellular uptake of nanoparticles and the different particle dynamics thereafter. For example, since particle uptake changes the surrounding environment of the particle, optical scattering measurements should be able to resolve the uptake event and the subsequent size and mass dynamics. One such particle system of high interest is lipid nanoparticles [212]. In particular, the functional delivery of cargo into the cytosol of cells is only about 2% [219]. Confocal DAISY has the potential to investigate the dynamics of lipid nanoparticles when inside the endosomes after the initial cellular uptake, which could aid in understanding the low delivery efficiency. If combined with simultaneous fluorescence imaging, such a measurement setup would truly extend the applicability of optical scattering-based particle characterisation into complex biological system. Achieving this in practice will be far from a trivial task as it will require state-of-the-art imaging and image analysis. But given the importance of the unanswered questions such a method could help answering, the roadmap outlined in this section and the ideas presented in this thesis will hopefully guide future development towards solving this grand challenge.

Acknowledgements

The past few years have been an incredible journey, both scientifically and personally. From the bottom of my heart, I want to thank Area of Advance Nano for funding my PhD project and giving me the opportunity to develop my own research ideas.

To Fredrik Höök, my main supervisor and mentor: Thanks for your guidance, scientific insights, and trust. Without you giving me the confidence to explore my crazy ideas this thesis would not have reached the level it did. We said five years ago that we wanted to embark on a creative journey together, and this really exceeded all my expectations.

To Daniel Midtvedt, my co-supervisor and scientific partner in crime: Thanks for your patience and the endless discussions about optics and method development. We have since long reached our initial vision, and we are far from being done yet!

To Elin Esbjörner, my co-supervisor and source of biological insights: Thanks for always being available and letting me test all the different developed methods.

To Eva and Andy: Thanks for inspiring me to start working with microscopy.

To Fredrik E: Thanks for initiating the journey into charactering suspended particles.

To my long list of collaborators over the years: It would not have been possible without you! Special thanks to Emelie, Adrián, Silver, Fredrik E, Benjamin, Berenice, Fredrik S., Petteri, Malgorzata, and Vladimir.

A special thanks to Mattias, Silver, Adrián, Petteri, Henrik, and Julia for proof reading either this thesis or my previous licentiate thesis.

Past and present members of the Biological Physics group: Thanks for a very open and friendly environment, with very interesting, daring, challenging, and entertaining discussions both during and outside work hours. A special thanks to Mattias, Govin, Karin, Silver, Kajsa, Simon, Julia, Petteri, and Adrián, without you the workplace would have been a much less fun place.

To all my friends I have met during my now 10 years at Chalmers: Love you guys! A special thanks to Alvaro, Pluggande 8:an, Roger, Ali, Tuve, and Barbara, for all reminding me that there is more to life than work.

To my family and friends: Thanks for just being who you all are and inspiring me over the years. A special thanks to my mom for being my main scientific inspiration from the day I was born.

To Valeriia: You are such an inspiration to me and I love you.

To my Mormor and Morfar: It is in your memory I try to become a better person for every day that goes by.

Erik Olsén, Göteborg, July 2023

References

[1] D. B. Williams and C. B. Carter, *The Transmission Electron Microscope*, in *Transmission Electron Microscopy* (Springer, 1996).

[2] Y. F. Dufrêne, *Towards Nanomicrobiology Using Atomic Force Microscopy*, Nat Rev Microbiol **6**, 674 (2008).

[3] P. Török and F.-J. Kao, *Optical Imaging and Microscopy: Techniques and Advanced Systems*, Vol. 87 (Springer, 2007).

[4] Nobel Prize Outreach AB 2023, *The Nobel Prize in Physics 1986*, https://www.nobelprize.org/prizes/physics/1986/summary/ (accessed Feb. 05, 2023).

[5] Nobel Prize Outreach AB 2023, *The Nobel Prize in Chemistry 2017*, https://www.nobelprize.org/prizes/chemistry/2017/summary/ (accessed Feb. 05, 2023).

[6] Nobel Prize Outreach AB 2023, *The Nobel Prize in Chemistry 2014*, https://www.nobelprize.org/prizes/chemistry/2014/summary/ (accessed Feb. 05, 2023).

[7] Nobel Prize Outreach AB 2023, *The Nobel Prize in Physics 1953*, https://www.nobelprize.org/prizes/physics/1953/summary/ (accessed Feb. 05, 2023).

[8] Nobel Prize Outreach AB 2023, *The Nobel Prize in Physics 1971*, https://www.nobelprize.org/prizes/physics/1971/summary/ (accessed Feb. 07, 2023).

[9] Nobel Prize Outreach AB 2023, *The Nobel Prize in Chemistry 1925*, https://www.nobelprize.org/prizes/chemistry/1925/summary/ (accessed Feb. 27, 2023).

[10] Nobel Prize Outreach AB 2023, *The Nobel Prize in Chemistry 1982*, https://www.nobelprize.org/prizes/chemistry/1982/summary/ (accessed Feb. 27, 2023).

[11] R. Brown, *XXVII. A Brief Account of Microscopical Observations Made in the Months of June, July and August 1827, on the Particles Contained in the Pollen of Plants; and on the General Existence of Active Molecules in Organic and Inorganic Bodies*, The Philosophical Magazine **4**, 161 (1828).

[12] M. D. Haw, *Colloidal Suspensions, Brownian Motion, Molecular Reality: A Short History*, Journal of Physics Condensed Matter **14**, 7769 (2002).

[13] D. M. Wilkinson, *Brown Knew Particles Were Smaller than Pollen*, Nature **434**, 137 (2005).

[14] A. Einstein, *Über Die von Der Molekularkinetischen Theorie Der Wärme Geforderte Bewegung von in Ruhenden Flüssigkeiten Suspendierten Teilchen*, Ann Phys **322**, 549 (1905).

[15] G. C. Brittain, Y. Q. Chen, E. Martinez, V. A. Tang, T. M. Renner, M. A. Langlois, and S. Gulnik, *A Novel Semiconductor-Based Flow Cytometer with Enhanced*

Light-Scatter Sensitivity for the Analysis of Biological Nanoparticles, Sci Rep **9**, (2019).

[16] E. van der Pol, T. G. van Leeuwen, and X. Yan, *Misinterpretation of Solid Sphere Equivalent Refractive Index Measurements and Smallest Detectable Diameters of Extracellular Vesicles by Flow Cytometry*, Sci Rep **11**, (2021).

[17] G. C. Brittain, M. A. Langlois, and S. Gulnik, *Reply to: Misinterpretation of Solid Sphere Equivalent Refractive Index Measurements and Smallest Detectable Diameters of Extracellular Vesicles by Flow Cytometry*, Sci Rep **11**, (2021).

[18] A. Kamanzi et al., *Simultaneous, Single-Particle Measurements of Size and Loading Give Insights into the Structure of Drug-Delivery Nanoparticles*, ACS Nano **15**, 19244 (2021).

[19] A. C. Madison, A. L. Pintar, C. R. Copeland, N. Farkas, and S. M. Stavis, *Letter to the Editor Concerning "Simultaneous, Single-Particle Measurements of Size and Loading Give Insights into the Structure of Drug-Delivery Nanoparticles,"* ACS Nano **17**, 8837 (2023).

[20] A. Kamanzi, M. Sutton, F. Höök, and S. Leslie, *Response to "Letter to the Editor Concerning 'Simultaneous, Single-Particle Measurements of Size and Loading Give Insights into the Structure of Drug-Delivery Nanoparticles,'"* ACS Nano **17**, 8843 (2023).

[21] Wikimedia Commons contributors, *Biological and Technological Scales Compared*, https://commons.wikimedia.org/w/index.php?title=File:Biological_and_technological_scales_compared-en.svg&oldid=455995727 (accessed Mars 24, 2021).

[22] J. Peatross and M. Ware, *Physics of Light and Optics* (Brigham Young University, 2015).

[23] L. Priest, J. S. Peters, and P. Kukura, *Scattering-Based Light Microscopy: From Metal Nanoparticles to Single Proteins*, Chem Rev **121**, 11937 (2021).

[24] B. Vestad, A. Llorente, A. Neurauter, S. Phuyal, B. Kierulf, P. Kierulf, T. Skotland, K. Sandvig, K. B. F. Haug, and R. Øvstebø, *Size and Concentration Analyses of Extracellular Vesicles by Nanoparticle Tracking Analysis: A Variation Study*, J Extracell Vesicles **6**, (2017).

[25] M. Imanbekova, S. Suarasan, Y. Lu, S. Jurchuk, and S. Wachsmann-Hogiu, *Recent Advances in Optical Label-Free Characterization of Extracellular Vesicles*, Nanophotonics **11**, 2827 (2022).

[26] B. Gul, F. Syed, S. Khan, A. Iqbal, and I. Ahmad, *Characterization of Extracellular Vesicles by Flow Cytometry: Challenges and Promises*, Micron **161**, (2022).

[27] J. Stetefeld, S. A. McKenna, and T. R. Patel, *Dynamic Light Scattering: A Practical Guide and Applications in Biomedical Sciences*, Biophys Rev **8**, 409 (2016).

[28] S. J. Sahl, S. W. Hell, and S. Jakobs, *Fluorescence Nanoscopy in Cell Biology*, Nat Rev Mol Cell Biol **18**, 685 (2017).

[29] S. Kawata, T. Ichimura, A. Taguchi, and Y. Kumamoto, *Nano-Raman Scattering Microscopy: Resolution and Enhancement*, Chem Rev **117**, 4983 (2017).

[30] J. K. Hannestad, S. Rocha, B. Agnarsson, V. P. Zhdanov, P. Wittung-Stafshede, and F. Höök, *Single-Vesicle Imaging Reveals Lipid-Selective and Stepwise Membrane Disruption by Monomeric a-Synuclein*, Proc Natl Acad Sci U S A **117**, 14178 (2020).

[31] B. Špačková et al., *Label-Free Nanofluidic Scattering Microscopy of Size and Mass of Single Diffusing Molecules and Nanoparticles*, Nat Methods **19**, 751 (2022).

[32] D. Sage, L. Donati, F. Soulez, D. Fortun, G. Schmit, A. Seitz, R. Guiet, C. Vonesch, and M. Unser, *DeconvolutionLab2: An Open-Source Software for Deconvolution Microscopy*, Methods **115**, 28 (2017).

[33] X. Bian, C. Kim, and G. E. Karniadakis, *111 Years of Brownian Motion*, Soft Matter **12**, 6331 (2016).

[34] H. P. Erickson, *Size and Shape of Protein Molecules at the Nanometer Level Determined by Sedimentation, Gel Filtration, and Electron Microscopy*, Biol Proced Online **11**, 32 (2009).

[35] G. Young et al., *Quantitative Mass Imaging of Single Molecules in Solution*, Science (1979) **360**, 423 (2018).

[36] M. Dahmardeh, H. M. Dastjerdi, H. Mazal, M. Planck, H. Köstler, and V. Sandoghdar, *Self-Supervised Machine Learning Pushes the Sensitivity Limit in Label-Free Detection of Single Proteins below 10 KDa*, Nature Methods **20**, 442 (2023).

[37] N. Hoshyar, S. Gray, H. Han, and G. Bao, *The Effect of Nanoparticle Size on in Vivo Pharmacokinetics and Cellular Interaction*, Nanomedicine **11**, 673 (2016).

[38] A. Albanese, P. S. Tang, and W. C. W. Chan, *The Effect of Nanoparticle Size, Shape, and Surface Chemistry on Biological Systems*, Annu Rev Biomed Eng **14**, 1 (2012).

[39] S. D. Stellman, *A Spherical Chicken*, Science (1979) **182**, 1296 (1973).

[40] V. P. Zhdanov, *How the Partial-Slip Boundary Condition Can Influence the Interpretation of the DLS and NTA Data*, J Biol Phys **46**, 169 (2020).

[41] D. Midtvedt, E. Olsén, F. Höök, and G. D. M. Jeffries, *Label-Free Spatio-Temporal Monitoring of Cytosolic Mass, Osmolarity, and Volume in Living Cells*, Nat Commun **10**, (2019).

[42] E. van der Pol, F. A. W. Coumans, A. Sturk, R. Nieuwland, and T. G. van Leeuwen, *Refractive Index Determination of Nanoparticles in Suspension Using Nanoparticle Tracking Analysis*, Nano Lett **14**, 6195 (2014).

[43] A. D. Kashkanova, M. Blessing, A. Gemeinhardt, D. Soulat, and V. Sandoghdar, *Precision Size and Refractive Index Analysis of Weakly Scattering Nanoparticles in Polydispersions*, Nat Methods **19**, 586 (2022).

[44] S.-H. Lee, Y. Roichman, G.-R. Yi, S.-H. Kim, S.-M. Yang, A. van Blaaderen, P. van Oostrum, and D. G. Grier, *Characterizing and Tracking Single Colloidal Particles with Video Holographic Microscopy*, Opt Express **15**, 18275 (2007).

[45] M. K. Kim, *Principles and Techniques of Digital Holographic Microscopy*, SPIE Reviews **1**, (2010).
[46] M. Paturzo, V. Pagliarulo, V. Bianco, P. Memmolo, L. Miccio, F. Merola, and P. Ferraro, *Digital Holography, a Metrological Tool for Quantitative Analysis: Trends and Future Applications*, Opt Lasers Eng **104**, 32 (2018).
[47] A. Winters, F. C. Cheong, M. A. Odete, J. Lumer, D. B. Ruffner, K. I. Mishra, D. G. Grier, and L. A. Philips, *Quantitative Differentiation of Protein Aggregates From Other Subvisible Particles in Viscous Mixtures Through Holographic Characterization*, J Pharm Sci **109**, 2405 (2020).
[48] P. J. Wyatt, *Light Scattering and the Absolute Characterization of Macromolecules*, Anal Chim Acta **272**, 1 (1993).
[49] Robert Hooke, *Micrographia, or Some Physiological Descriptions of Minute Bodies Made by Magnifying Glasses, with Observations and Inquiries Thereupon* (Printed by Jo. Martyn, and Ja. Allestry, Printers to the Royal Society, and are to be sold at their Shop at the Bell in S. Paul's Churchyard, London, 1665).
[50] J.-C. Lai, Y.-Y. Zhang, Z.-H. Li, H.-J. Jiang, and A.-Z. He, *Complex Refractive Index Measurement of Biological Tissues by Attenuated Total Reflection Ellipsometry*, Appl Opt **49**, 3235 (2010).
[51] D. K. Cheng, *Field and Wave Electromagnetics*, Second edition (Pearson Education Limited, 2014).
[52] V. Kestens, V. Bozatzidis, P. J. De Temmerman, Y. Ramaye, and G. Roebben, *Validation of a Particle Tracking Analysis Method for the Size Determination of Nano- and Microparticles*, Journal of Nanoparticle Research **19**, (2017).
[53] V. Kestens et al., *Challenges in the Size Analysis of a Silica Nanoparticle Mixture as Candidate Certified Reference Material*, Journal of Nanoparticle Research **18**, (2016).
[54] R. A. L. Jones, *Soft Condensed Matter*, Vol. 6 (Oxford University Press, 2002).
[55] G. Cooper and R. E. Hausman, *The Cell: A Molecular Approach, Fifth Edition* (ASM Press, 2009).
[56] B. Midtvedt, E. Olsén, F. Eklund, F. Höök, C. B. Adiels, G. Volpe, and D. Midtvedt, *Fast and Accurate Nanoparticle Characterization Using Deep-Learning-Enhanced Off-Axis Holography*, ACS Nano **15**, 2240 (2021).
[57] H. M. Mcconnell, T. H. Watts, R. M. Weis, and A. A. Brian, *Supported Planar Membranes in Studies of Cell-Cell Recognition in the Immune System*, Biochim Biophys Acta **864**, 95 (1986).
[58] G. J. Hardy, R. Nayak, and S. Zauscher, *Model Cell Membranes: Techniques to Form Complex Biomimetic Supported Lipid Bilayers via Vesicle Fusion*, Curr Opin Colloid Interface Sci **18**, 448 (2013).
[59] S. Block, B. J. Fast, A. Lundgren, V. P. Zhdanov, and F. Höök, *Two-Dimensional Flow Nanometry of Biological Nanoparticles for Accurate Determination of Their Size and Emission Intensity*, Nat Commun **7**, 12956 (2016).
[60] I. Pfeiffer and F. Höök, *Bivalent Cholesterol-Based Coupling of Oligonucletides to Lipid Membrane Assemblies*, J Am Chem Soc **126**, 10224 (2004).

[61] G. Bordanaba-Florit, F. Royo, S. G. Kruglik, and J. M. Falcón-Pérez, *Using Single-Vesicle Technologies to Unravel the Heterogeneity of Extracellular Vesicles*, Nat Protoc **16**, 3163 (2021).
[62] Y. Couch et al., *A Brief History of Nearly EV-Erything – The Rise and Rise of Extracellular Vesicles*, J Extracell Vesicles **10**, e12144 (2021).
[63] F. Eklund, M. Alheshibri, and J. Swenson, *Differentiating Bulk Nanobubbles from Nanodroplets and Nanoparticles*, Curr Opin Colloid Interface Sci **53**, (2021).
[64] M. Alheshibri, J. Qian, M. Jehannin, and V. S. J. Craig, *A History of Nanobubbles*, Langmuir **32**, 11086 (2016).
[65] E. Stride, T. Segers, G. Lajoinie, S. Cherkaoui, T. Bettinger, M. Versluis, and M. Borden, *Microbubble Agents: New Directions*, Ultrasound Med Biol **46**, 1326 (2020).
[66] K. Grunewald, P. Desai, D. C. Winkler, J. B. Heymann, D. M. Belnap, W. Baumeister, and A. C. Steven, *Three-Dimensional Structure of Herpes Simplex Virus from Cryo-Electron Tomography*, Science (1979) **302**, 1396 (2003).
[67] World Health Organization, *Herpes Simplex Virus*, https://www.who.int/news-room/fact-sheets/detail/herpes-simplex-virus (accessed Mars 21, 2023).
[68] World Health Organization, *Immunization, Vaccines and Biologicals: Herpes Simplex Virus*, https://www.who.int/teams/immunization-vaccines-and-biologicals/diseases/herpes-simplex-virus (accessed Mars 21, 2023).
[69] B. Kaczmarek, *Tannic Acid with Antiviral and Antibacterial Activity as a Promising Component of Biomaterials-A Minireview*, Materials **13**, 3224 (2020).
[70] P. Orłowski et al., *Tannic Acid Modified Silver Nanoparticles Show Antiviral Activity in Herpes Simplex Virus Type 2 Infection*, PLoS One **9**, (2014).
[71] P. Orłowski et al., *Tannic Acid-Modified Silver and Gold Nanoparticles as Novel Stimulators of Dendritic Cells Activation*, Front Immunol **9**, (2018).
[72] P. Orłowski, A. Kowalczyk, E. Tomaszewska, K. Ranoszek-Soliwoda, A. Węgrzyn, J. Grzesiak, G. Celichowski, J. Grobelny, K. Eriksson, and M. Krzyzowska, *Antiviral Activity of Tannic Acid Modified Silver Nanoparticles: Potential to Activate Immune Response in Herpes Genitalis*, Viruses **10**, (2018).
[73] D. W. Schaefer, J. E. Martin, P. Wiltzius, and D. S. Cannell, *Fractal Geometry of Colloidal Aggregates*, Phys Rev Lett **52**, 2371 (1984).
[74] P. Meakin, *Fractal Aggregates*, Adv Colloid Interface Sci **28**, 249 (1987).
[75] C. M. Sorensen, *Light Scattering by Fractal Aggregates: A Review*, Aerosol Science and Technology **35**, 648 (2001).
[76] J. Fung and S. Hoang, *Computational Assessment of an Effective-Sphere Model for Characterizing Colloidal Fractal Aggregates with Holographic Microscopy*, J Quant Spectrosc Radiat Transf **236**, 106591 (2019).
[77] M. Carpineti, F. Ferri, M. Giglio, E. Paganini, and U. Perini, *Salt-Induced Fast Aggregation of Polystyrene Latex*, Phys Rev A (Coll Park) **42**, 15 (1990).
[78] Z. Zhou and B. Chu, *Fractal Study of Polystyrene Latex and Silica Particle Aggregates*, Physica A **177**, 93 (1991).

[79] C. M. Sorensen, *The Mobility of Fractal Aggregates: A Review*, Aerosol Science and Technology **45**, 765 (2011).
[80] P. L. Ma, M. D. Buschmann, and F. M. Winnik, *Complete Physicochemical Characterization of DNA/Chitosan Complexes by Multiple Detection Using Asymmetrical Flow Field-Flow Fractionation*, Anal Chem **82**, 9636 (2010).
[81] M. Lattuada, H. Wu, and M. Morbidelli, *Hydrodynamic Radius of Fractal Clusters*, J Colloid Interface Sci **268**, 96 (2003).
[82] C. Wang, F. C. Cheong, D. B. Ruffner, X. Zhong, M. D. Ward, and D. G. Grier, *Holographic Characterization of Colloidal Fractal Aggregates*, Soft Matter **12**, 8774 (2016).
[83] J. D. Jackson, *Classical Electrodynamics*, Third edition (Wiley, 1998).
[84] J. R. Lakowicz, *Principles of Fluorescence Spectroscopy* (Springer science & business media, 2006).
[85] S. Weisenburger and V. Sandoghdar, *Light Microscopy: An Ongoing Contemporary Revolution*, Contemp Phys **56**, 123 (2015).
[86] B. E. A. Saleh and M. C. Teich, *Fundamentals of Photonics*, Third edition (John Wiley & Sons, 2019).
[87] C. H. Henry and R. F. Kazarinov, *Quantum Noise in Photonics*, Rev. Mod. Phys. **68**, 801 (1996).
[88] G. B. Folland, *Fourier Analysis and Its Applications*, Vol. 4 (American Mathematical Soc., 2009).
[89] Y. Cotte, M. F. Toy, E. Shaffer, N. Pavillon, and C. Depeursinge, *Sub-Rayleigh Resolution by Phase Imaging*, Opt Lett **35**, 2176 (2010).
[90] C. Zhang, *Methods and Instruments for the Measurement of Numerical Aperture for Microscope Objective Lens: A Mini Review*, Review of Scientific Instruments **93**, (2022).
[91] H. Shen, L. J. Tauzin, R. Baiyasi, W. Wang, N. Moringo, B. Shuang, and C. F. Landes, *Single Particle Tracking: From Theory to Biophysical Applications*, Chem Rev **117**, 7331 (2017).
[92] C. F. Bohren and D. R. Huffman, *Absorption and Scattering of Light by Small Particles* (John Wiley & Sons, 1983).
[93] S. A. Maier, *Plasmonics: Fundamentals and Applications* (Springer Science & Business Media, 2007).
[94] F. R. Hallett, J. Watton, and P. Krygsman, *Vesicle Sizing: Number Distributions by Dynamic Light Scattering*, Biophys J **59**, 357 (1991).
[95] P. J. Wyatt, *Submicrometer Particle Sizing by Multiangle Light Scattering Following Fractionation*, J Colloid Interface Sci **197**, 9 (1998).
[96] J.-P. Schäfer, Implementierung Und Anwendung Analytischer Und Numerischer Verfahren Zur Lösung Der Maxwellgleichungen Für Die Untersuchung Der Lichtausbreitung in Biologischem Gewebe, Universität Ulm, 2011.
[97] I. L. Rasskazov, P. S. Carney, and A. Moroz, *STRATIFY: A Comprehensive and Versatile MATLAB Code for a Multilayered Sphere*, OSA Contin **3**, 2290 (2020).

[98] U. Hohenester and A. Trügler, *MNPBEM - A Matlab Toolbox for the Simulation of Plasmonic Nanoparticles*, Comput Phys Commun **183**, 370 (2012).
[99] L. E. Altman, R. Quddus, F. C. Cheong, and D. G. Grier, *Holographic Characterization and Tracking of Colloidal Dimers in the Effective-Sphere Approximation*, Soft Matter **17**, 2695 (2021).
[100] L. E. Altman and D. G. Grier, *CATCH: Characterizing and Tracking Colloids Holographically Using Deep Neural Networks*, Journal of Physical Chemistry B **124**, 1602 (2020).
[101] M. Hannel, C. Middleton, and D. G. Grier, *Holographic Characterization of Imperfect Colloidal Spheres*, Appl Phys Lett **107**, (2015).
[102] E. van der Pol, L. de Rond, F. A. W. Coumans, E. L. Gool, A. N. Böing, A. Sturk, R. Nieuwland, and T. G. van Leeuwen, *Absolute Sizing and Label-Free Identification of Extracellular Vesicles by Flow Cytometry*, Nanomedicine **14**, 801 (2018).
[103] P. Y. Liu et al., *Cell Refractive Index for Cell Biology and Disease Diagnosis: Past, Present and Future*, Lab Chip **16**, 634 (2016).
[104] P. Langehanenberg, B. Kemper, D. Dirksen, and G. von Bally, *Autofocusing in Digital Holographic Phase Contrast Microscopy on Pure Phase Objects for Live Cell Imaging*, Appl Opt **47**, 176 (2008).
[105] F. Zernike, *Phase Contrast, a New Method for the Microscopic Observation of Transparent Objects*, Physica **9**, 686 (1942).
[106] B. Rappaz, P. Marquet, E. Cuche, Y. Emery, C. Depeursinge, and P. J. Magistretti, *Measurement of the Integral Refractive Index and Dynamic Cell Morphometry of Living Cells with Digital Holographic Microscopy*, Opt Express **13**, 9361 (2005).
[107] F. Charrière, A. Marian, F. Montfort, J. Kuehn, T. Colomb, E. Cuche, P. Marquet, and C. Depeursinge, *Cell Refractive Index Tomography by Digital Holographic Microscopy*, Opt Lett **31**, 178 (2006).
[108] D. Midtvedt, F. Eklund, E. Olsén, B. Midtvedt, J. Swenson, and F. Höök, *Size and Refractive Index Determination of Subwavelength Particles and Air Bubbles by Holographic Nanoparticle Tracking Analysis*, Anal Chem **92**, (2020).
[109] J. Cauzzo, N. Jayakumar, B. S. Ahluwalia, A. Ahmad, and N. Škalko-Basnet, *Characterization of Liposomes Using Quantitative Phase Microscopy (QPM)*, Pharmaceutics **13**, (2021).
[110] T. A. Zangle and M. A. Teitell, *Live-Cell Mass Profiling: An Emerging Approach in Quantitative Biophysics*, Nat Methods **11**, 1221 (2014).
[111] J. Reed, J. Chun, T. A. Zangle, S. Kalim, J. S. Hong, S. E. Pefley, X. Zheng, J. K. Gimzewski, and M. A. Teitell, *Rapid, Massively Parallel Single-Cell Drug Response Measurements via Live Cell Interferometry*, Biophys J **101**, 1025 (2011).
[112] M. N. Berberan-Santos, *Beer's Law Revisited*, J Chem Educ **67**, 757 (1990).
[113] S. Khadir, D. Andrén, P. C. Chaumet, S. Monneret, N. Bonod, M. Käll, A. Sentenac, and G. Baffou, *Full Optical Characterization of Single Nanoparticles Using Quantitative Phase Imaging*, Optica **7**, 243 (2020).

[114] Y. F. Huang, G. Y. Zhuo, C. Y. Chou, C. H. Lin, W. Chang, and C. L. Hsieh, *Coherent Brightfield Microscopy Provides the Spatiotemporal Resolution to Study Early Stage Viral Infection in Live Cells*, ACS Nano **11**, 2575 (2017).
[115] Y. Li, H. S. Lim, S. C. Ng, Z. K. Wang, M. H. Kuok, E. Vekris, V. Kitaev, F. C. Peiris, and G. A. Ozin, *Micro-Brillouin Scattering from a Single Isolated Nanosphere*, Appl Phys Lett **88**, 1 (2006).
[116] J. M. Hollas, *Modern Spectroscopy*, Fourth edition (John Wiley & Sons, 2004).
[117] L. von Diezmann, Y. Shechtman, and W. E. Moerner, *Three-Dimensional Localization of Single Molecules for Super-Resolution Imaging and Single-Particle Tracking*, Chem Rev **117**, 7244 (2017).
[118] E. J. van der Vlist, E. N. M. Nolte-'t Hoen, W. Stoorvogel, G. J. A. Arkesteijn, and M. H. M. Wauben, *Fluorescent Labeling of Nano-Sized Vesicles Released by Cells and Subsequent Quantitative and Qualitative Analysis by High-Resolution Flow Cytometry.*, Nat Protoc **7**, 1311 (2012).
[119] D. Kim, N. Oh, K. Kim, S. Y. Lee, C. G. Pack, J. H. Park, and Y. K. Park, *Label-Free High-Resolution 3-D Imaging of Gold Nanoparticles inside Live Cells Using Optical Diffraction Tomography*, Methods **136**, 160 (2018).
[120] S. Jõemetsa et al., *Independent Size and Fluorescence Emission Determination of Individual Biological Nanoparticles Reveals That Lipophilic Dye Incorporation Does Not Scale with Particle Size*, Langmuir **36**, 9693 (2020).
[121] Q. Lubart, J. K. Hannestad, H. Pace, D. Fjällborg, F. Westerlund, E. K. Esbjörner, and M. Bally, *Lipid Vesicle Composition Influences the Incorporation and Fluorescence Properties of the Lipophilic Sulphonated Carbocyanine Dye SP-DiO*, Physical Chemistry Chemical Physics **22**, 8781 (2020).
[122] J. Larsen, N. S. Hatzakis, and D. Stamou, *Observation of Inhomogeneity in the Lipid Composition of Individual Nanoscale Liposomes*, J Am Chem Soc **133**, 10685 (2011).
[123] Y.-T. Hsiao, T.-Y. Wu, B.-K. Wu, S.-W. Chu, and C.-L. Hsieh, *Spinning Disk Interferometric Scattering Confocal Microscopy Captures Millisecond Timescale Dynamics of Living Cells*, Opt Express **30**, 45233 (2022).
[124] B. Midtvedt et al., *Single-Shot Self-Supervised Object Detection in Microscopy*, Nat Commun **13**, (2022).
[125] Wikimedia Commons contributors, *Jablonski Diagram of Fluorescence Only*, https://commons.wikimedia.org/w/index.php?title=File:Jablonski_Diagram_of_Fluorescence_Only.png&oldid=540353523 (accessed Mars 24, 2021).
[126] J. Happel and H. Brenner, *Low Reynolds Number Hydrodynamics: With Special Applications to Particulate Media*, Springer (1983).
[127] L. E. Reichl, *A Modern Course in Statistical Physics*, Fourth edition (Wiley-VCH, 2017).
[128] R. Kubo, *The Fluctuation-Dissipation Theorem*, Reports on Progress in Physics **29**, 255 (1966).

[129] D. S. Lemons and A. Gythiel, *Paul Langevin's 1908 Paper "On the Theory of Brownian Motion" ["Sur La Théorie Du Mouvement Brownien," C. R. Acad. Sci. (Paris) 146 , 530–533 (1908)]* , Am J Phys **65**, 1079 (1997).

[130] C. L. Vestergaard, P. C. Blainey, and H. Flyvbjerg, *Optimal Estimation of Diffusion Coefficients from Single-Particle Trajectories*, Phys Rev E Stat Nonlin Soft Matter Phys **89**, (2014).

[131] R. Metzler, J. H. Jeon, A. G. Cherstvy, and E. Barkai, *Anomalous Diffusion Models and Their Properties: Non-Stationarity, Non-Ergodicity, and Ageing at the Centenary of Single Particle Tracking*, Physical Chemistry Chemical Physics **16**, 24128 (2014).

[132] G. Muñoz-Gil et al., *Objective Comparison of Methods to Decode Anomalous Diffusion*, Nat Commun **12**, (2021).

[133] Wikimedia Commons contributors, *Csm Brownian Motion*, https://commons.wikimedia.org/w/index.php?title=File:Csm_Brownian-Motion_f99de6516a.png&oldid=490210695 (accessed Mars 15, 2021).

[134] E. Lauga, M. Brenner, and H. Stone, *Microfluidics: The No-Slip Boundary Condition*, in *Springer Handbook of Experimental Fluid Mechanics*, edited by C. Tropea, A. L. Yarin, and J. F. Foss (Heidelberg, 2007), pp. 1219–1240.

[135] D. M. Huang, C. Sendner, D. Horinek, R. R. Netz, and L. Bocquet, *Water Slippage versus Contact Angle: A Quasiuniversal Relationship*, Phys Rev Lett **101**, 1 (2008).

[136] I. Fratoddi, *Hydrophobic and Hydrophilic Au and Ag Nanoparticles. Breakthroughs and Perspectives*, Nanomaterials **8**, (2018).

[137] E. Lauga and T. M. Squires, *Brownian Motion near a Partial-Slip Boundary: A Local Probe of the No-Slip Condition*, Physics of Fluids **17**, (2005).

[138] P. A. Thompson and S. M. Troian, *A General Boundary Condition for Liquid Flow at Solid Surfaces*, Nature **389**, 360 (1997).

[139] D. Bonn, J. Eggers, J. Indekeu, and J. Meunier, *Wetting and Spreading*, Rev Mod Phys **81**, 739 (2009).

[140] J. L. Anderson, F. Rauh, and A. Morales, *Particle Diffusion as a Function of Concentration and Ionic Strength*, Journal of Physical Chemistry **82**, 608 (1978).

[141] S. H. Lee, R. S. Chadwick, and L. G. Leal, *Motion of a Sphere in the Presence of a Plane Interface. Part 1. An Approximate Solution by Generalization of the Method of Lorentz*, J Fluid Mech **93**, 705 (1979).

[142] O. I. Vinogradova and G. E. Yakubov, *Surface Roughness and Hydrodynamic Boundary Conditions*, Phys Rev E Stat Nonlin Soft Matter Phys **73**, (2006).

[143] H. Faxén, *Der Gültigkeitsbereich Der Stokes-Oseenschen Wiederstandsformel. Erklärung Einiger von J. Weyssenhoff Gefundener Unstimmigkeiten*, Ann Phys **368**, 581 (1920).

[144] H. Faxén, *Der Widerstand Gegen Die Bewegung Einer Starren Kugel in Einer Zähen Flüssigkeit, Die Zwischen Zwei Parallelen Ebenen Wänden Eingeschlossen Ist*, Ann Phys **373**, (1922).

[145] A. J. Goldman, R. G. Cox, and H. Brenner, *Slow Viscous Motion of a Sphere Parallel to a Plane Wall-I Motion through a Quiescent Fluid*, Chem Eng Sci **22**, 637 (1967).
[146] H. Brenner, *The Slow Motion of a Sphere through a Viscous Fluid towards a Plane Surface*, Chem Eng Sci **16**, 242 (1961).
[147] B. Lin, J. Yu, and S. A. Rice, *Direct Measurements of Constrained Brownian Motion of an Isolated Sphere between Two Walls*, Phys Rev E **62**, 3909 (2000).
[148] P. Dechadilok and W. M. Deen, *Hindrance Factors for Diffusion and Convection in Pores*, Ind Eng Chem Res **45**, 6953 (2006).
[149] S. Leroy, A. Steinberger, C. Cottin-Bizonne, A. M. Trunfio-Sfarghiu, and E. Charlaix, *Probing Biolubrication with a Nanoscale Flow*, Soft Matter **5**, 4997 (2009).
[150] N. Chenouard et al., *Objective Comparison of Particle Tracking Methods*, Nat Methods **11**, 281 (2014).
[151] A. J. Berglund, *Statistics of Camera-Based Single-Particle Tracking*, Phys Rev E Stat Nonlin Soft Matter Phys **82**, 1 (2010).
[152] Nobel Prize Outreach AB 2023, *The Nobel Prize in Physics 1965*, https://www.nobelprize.org/prizes/physics/1965/summary/ (accessed Feb. 11, 2023).
[153] F. Zernike, *How I Discovered Phase Contrast*, Science (1979) **121**, 345 (1955).
[154] T. E. Gureyev and K. A. Nugent, *Rapid Quantitative Phase Imaging Using the Transport of Intensity Equation*, Opt Commun **133**, 339 (1997).
[155] Y. Rivenson, Y. Wu, and A. Ozcan, *Deep Learning in Holography and Coherent Imaging*, Light Sci Appl **8**, (2019).
[156] P. Bon, G. Maucort, B. Wattellier, and S. Monneret, *Quadriwave Lateral Shearing Interferometry for Quantitative Phase Microscopy of Living Cells*, Opt Express **17**, 13080 (2009).
[157] I. Yamaguchi and T. Zhang, *Phase-Shifting Digital Holography*, Opt Lett **22**, 1268 (1997).
[158] Z. Wang, L. Millet, M. Mir, H. Ding, S. Unarunotai, J. Rogers, M. U. Gillette, and G. Popescu, *Spatial Light Interference Microscopy (SLIM)*, Opt Express **19**, 2643 (2010).
[159] H. M. L. Robert, K. Holanová, Ł. Bujak, M. Vala, V. Henrichs, Z. Lánský, and M. Piliarik, *Fast Photothermal Spatial Light Modulation for Quantitative Phase Imaging at the Nanoscale*, Nat Commun **12**, (2021).
[160] G. Baffou, *Wavefront Microscopy Using Quadriwave Lateral Shearing Interferometry: From Bioimaging to Nanophotonics*, ACS Photonics **10**, 322 (2023).
[161] H. Cao, R. Chriki, S. Bittner, A. A. Friesem, and N. Davidson, *Complex Lasers with Controllable Coherence*, Nature Reviews Physics **1**, 156 (2019).
[162] L. Huang, T. Liu, X. Yang, Y. Luo, Y. Rivenson, and A. Ozcan, *Holographic Image Reconstruction with Phase Recovery and Autofocusing Using Recurrent Neural Networks*, ACS Photonics **8**, 1763 (2021).

[163] D. Gabor, *A New Microscopic Principle*, Nature **161**, 777 (1948).
[164] E. N. Leith and J. Upatnieks, *Wavefront Reconstruction with Continuous-Tone Objects**, J Opt Soc Am **53**, 1377 (1963).
[165] K. Goto and Y. Hayasaki, *Three-Dimensional Motion Detection of a 20-Nm Gold Nanoparticle Using Twilight-Field Digital Holography with Coherence Regulation*, Opt Lett **40**, 3344 (2015).
[166] Wikimedia Commons contributors, *A Diagram Showing the 4F Correlator from Fourier Optics*, https://upload.wikimedia.org/wikipedia/commons/e/e6/4F_Correlator.svg (accessed Mars 7, 2023).
[167] C. Y. Cheng, Y. H. Liao, and C. L. Hsieh, *High-Speed Imaging and Tracking of Very Small Single Nanoparticles by Contrast Enhanced Microscopy*, Nanoscale **11**, 568 (2019).
[168] L. Saemisch, N. F. van Hulst, and M. Liebel, *One-Shot Phase Image Distinction of Plasmonic and Dielectric Nanoparticles*, Nano Lett **21**, 4021 (2021).
[169] F. Dubois, C. Schockaert, N. Callens, and C. Yourassowsky, *Focus Plane Detection Criteria in Digital Holography Microscopy by Amplitude Analysis*, Opt Express **14**, 5895 (2006).
[170] P. Memmolo, L. Miccio, M. Paturzo, G. Di Caprio, G. Coppola, P. A. Netti, and P. Ferraro, *Recent Advances in Holographic 3D Particle Tracking*, Adv Opt Photonics **7**, 713 (2015).
[171] R. Parthasarathy, *Rapid, Accurate Particle Tracking by Calculation of Radial Symmetry Centers*, Nat Methods **9**, 724 (2012).
[172] H. W. Kuhn, *The Hungarian Method for the Assignment Problem*, Naval Research Logistics Quarterly **2**, 83 (1955).
[173] K. Lindfors, T. Kalkbrenner, P. Stoller, and V. Sandoghdar, *Detection and Spectroscopy of Gold Nanoparticles Using Supercontinuum White Light Confocal Microscopy*, Phys Rev Lett **93**, (2004).
[174] V. Jacobsen, P. Stoller, C. Brunner, V. Vogel, and V. Sandoghdar, *Interferometric Optical Detection and Tracking of Very Small Gold Nanoparticles at a Water-Glass Interface*, Opt. Express **14**, 405 (2006).
[175] T. Heermann, F. Steiert, B. Ramm, N. Hundt, and P. Schwille, *Mass-Sensitive Particle Tracking to Elucidate the Membrane-Associated MinDE Reaction Cycle*, Nat Methods **18**, 1239 (2021).
[176] P. Kukura, H. Ewers, C. Müller, A. Renn, A. Helenius, and V. Sandoghdar, *High-Speed Nanoscopic Tracking of the Position and Orientation of a Single Virus*, Nat Methods **6**, 923 (2009).
[177] T. P. J. Knowles, P. K. Challa, K. L. Saar, Q. A. Peter, and Z. Toprakcioglu, *Optical Microscopy*, US 2022/0011560 A1 (January 2022).
[178] J. Dong, D. Maestre, C. Conrad-Billroth, and T. Juffmann, *Fundamental Bounds on the Precision of ISCAT, COBRI and Dark-Field Microscopy for 3D Localization and Mass Photometry*, J Phys D Appl Phys **54**, (2021).

[179] Wikimedia Commons contributors, *ISCAT Setup Configurations.*, https://upload.wikimedia.org/wikipedia/commons/e/e5/ISCAT_setup_configurations.svg (accessed Mars 9, 2023).
[180] B. Gul, S. Ashraf, S. Khan, H. Nisar, and I. Ahmad, *Cell Refractive Index: Models, Insights, Applications and Future Perspectives*, Photodiagnosis Photodyn Ther **33**, 102096 (2021).
[181] F. Chollet, *Deep Learning with Python* (Manning Publications Co, 2018).
[182] B. Midtvedt, S. Helgadottir, A. Argun, J. Pineda, D. Midtvedt, and G. Volpe, *Quantitative Digital Microscopy with Deep Learning*, Appl Phys Rev **8**, 011310 (2021).
[183] Y. Rivenson, T. Liu, Z. Wei, Y. Zhang, K. de Haan, and A. Ozcan, *PhaseStain: The Digital Staining of Label-Free Quantitative Phase Microscopy Images Using Deep Learning*, Light Sci Appl **8**, (2019).
[184] S. Helgadottir, A. Argun, and G. Volpe, *Digital Video Microscopy Enhanced by Deep Learning*, Optica **6**, 506 (2019).
[185] R. Öz, S. Kk, and F. Westerlund, *A Nanofluidic Device for Real-Time Visualization of DNA-Protein Interactions on the Single DNA Molecule Level*, Nanoscale **11**, 2071 (2019).
[186] S. R. Leslie, A. P. Fields, and A. E. Cohen, *Convex Lens-Induced Confinement for Imaging Single Molecules*, Anal Chem **82**, 6224 (2010).
[187] C. Yoshina-Ishii and S. G. Boxer, *Arrays of Mobile Tethered Vesicles on Supported Lipid Bilayers*, J Am Chem Soc **125**, 3696 (2003).
[188] F. Reina, S. Galiani, D. Shrestha, E. Sezgin, G. De Wit, D. Cole, B. Christoffer Lagerholm, P. Kukura, and C. Eggeling, *Complementary Studies of Lipid Membrane Dynamics Using ISCAT and Super-Resolved Fluorescence Correlation Spectroscopy*, J Phys D Appl Phys **51**, (2018).
[189] M. Bally, A. Gunnarsson, L. Svensson, G. Larson, V. P. Zhdanov, and F. Höök, *Interaction of Single Viruslike Particles with Vesicles Containing Glycosphingolipids*, Phys Rev Lett **107**, 1 (2011).
[190] A. Kunze, M. Bally, F. Höök, and G. Larson, *Equilibrium-Fluctuation-Analysis of Single Liposome Binding Events Reveals How Cholesterol and Ca2+ Modulate Glycosphingolipid Trans-Interactions*, Sci Rep **3**, 10 (2013).
[191] P. Joyce, S. Jõemetsa, S. Isaksson, S. Hossain, P. Larsson, C. Bergström, and F. Höök, *TIRF Microscopy-Based Monitoring of Drug Permeation Across a Lipid Membrane Supported on Mesoporous Silica*, Angewandte Chemie - International Edition **60**, 2069 (2021).
[192] K. M. Yip, N. Fischer, E. Paknia, A. Chari, and H. Stark, *Atomic-Resolution Protein Structure Determination by Cryo-EM*, Nature **587**, 157 (2020).
[193] L. E. Franken, E. J. Boekema, and M. C. A. Stuart, *Transmission Electron Microscopy as a Tool for the Characterization of Soft Materials: Application and Interpretation*, Advanced Science **4**, (2017).
[194] P. Zhang, G. Ma, W. Dong, Z. Wan, S. Wang, and N. Tao, *Plasmonic Scattering Imaging of Single Proteins and Binding Kinetics*, Nat Methods **17**, 1010 (2020).

[195] B. Agnarsson, A. Lundgren, A. Gunnarsson, M. Rabe, A. Kunze, M. Mapar, L. Simonsson, M. Bally, V. P. Zhdanov, and F. Höök, *Evanescent Light-Scattering Microscopy for Label-Free Interfacial Imaging: From Single Sub-100 Nm Vesicles to Live Cells*, ACS Nano **9**, 11849 (2015).
[196] P. Zhang, L. Zhou, R. Wang, X. Zhou, J. Jiang, Z. Wan, and S. Wang, *Evanescent Scattering Imaging of Single Protein Binding Kinetics and DNA Conformation Changes*, Nat Commun **13**, (2022).
[197] J. Ortega Arroyo, D. Cole, and P. Kukura, *Interferometric Scattering Microscopy and Its Combination with Single-Molecule Fluorescence Imaging*, Nat Protoc **11**, 617 (2016).
[198] L. Novotny and B. Hecht, *Principles of Nano-Optics*, Second edition (Cambridge university press, 2012).
[199] M. Sjöberg, *Multiparametric Optical Characterization of Biological Nanoparticles Using Evanescent Field Sensing* (Chalmers University of Technology, 2022).
[200] R. Fakhrullin, L. Nigamatzyanova, and G. Fakhrullina, *Dark-Field/Hyperspectral Microscopy for Detecting Nanoscale Particles in Environmental Nanotoxicology Research*, Science of the Total Environment **772**, 145478 (2021).
[201] M.-C. Nguyen, P. Bonnaud, R. Dibsy, G. Maucort, S. Lyonnais, D. Muriaux, and P. Bon, *Label-Free Single Nanoparticle Identification and Characterization Including Infectious Emergent Virus*, ArXiv Preprint ArXiv:2301.02542 (2023).
[202] A. Einstein, *Physikalische Gesellschaft Zu Berlin Und Deutsche Gesellschaft Für Technische Physik. Berlin, 17. July 1931*, Angewandte Chemie **44**, 685 (1931).
[203] J. F. Collis, S. Olcum, D. Chakraborty, S. R. Manalis, and J. E. Sader, *Measurement of Navier Slip on Individual Nanoparticles in Liquid*, Nano Lett **21**, 4959 (2021).
[204] G. Emilsson, R. L. Schoch, L. Feuz, F. Höök, R. Y. H. Lim, and A. B. Dahlin, *Strongly Stretched Protein Resistant Poly(Ethylene Glycol) Brushes Prepared by Grafting-To*, ACS Appl Mater Interfaces **7**, 7505 (2015).
[205] J. Q. Gerlach and M. D. Griffin, *Getting to Know the Extracellular Vesicle Glycome*, Mol Biosyst **12**, 1071 (2016).
[206] E. Olsén, S. Jõemetsa, A. González, P. Joyce, V. P. Zhdanov, D. Midtvedt, and F. Höök, *Diffusion of Lipid Nanovesicles Bound to a Lipid Membrane Is Associated with the Partial-Slip Boundary Condition*, Nano Lett **21**, 8503 (2021).
[207] L. A. Philips, D. B. Ruffner, F. C. Cheong, J. M. Blusewicz, P. Kasimbeg, B. Waisi, J. R. McCutcheon, and D. G. Grier, *Holographic Characterization of Contaminants in Water: Differentiation of Suspended Particles in Heterogeneous Dispersions*, Water Res **122**, 431 (2017).
[208] K. Thorsteinsson, E. Olsén, E. Schmidt, H. Pace, and M. Bally, *FRET-Based Assay for the Quantification of Extracellular Vesicles and Other Vesicles of Complex Composition*, Anal Chem **92**, 15336 (2020).
[209] A. Ymeti, J. Greve, P. V. Lambeck, T. Wink, S. W. F. M. Van Novell, T. A. M. Beumer, R. R. Wijn, R. G. Heideman, V. Subramaniam, and J. S. Kanger, *Fast,*

Ultrasensitive Virus Detection Using a Young Interferometer Sensor, Nano Lett **7**, 394 (2007).

[210] L. A. Jackson et al., *An MRNA Vaccine against SARS-CoV-2 — Preliminary Report*, New England Journal of Medicine **383**, 1920 (2020).

[211] F. P. Polack et al., *Safety and Efficacy of the BNT162b2 MRNA Covid-19 Vaccine*, New England Journal of Medicine **383**, 2603 (2020).

[212] X. Hou, T. Zaks, R. Langer, and Y. Dong, *Lipid Nanoparticles for MRNA Delivery*, Nat Rev Mater **6**, 1078 (2021).

[213] N. Aliakbarinodehi et al., *Interaction Kinetics of Individual MRNA-Containing Lipid Nanoparticles with an Endosomal Membrane Mimic: Dependence on PH, Protein Corona Formation, and Lipoprotein Depletion*, ACS Nano **16**, 20163 (2022).

[214] Y. Wu, R. D. Tilley, and J. J. Gooding, *Challenges and Solutions in Developing Ultrasensitive Biosensors*, J Am Chem Soc **141**, 1162 (2019).

[215] H. Aldewachi, T. Chalati, M. N. Woodroofe, N. Bricklebank, B. Sharrack, and P. Gardiner, *Gold Nanoparticle-Based Colorimetric Biosensors*, Nanoscale.

[216] R. Phillips, J. Kondev, J. Theriot, and H. Garcia, *Physical Biology of the Cell* (Garland Science, 2012).

[217] J. W. Lichtman and J. A. Conchello, *Fluorescence Microscopy*, Nat Methods **2**, 910 (2005).

[218] M. Küeppers, D. Albrecht, A. Kashkanova, J. Luehr, and V. Sandoghdar, *Confocal Interferometric Scattering Microscopy Reveals 3D Nanoscopic Structure and Dynamics in Live Cells*, Nat Commun **14**, 1962 (2023).

[219] J. Gilleron et al., *Image-Based Analysis of Lipid Nanoparticle-Mediated SiRNA Delivery, Intracellular Trafficking and Endosomal Escape*, Nat Biotechnol **31**, 638 (2013).